TÉCNICO LISBOA

Aerodynamic Performance Prediction of a Wind Turbine in Steady and Unsteady Conditions Using a Panel Method

Leonardo Buralli

Thesis to obtain the Master of Science Degree in

Energy Engineering and Management

Supervisors: Dr. João Manuel Ribeiro Costa Baltazar
Prof. Ricardo Balbino Santos Pereira

Examination Committee

Chairperson: Prof. Edgar Caetano Fernandes
Supervisor: Dr. João Manuel Ribeiro Costa Baltazar
Member of the Committee: Prof. José Alberto Caiado Falcão de Campos

July 2021

Dedicated to my mother, Maria Grazia, who taught me the importance of being resilient.

Acknowledgments

First of all, I would like to thank my supervisors Dr. João Baltazar and Prof. Ricardo Pereira who have given me the opportunity to work on a thesis related to a field I have always been interested about, wind energy. In particular, I would like to express my gratitude to Dr. João Baltazar for his constant support and guidance for the realisation of this thesis. I have really enjoyed the weekly - sometimes even daily - conversations we had throughout the last year, which have been key to overcome the numerous challenges encountered in this work and to widen my understanding of technical topics such as Panel Method and wind turbine aerodynamics.

I would also want to thank everyone working behind the Innoenergy SELECT program for organising such an incredible academic (and life) experience that allowed me not only to study at KTH in Stockholm and IST in Lisbon, but also to meet amazing people from all over the world. Indeed, I owe a huge thanks to every single person I have met on this journey for making me become a better human being.

A special thanks to my flatmates, colleagues and friends Jack, Berto, Vezzo, Bianka, Fede and Carla who made my days in Stockholm and Lisbon unforgettable. I could not have asked for better people to share this experience with.

Finally, I must thank my family, Maria Grazia, Aurora and Stefano, my girlfriend Sofia and all my Italian friends for having believed in me and supported me from the very beginning. I would not have achieved this result without you.

Resumo

Nos últimos anos, tem-se observado um rápido desenvolvimento tecnológico na indústria eólica com impacto no setor da energia, desempenhando um papel importante para a transição energética.

As turbinas eólicas operam num ambiente instável, experimentando vários efeitos (por exemplo, mudança abruptas na velocidade do vento). Este fenómeno pode resultar em grandes flutuações nas cargas das pás da turbina e torre, afetando consequentemente o projeto de tais sistemas.

O objetivo deste trabalho é o estudo aerodinâmico em condições estacionárias e não-estacionárias do escoamento potencial em torno duma turbina eólica, projetada para os testes experimentais New MEXICO usando o método de painel tridimensional desenvolvido no Instituto Superior Técnico (IST), *PROPAN*.

Em primeiro lugar, realizou-se um estudo numérico em condições estacionárias preparatório para as simulações não-estacionárias. Consideraram-se duas velocidades de vento, 10.05 m/s ($TSR = 10$) e 15.06 m/s ($TSR = 6.7$). Da comparação das simulações numéricas com os dados experimentais da New MEXICO, uma boa concordância é geralmente encontrada.

Em segundo lugar, estudou-se o caso da variação dinâmica do passo da pá e o seu efeito nas cargas da turbina para $TSR = 10$. Foram considerados dois modelos para a geometria da esteira, com a principal diferença no alinhamento e geometria. As forças previstas com ambas as geometrias de esteira são comparáveis às experimentais ao atingir a solução de estado estacionário. Por outro lado, a força undershoot e overshoot que ocorrem após a mudançã do passo não podem ser capturados corretamente.

Palavras-chave: Turbinas Eólica, Método de Painel, Escoamento Não-estacionário, MEXICO.

Abstract

In the recent years the wind industry has seen one of fastest-growing technological development in the energy sector, playing a massive role in the energy transition.

Wind turbines operate in a very unsteady environment, therefore experiencing variable effects (i.e. sudden change in wind speed). This can result in large oscillations of the loads on the turbine blades and tower, consequently affecting the performance of such systems.

The purpose of this work is the aerodynamic study under steady and unsteady inflow conditions of a wind turbine designed for the New MEXICO experiment using the three-dimensional panel method developed at Instituto Superior Técnico (IST), *PROPAN*.

First, an extensive numerical study under steady inflow conditions is performed to obtain a well-defined turbine grid to be utilised as input for the dynamic simulations. Two undisturbed wind velocities, 10.05 m/s ($TSR = 10$) and 15.06 m/s ($TSR = 6.7$), are considered. When comparing the simulated results with the New MEXICO experimental data, a good agreement is generally found.

Second, the dynamic blade pitch variation and its effect on the blade loads at $TSR = 10$ are described. Two different methods to create the wake geometry were applied, with the main difference of yielding a wake geometry either partially or fully aligned to the incoming wind flow. The forces predicted with both wake geometries are comparable to the experimental ones when achieving the steady state solution. On the other hand, the force undershoot and overshoot occurring after the pitch modification can not be captured properly.

Keywords: Wind Turbine, Panel Method, Dynamic Inflow, MEXICO.

Contents

List of Tables

List of Figures

Nomenclature

Abbreviations

$2D$	Two-dimensions
$3D$	Three-dimensions
BEM	Blade Element Momentum
CAD	Computer-Aided Design
CFD	Computational Fluid Dynamics
DNW	German Dutch wind tunnel
DTU	Technical University of Denmark
EAW	Empirical Aligned Wake
$HAWT$	Horizontal Axis Wind Turbine
IAW	Independent Aligned Wake
IST	Instituto Superior Técnico
LL	Lifting Line
LLF	Large Scale Low Speed Facility
LST	Delft University wind tunnel
$MEXICO$	Model EXperiments In COntrolled condition
PIV	Particle Image Velocimetry
$RANS$	Reynolds-averaged Navier–Stokes
TSR	Tip Speed Ratio
$VAWT$	Vertical Axis Wind Turbine

Greek symbols

α	Angle of attack

β Geometric inflow angle

β_i Inflow angle

$\Delta\theta$ Angular time step

Γ Circulation

μ Dipole strength

Ω Angular velocity

ϕ Perturbation potential

ψ Pitch angle

ρ Air density

σ Source strength

ξ Hermite interpolation parameter

Roman symbols

$\mathcal{S}_{\mathcal{B}}$ Blade surfaces

$\mathcal{S}_{\mathcal{H}}$ Hub surfaces

$\mathcal{S}_{\mathcal{W}}$ Wake surfaces

$\mathcal{S}$ Boundary domain

$\vec{e}_r$ Radial unit vector

$\vec{e}_s$ Unit vector tangent to vortex sheet

$\vec{n}$ Unit normal

$\vec{S}$ Position vector

$\vec{V}$ Total wind velocity field

$\vec{V}_m$ Mean velocity on the wake surface

$\vec{V}_w$ Velocity of the points on the wake surface

$\vec{x}$ Position vector

a Axial induction factor; helical axial pitch per unit radian

a' Angular induction factor

c Airfoil chord

C_D Drag coefficient

C_L Lift coefficient

C_n, C_t Normal and tangential force coefficient to blade section chord, respectively

C_P Power coefficient

C_p Pressure coefficient

C_T Thrust coefficient

C_X, C_Q Normal and tangential force coefficient to the rotor plane, respectively

D Drag; diameter

D_{ij} Dipole influence coefficient matrix

F_n Normal force per unit length

F_t Tangential force per unit length

f_{max} Blade section maximum camber

F_{res} Resultant force

it Blade section rake

J_I, J_F Initial and final wake strip, respectively

J_V Alignment section radial wake strips

K Number of rotor blades; number of blade-hub sectors

L Lift

N Total number of panels in the blade-hub sectors

n Time step

N_C Number of blade panels in the chordwise direction

N_R Number of blade panels in the spanwise direction

N_t Total number of time steps

N_W Number of wake panels for each radial strip in the streamwise direction

N_θ Number of angular time steps per revolution

N_{hd} Number of hub panels in the downstream direction

N_{ht} Number of hub panels in the circumferential direction

N_{hu} Number of hub panels in the upstream direction

N_{R_W} Number of wake panels in the spanwise direction

N_{rev} Number of rotor revolutions

N_{WA} Number of wake alignment iterations

p Pressure; pitch

p_∞ Pressure of undisturbed inflow

Q Torque

R Rotor radius

Re Reynolds number

S_{ij} Source influence coefficient matrix

T Thrust; temperature

t Time variable

t_{max} Blade section maximum thickness

U Undisturbed wind velocity

v_a, v_t Axial and tangential induced velocities

V_∞ Relative wind velocity

x, r, θ Cylindrical coordinate system rotating with turbine rotor

x, y, z Cartesian coordinate system rotating with turbine rotor

x_0, r_0, θ_0 Inertial earth-fixed cylindrical coordinate system

x_0, y_0, z_0 Inertial earth-fixed Cartesian coordinate system

X_V Alignment section axial positions

x_W Axial wake length

x_{fw} Transition wake final streamwise position

x_{uw} Ultimate wake final streamwise position

Subscripts

amb Ambient condition

h, t Hub and tip radius, respectively

i, j Grid panel strips

i, v Inviscid and viscous, respectively

le, te Leading and trailing edges, respectively

n Normal component

S Surface

t Tangential component

Superscripts

(h) Iteration step.

$+, -$ Suction and pressure sides, respectively.

Chapter 1

Introduction

The impact of climate change has been increasingly evident over the last decade. The melting of glaciers has reached dramatic levels due to the incredible rise in temperatures seen all over the planet. This has also led to more destructive natural disasters such as floods, wildfires and droughts, which affected massively local communities. The implementation of energy systems running on renewable sources, together with the introduction of strong and courageous governmental energy policies, is fundamental to tackle climate change and achieve the global emissions reduction goals signed in the Paris Agreement.

In the complexity of the global energy mix, wind energy will play a massive role in the transition from a fossil-fuel-based economy to a greener and more sustainable one. Wind industry has seen one of fastest-growing technological development in the energy sector, passing from an average of 1 MW turbines installed at the beginning of this century to the recent production of turbines with a rated capacity up to 15 MW. These advancements went hand in hand with cost reductions, which are going to be progressively greater in the future. As a matter of fact, onshore wind energy is set to consistently offer a less expensive source of new electricity than the least-cost fossil fuel alternative in most countries [1].

Massive achievements are also expected to be obtained from the deployment of large-scale offshore wind farms. In the past years, the offshore wind industry has grown in European countries bordering the North Seas because of the high quality wind resources and relatively shallow water, limiting consistently the replicability of such systems in deep water conditions, where most of the potential offshore wind resource is located. The recent development of floating offshore wind turbines represents a game-changer solution to this issue, enhancing drastically the impact of wind energy on the decarbonisation of power production.

1.1 Wind energy technology

A wind turbine is a machine that works on a simple principle: it transforms kinetic wind energy into rotational mechanical energy, which eventually spins a generator to produce electrical energy. More in detail, it takes advantage of the aerodynamic force generated on the rotor blades, following the same

physical principles that make an airplane fly. This force is the resultant of two components, lift and drag, and derives from the difference in the air pressure between the two sides of each blade, occurring when wind flows across the blades. More specifically, considering a specific blade, the air pressure on its upper side decreases (suction side), while it increases on the lower side (pressure side). The ratio between lift and drag is a key parameter for optimising the design of the blades and must be evaluated in relation to the wind turbine type.

Wind turbines can be grouped mainly in two categories: Horizontal Axis Wind Turbine (HAWT) and Vertical Axis Wind Turbine (VAWT). The former is characterised by the rotor axis being parallel to the wind flow, thus it is a lift-driven machine. The latter has a vertical axis perpendicular to the ground, with the blades rotating around it. More specifically, this type of turbine utilizes drag or lift or a combination of the two to operate [2]. A brief description of both concepts is presented in the following sections.

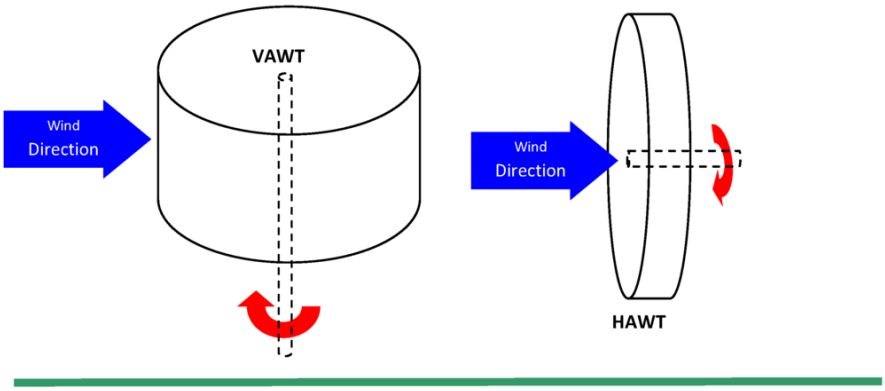

Figure 1.1: Shaft and rotor orientation for HAWT and VAWT [3].

1.1.1 Horizontal axis wind turbine

Nowdays the HAWT type has become the most used mechanical device to harvest wind energy , since it has been largely supported with fundings for research and development throughout the years [2, 4]. The continuous interest in this particular device has been sustained by the great achievements obtained in terms of power production and efficiency, which make HAWTs dominant in the utility-scale power generation market.

A HAWT is made of a tower, a nacelle, a generator and rotor blades. The nacelle contains key components to run the turbine efficiently, such as gear box (usually in case of variable speed turbines), low- and high-speed shafts, generator, controller, and brakes. In addition, a wind speed anemometer and a wind vane are mounted on the nacelle. All of these devices are necessary because HAWTs need some control actions [5]:

- Brake system to avoid any damage to the turbine in extreme wind conditions;
- Yaw system to always align the rotor axis to wind direction;
- Stall or pitch regulation, in order to control the power output.

Within the HAWT category, an important parameter that has been deeply studied to maximise the efficiency is the number of blades. A 3-bladed layout is commonly accepted to be a good practical trade-off between torque (which affects positively power output) and structural stability (a high number of blades leads to a heavy structure to be withstood by the tower). On the other hand, there is not an absolute optimal number of blades, since it largely depends on the application and size of the turbine. Moreover, there are still many discussions around this topic in the wind industry, such that in the future other turbine configurations might take over the 3-bladed design.

Another distinction can be made for HAWTs having either an upwind or downwind configuration, as shown in Figure 1.2. The difference lies in the position of the rotor in relation to the tower, which influences the wind profile seen by the rotor blades and ultimately the maximum power extraction. Downwind turbines have the advantage of not requiring an active yaw mechanism and there is no risk of blades hitting the tower. On the other hand, the tower induces turbulence which leads to periodic loads on the blades and power fluctuation, a phenomenon called ”tower shadow” [6]. Furthermore, common upwind turbines' nacelle assemblies are installed with specific cone angles which represent the angle between the main turbine axis and the horizontal axis, so to prevent contact between the turbine blades and the tower. Therefore, upwind turbines are the most commercialised ones.

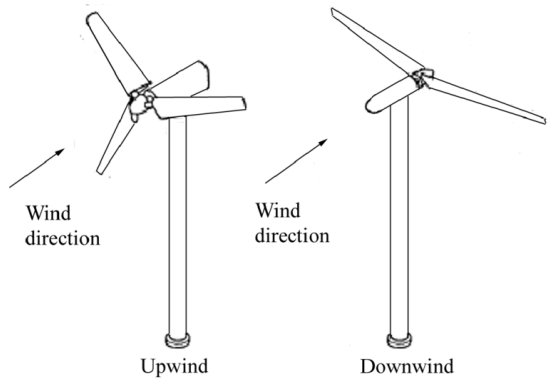

Figure 1.2: Upwind and downwind configuration for HAWTs [6].

1.1.2 Vertical axis wind turbine

Historically VAWTs were the first ever wind turbines to be used for harnessing wind energy. However researchers of the modern era lost interest in it due to the initial perception that VAWT cannot be used for large scale electricity generation [7]. There are generally two main designs: Savonius and Darrieus (Figure 1.3). The former is composed by two or more semi-cylindrical buckets that use drag force to put into rotation the vertical shaft. Darrieus wind turbines use airfoil shape blades, usually three, that generate lift force to rotate the main shaft. The rotor of Darrieus turbines can assume different configurations, as ”egg-beater”, H-shape or helical shape [8]. Overall, Darrieus have a lower starting torque but a higher efficiency.

Although the limited number of VAWT installations, it has several significant advantages compared to HAWT that can be summurised as follows:

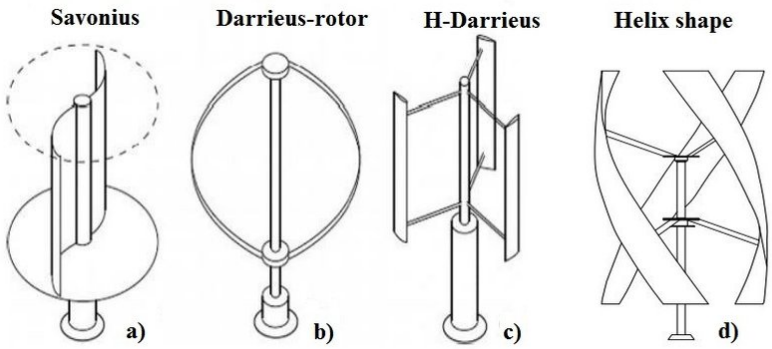

Figure 1.3: Different kinds of vertical axis wind turbines (VAWT): (a) Savonius; (b) Darrieus with "egg-beater" design rotor; (c) H-shape blades; (d) helix shape blades [8].

- Insensitivity to wind direction, thus no yaw system required;
- Less components and consequent reduced risk of failures;
- Ability to produce power at low wind speed (i.e. urban areas);
- Low level of noise.

Despite these pros, there are many drawbacks to be considered. For instance, VAWT is inefficient in high speed wind environment because it has very low starting torques and issues on its dynamic stability. It has also a high cost of drive train, low power efficiency, and high dynamic loading on the blades [6].

1.2 State of art of HAWT performance prediction

Aerodynamic load is part of the decisive effects that wind turbine must consider. It directly affects the structural design of a wind turbine blade, the design of the generator set and the design of control system [9]. Therefore, performance forecasting is fundamental when designing a wind turbine and its accuracy plays a central role in the economic feasibility of wind farm projects.

Conducting direct experiments is obviously the best solution to obtain data with high level of accuracy. However, wind turbines size represents a big limit to the implementation of real-scale experiments, both from a physical and economic perspective. As a matter of fact, testing modern HAWTs means to handle 160-meter-diameter machines which consequently lead to many technical difficulties (i.e. wind tunnel size).

In this framework, the continuous development of analytical methods and software for wind turbine loads prediction has been heavily supported by researchers and companies. Blade Element Momentum theory (BEM), lifting line, panel method and CFD are among the main methods utilised by the wind industry.

1.2.1 BEM Theory

Most of the present wind turbine design codes are based on Blade Element Momentum (BEM) theory. This theory can be considered as a combination of the Blade Element Theory, which models the blade aerodynamics, and the Momentum Theory which models the induction aerodynamics [10]. The former consists in dividing the blade into small elements that act independently of surrounding elements and operate aerodynamically as 2D airfoils. Aerodynamic forces are calculated on each segment and then summed along the whole blade span to compute the total force and torque. The latter completes the formulation providing a prediction of ideal efficiency and flow velocity, determining the forces acting on the rotor. From the Momentum Theory, the differential torque (dQ) and thrust [1] (dT) can be computed as:

$$dQ = 4\pi r^3 \rho U \Omega a'(1-a)dr \tag{1.1}$$

$$dT = 4\pi r \rho U^2 a(1-a)dr \tag{1.2}$$

The induction factors a and a' represent the axial and angular velocity changes, respectively, in wind and rotational speed as the wind passes through the rotor axis, U is the undisturbed flow velocity, Ω is the rotational speed of the rotor and ρ is the air density. From the Blade Element Theory, the same quantities can be defined as:

$$dQ = \frac{1}{2} K \rho V_\infty^2 c C_Q r dr \tag{1.3}$$

$$dT = \frac{1}{2} K \rho V_\infty^2 c C_X dr \tag{1.4}$$

where K is the number of blades, V_∞ represents the relative wind velocity, c is the chord length, C_X and C_Q are the normal and tangential force coefficients to the rotor plane, respectively, and are calculated as:

$$V_\infty = \sqrt{U^2(1-a)^2 + \Omega^2 r^2 (1+a')^2} \tag{1.5}$$

$$C_X = C_L cos\beta_i + C_D sin\beta_i \tag{1.6}$$

$$C_Q = C_L sin\beta_i - C_D cos\beta_i \tag{1.7}$$

The lift coefficient $C_L = \frac{L}{1/2\rho V_\infty^2 c}$ and drag coefficient $C_D = \frac{D}{1/2\rho V_\infty^2 c}$ (Lift L and Drag D) depend on the angle of attack α and the Reynolds number Re. These are experimentally computed and given for different airfoils. The inflow angle β_i is the sum of α and the pitch angle ψ. All the velocities, angles and forces mentioned above are shown in the velocity triangle of Figure 1.4.

By equating Equation (1.1) with Equation (1.3) and Equation (1.2) with Equation (1.4), it is possible to solve a system of equations with the unknown a and a'. The solving method is iterative, assuming new values of the induction factors a and a' until a certain tolerance is met. Finally the thrust and power

[1] In this work the term *thrust* indicates the axial force experienced by the wind turbine.

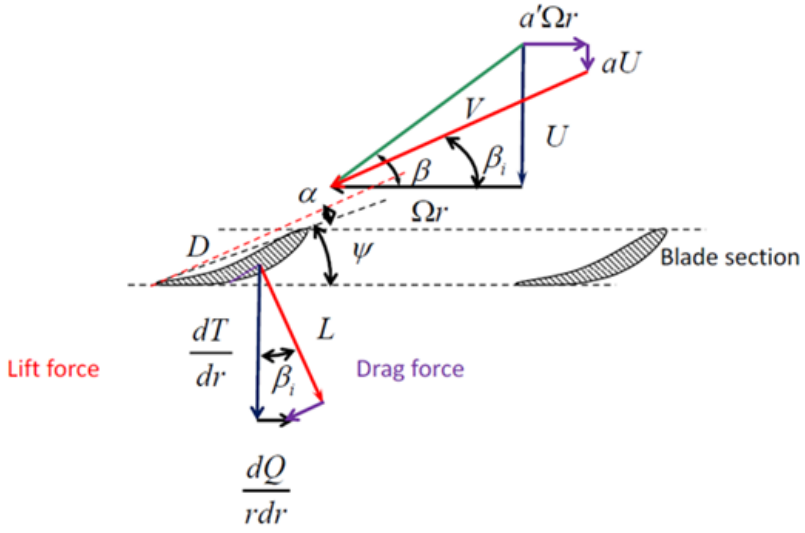

Figure 1.4: Blade velocity triangle [11].

coefficients (C_T and C_P) can be obtained as:

$$C_T = \frac{T}{\frac{1}{2}\rho U^2 \pi R^2} \tag{1.8}$$

$$C_P = \frac{\Omega Q}{\frac{1}{2}\rho U^3 \pi R^2} \tag{1.9}$$

BEM is a relatively simple method and does not need of heavy computational power. On the other hand, as mentioned at the beginning of this section, it relies on many unrealistic assumptions. Some corrections have been proposed throughout the years, such as the Prandtl tip loss correction, Glauert's correction and the Rotational Augmentation correction. The first erases the assumption of an infinite number of blades, the second provides a better relationship between the induction factors and the thrust coefficient, while the third takes into account the delay in stall phenomenon experienced by the most inboard sections of a rotating blade when compared to the 2D stationary characteristic of the airfoil. Although these improvements, BEM is derived from stationary conditions while wind turbines operate at a very unsteady environment.

1.2.2 Lifting Line

A sophisticated but still computationally efficient approach to account for the complex flow phenomena on wind turbine rotors can be found in the lifting-line (LL) theory [12]. This method produces accurate prediction of rotor forces and efficiency and quickly converges to optimal rotor parameters such as diameter, rotation rate and blade number. Furthermore, it offers several advantages over BEM, such as a more accurate relationship between the induction velocities and the radial circulation distribution [13]. On the other hand, many assumptions have still to be made, such as constant angular velocity, uniform flow aligned with the rotation axis and inviscid and incompressible fluid.

In this model each turbine blade is represented by a radial bound vortex (lifting line). Considering a cylindrical coordinate system (x, r, θ), the lifting lines are located at $\theta_k = 2\pi(k-1)/K, k = 1, ..., K$ with a variable circulation $\vec{\Gamma} = -\Gamma(r)\vec{e_r}$, where $\vec{e_r}$ is the radial unit vector. Applying the Helmholtz theorem, the vortex shed by the single lifting line has the intensity $\vec{\gamma} = \frac{d\Gamma(r)}{dr}\vec{e_s}$, with $\vec{e_s}$ the unit vector tangent to the vortex sheet [4], as shown in Figure 1.5.

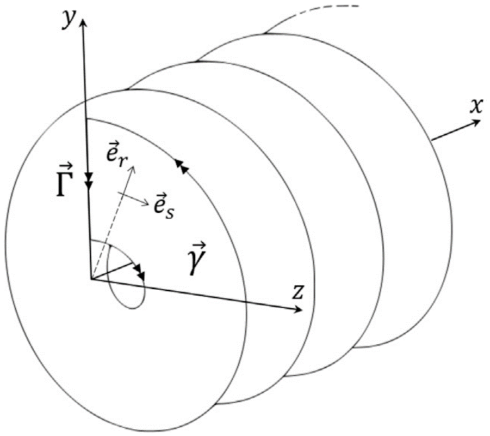

Figure 1.5: Vortex shed by a single lifting line [4].

From the Biot-Savart law and symmetrical considerations, the total induced velocity at the lifting lines can be described as:

$$\vec{v}(\vec{x}) = \frac{1}{4\pi}\sum_{k=1}^{K}\int_{S_k}\frac{\vec{\gamma}\times\vec{S}}{S^3}dA \tag{1.10}$$

where $\vec{S}$ is the position vector from the integration point to the field point with module S. The relative velocity V_∞ can then be expressed as:

$$V_\infty = \sqrt{(U - v_a)^2 + (\Omega r + v_t)^2} \tag{1.11}$$

with v_a and v_t being the axial and tangential induced velocities, respectively. Keeping the definitions of forces and angles presented in Section 1.2.1, the lift coefficient C_L can be expressed as $C_L = \frac{2\Gamma}{V_\infty c}$. Taking as reference length R and as reference velocity U, Equation (1.8) and Equation (1.9) can be converted into dimensionless form as follows:

$$C_T = \frac{2K}{\pi}\int_{r_h}^{1}((TSR)r + v_t)\Gamma(1 + \frac{C_D}{C_L}\tan\beta_i)dr \tag{1.12}$$

$$C_P = \frac{2K(TSR)}{\pi}\int_{r_h}^{1}(1 - v_a)\Gamma(1 - \frac{C_D}{C_L}\cot\beta_i)rdr \tag{1.13}$$

where r_h is the non-dimensional hub radius and TSR is the tip-speed-ratio, defined as $TSR = \Omega R/U$.

In the classical theory, each trailing vortex is assumed to be a helix with fixed radius and pitch [13], thus the wake is considered rigid. This represents a considerable limit when comparing the LL results to the experimental ones. In order to overcome this issue, wake-alignment methods can be implemented, as presented in [4]. These methods consist of computing the induced velocities in different sections downstream of the rotor plane, leading to an axial variation of pitch, aligned with the axial and tangential

velocity components.

1.2.3 Panel method

Boundary Element Methods, also known as Panel methods, have been developed for decades to perform calculation of incompressible potential flow of propellers and lifting-bodies. The main characteristic is to have the body surface divided into some small panels.

The basic panel method covering only non-lifiting bodies was developed by a group led by Hess and Smith [14] at Douglas Aircraft in the late 1950s and early 1960s [15]. In this method, flat quadrilateral elements with constant source distributions were used to represent the body surface. In order to predict the lift force, vorticity was then included in the method by Hess [16]. Later Morino and Kuo [17] made a deep discussion of the method and gave a great contribution to applying the method to the aerodynamics, introducing the implementation of hyperboloidal quadrilateral panels with constant source and constant normal dipole distributions on the body surface. Further improvements and adjustments were then developed by Pyo [18] and Hsin et al. [19], validating the method as a powerful solution for potential flow calculations. Moreover, good results have also been yielded from studies of potential flow in unsteady conditions (see for instance [20, 21]).

When compared to CFD (RANS), various studies demonstrated a great accuracy in analysing the rotational flow field, with good comparison of the pressure distributions and loadings on propeller blades under unsteady conditions [22, 23].

1.2.4 RANS

The Navier-Stokes equations govern the flow physics of Newtonian fluids, such as air. Although these differential equations are extremely complex to solve, the continuous development of computational fluid dynamics (CFD) algorithms represents a winning tool. Indeed, CFD yields a more consistent and physically realistic flow field around a wind turbine than BEM and LL. In the last decades a large number of CFD studies on rotor aerodynamics have been done since its first application to a full rotor by Hansen et al. [24] (see for example [25–27]).

The main CFD approach utilised by the wind industry relies on the Reynolds Averaged Navier-Stokes (RANS) equations, which are a time-averaged version of the exact Navier-Stokes equations. Extensive studies have been carried out by Kang and Hirsch [28] and by the Technical University of Denmark (DTU), utilising their in-house Navier-Stokes solver EllipSys2D/3D to predict overall performances, loads, design of rotors and blade sections [29]. This approximation reduces consistently the computational power that would be needed to run even more complex methods (i.e. Large Eddie Simulation).

Thus, RANS simulations are more accurate in predicting wind turbine performances compared to BEM and LL, whereas they require a much greater computational power and running time.

1.3 Dynamic inflow

When a sudden change in pitch angle, rotor speed or wind speed occurs, the wake behind the turbine, and consequently the induction and the resulting effective velocity in the rotor plane will achieve steady state conditions only after a certain delay. This phenomenon is commonly called *dynamic inflow*.

It can be explained in terms of a vorticity representation of the wake (and the blades). The wake vorticity is made of shed vorticity and trailing vorticity, both time dependent. Dynamic inflow phenomena depend mainly on the trailing vorticity (i.e. the vorticity related to the spanwise variation of the bound vortex), where the shed vorticity (i.e. the vorticity related to the unsteady variation of the bound vortex) is accounted for through unsteady profile aerodynamics [10]. Figure 1.6 shows the trailed vorticity, which is generated at the blade and convected downstream with the local total velocity, partly wake induced. A new vorticity is created when a change in bound vorticity (e.g. through a change in the blade pitch angle) occurs. Since the vorticity is convected with a finite velocity, the resulting wake becomes a combination of old and new vorticity. As soon as the old vorticity has travelled a distance of some 2 to 4 diameters behind the rotor, its influence is hardly felt any more in the rotor plane and the new equilibrium situation is reached. However, before the vorticity has travelled this distance, a gradual change of the induced velocity takes place from its old equilibrium value to its new equilibrium value [30]. This transitory period leads to a force undershoot or overshoot acting on the rotor.

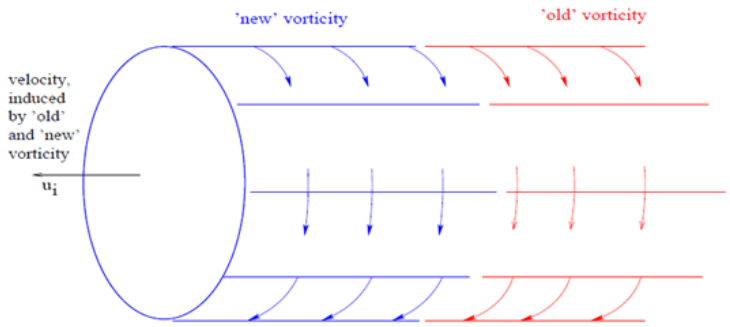

Figure 1.6: Wake with multiple vorticity derived from a pitch angle step [30].

The effects of this transitoty behaviour in the wake vorticity have a large practical importance, not only in view of the higher dynamic loads experienced by the turbine but also because of its impact on the aerodynamic damping characteristics and in particular in the design of pitch control algorithms [30]. Indeed, the consideration of dynamic inflow models when designing wind turbine controllers has been proved to be central to reduce tower fatigue load [31].

For these reasons, experiments in wind tunnels and developments of aerodynamic models aimed at simulating dynamic effects are fundamental. Since this phenomenon is driven by a change in axial force coefficient, the most common methodology is to vary the blade pitch angle.

1.4 Objective of the thesis

The purpose of this work is the aerodynamic study under steady and unsteady inflow conditions of a wind turbine designed for the New MEXICO experiment using the three-dimensional panel method developed at Instituto Superior Técnico (IST), *PROPAN* [32].

The New MEXICO experiment (Model EXperiments In COntrolled condition) consists of a series of measurements carried out on a 4.5 meter-diameter HAWT in the German Dutch Wind Tunnel (DNW) [33]. The aim of this project was to create a database containing experimental data for a wide range of wind conditions to be used for validation of computational methods.

The main focus is to compare the results obtained by *PROPAN* to the New MEXICO data under steady and dynamic inflow conditions at specific wind and rotational speeds, in order to assess the current potentiality of the panel method in terms of steady and dynamic load forecasts and lay the foundations for further improvements and developments. More in detail, two undisturbed wind velocities, 10.05 m/s ($TSR = 10$) and 15.06 m/s ($TSR = 6.7$), are considered for the steady simulations, while the dynamic blade pitch variation and its effect on the blade loads at $TSR = 10$ are simulated for the dynamic study.

Chapter 2

New Mexico project

The New MEXICO experiments were carried out on a 4.5 m diameter HAWT model between the 20^{th} of June and the 4^{th} of July 2014 in the in the Large Scale Low Speed Facility (LLF) of the German Dutch Wind Tunnels (DNW). It was supported by the European Union with the main goal of providing a database of aerodynamic measurements and it was a follow up of the MEXICO project, which was performed in 2006. The reason behind these new measurements was to improve the quality of the results achieved in the MEXICO experiment, taking into account the lessons learnt from it [33]. Figure 2.1 shows the experiment set-up.

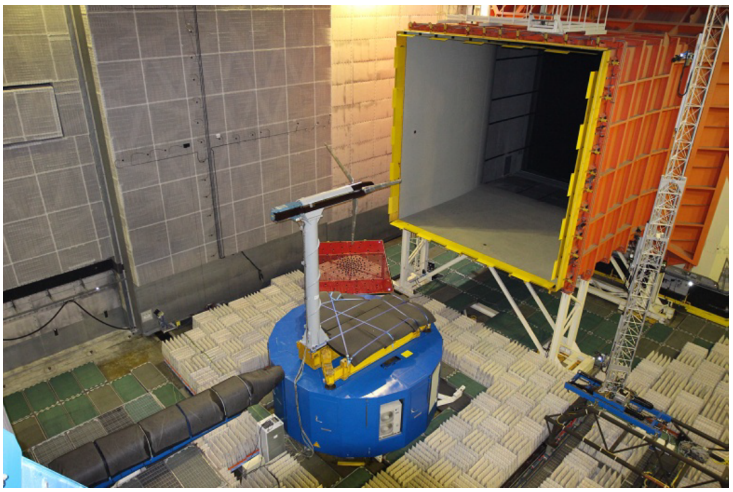

Figure 2.1: Set-up of the New MEXICO experiment [34].

In the following sections, a summary of the experiment is presented, while a complete description is reported in [34].

2.1 Turbine model

The 4.5 m diameter model subject of experiments includes a three bladed rotor, equipped with a speed controller and pitch actuator. Table 2.1 provides a summary of the general turbine properties.

The blade shape is composed by three different airfoil sections:

Rotor		
Rotation direction	[-]	Clockwise (facing the upwind part of the rotor)
Number of blades	[-]	3
Power regulation	[-]	Not present, speed control by motor/generator
Rotor speed	$[rpm]$	324.5-424.5
Swept area	$[m^2]$	15.9
Rotor diameter	$[m]$	4.5
Hub height	$[m]$	5.49
Tilt angle	[°]	0
Blades		
Blade length	$[m]$	2.04
Cone angle	[°]	0
Prebend	[-]	No prebend
Roughness	[-]	Both partly clean and fully zig-zag taped configuration
Material	[-]	Aluminium 7075-T651 Alloy
Tower		
Type	[-]	Tubular
Height including base	$[m]$	5.120
Diameter	$[m]$	0.508
Wall thickness	$[m]$	0.011
Roughness	[-]	Spiral flange to provoke transition
Material	[-]	Steel
Pitch system		
Type	[-]	Linear actuator
Range	[°]	[-5,90]

Table 2.1: New MEXICO model general information.

- DU91-W2-250 at the blade root, designed by Delft University;
- RISØ A2-21 at mid span, designed by the Risø National Laboratory in Denmark;
- NACA64-418 at the tip, derived from a mathematical formula elaborated by the ”National Advisory Committee for Aeronautics” (NACA).

A graphical representation can be seen in Figure 2.2 while the geometrical description of the blade properties is given in Table 2.2. It is important to notice that the blade radius starts at 0.210 m because the measurements were obtained from the centre of the rotor turbine.

In addition, roughness strips (zigzag strips) were applied on pressure and suction side of the blades, in order to obtain a more realistic boundary layer transition and avoid laminar separation on the blades. Therefore, the 2D aerodynamic lift and drag coefficients ($C_L(\alpha, Re)$, $C_D(\alpha, Re)$) are given for transition fixed (DU91 and RISØ) and both transition fixed and free (NACA). The Reynolds number is defined as $Re = \frac{Vc}{\nu}$, where ν is the kinematic viscosity and V is the tunnel velocity. In fact, RISØ A2-21 data was not available, thus it was substituted by RISØ A1-21 data. Further details of the aerodynamic coefficients are presented below.

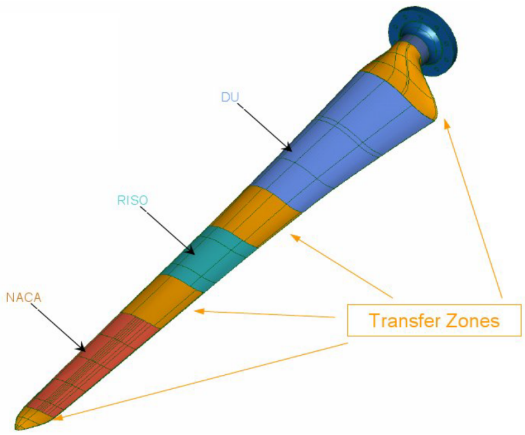

Figure 2.2: New MEXICO blade shape details [34].

Radius [m]	**Chord** [m]	**Twist** [°]	**Profile name** [-]
0.000	0.195	0.000	Cylinder
0.020	0.195	0.000	Cylinder
0.025	0.090	0.000	Cylinder
0.090	0.090	0.000	Cylinder
0.165	0.165	8.200	Transition (0.090 m to 0.240 m)
0.240	0.240	16.400	DU91-W2-250
0.465	0.207	12.100	DU91-W2-250
0.690	0.178	8.300	DU91-W2-250
0.815	0.166	7.100	DU91-W2-250
0.915	0.158	6.100	Transition (0.815 m to 1.015 m)
1.015	0.150	5.500	RISØ A2-21
1.140	0.142	4.800	RISØ A2-21
1.265	0.134	4.000	RISØ A2-21
1.365	0.129	3.700	Transition (1.265 m to 1.465 m)
1.465	0.123	3.200	NACA64-418
1.590	0.116	2.600	NACA64-418
1.815	0.102	1.500	NACA64-418
1.955	0.092	0.700	NACA64-418
1.983	0.082	0.469	NACA64-418
2.012	0.056	0.231	NACA64-418
2.040	0.011	0.000	NACA64-418

Table 2.2: New MEXICO blade geometric properties.

- DU91-W2-250

  The DU airfoils data are taken from measurements in the Delf University wind tunnel (LST) using different chord lengths (0.25 m and 0.60 m) and Reynolds numbers varying between 0.4×10^6 and 1×10^6. The data used in New MEXICO experiment is based on a chord length equal to 0.25 m and on two Reynolds numbers, 0.5×10^6 and 0.7×10^6.

- RISØ A1-21

This profile has been measured in the "Velux Wind Tunnel" at RISØ National Laboratory (Denmark). The data was given for $Re = 1.6 \times 10^6$. More information can not be provided due to confidentiality reason.

- NACA 64-418
  Also this profile has been measured in the Delft University wind tunnel (LST), for an airfoil chord of 0.25 m and Reynolds numbers between 0.3×10^6 and 1×10^6. The two datasets used in the experiment have $Re = 0.3 \times 10^6$ and $Re = 0.7 \times 10^6$.

Moreover, the blade CAD file is provided.

2.2 Wind tunnel

The LLF wind tunnel is a closed circuit, atmospheric, continuous low-speed wind tunnel. The configuration used for the New MEXICO experiment features an open test section of $9.5 \times 9.5\ m^2$, where flow is blowing from a nozzle to a collector (with a closed loop between collector and nozzle). The tunnel speed can vary between 5.5 m/s and 30 m/s.

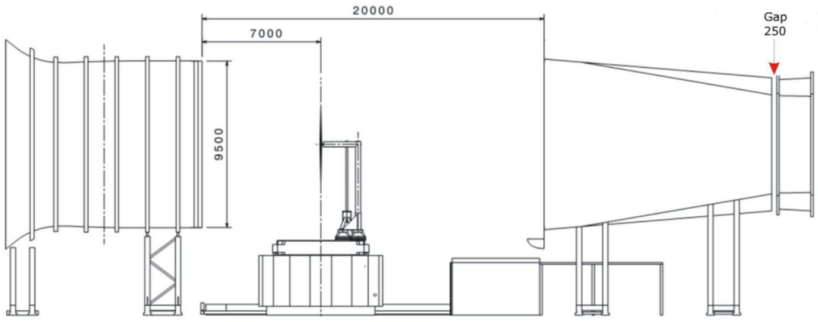

(a) Side view

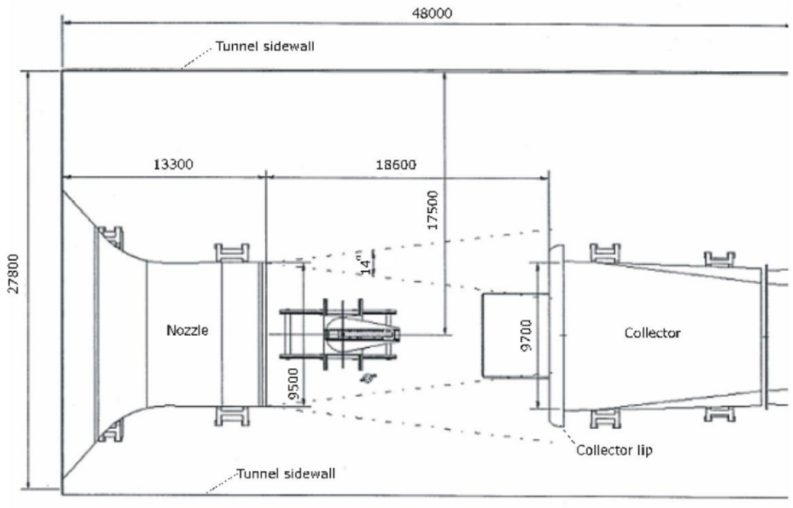

(b) Top view

Figure 2.3: Schematic view of the wind tunnel [34].

2.3 Data acquisition

The wind turbine model was instrumented with several sensors in order to evaluate many important quantities. The underlying convention to interpret the data correctly is that the rotor azimuth angle is considered zero when the blade 1 is at 12 o'clock position (aligned with the tower). Hence, the azimuth position for blade 2 and blade 3 are -120° and $+120^\circ$, respectively.

Tunnel data

Several measurements were performed to obtain tunnel data variables such as free-stream velocity, atmospheric pressure, tunnel temperature, yaw angle and pitch angle. Total and static pressure were measured in the side walls of the nozzle and calibrated against a pitot tube at the model center location (without model present) to obtain a relation between contraction pressures and free-stream velocity at the model location. Moreover, eight pressures were measured using taps in the collector entrance to gather more information on tunnel effects.

Balance data

The tower was mounted on a yawable DNW-balance for the measurement of three forces and three moments. The weight of the model affects the results whereas no corrections have been applied. As a consequence, the desired accuracy of the measurements was not achieved.

Pressure data

One of the most important physical quantities to be determined is the pressure magnitude around the blades. Thus, the blades were instrumented with 148 fast Kulite pressure sensors mounted at five specific span positions: 25%, 35%, 60%, 82% and 92%.

PIV data

Particle Image Velocimetry (PIV) is an optical measurement technique where the velocity field of an entire region within the flow is measured simultaneously [35]. Therefore, this technique made it possible to determine the 3D flow field in a detailed quantitative way, both upstream and downstream of the model. Further details can be found in [34].

2.4 Considered experiments

Within the scope of this thesis, the experiments with steady and dynamic inflow conditions were analysed and used as benchmarks. For the steady conditions, only the axial flow measurements were considered, thus excluding the yawed configurations.

2.4.1 Axial flow data

The axial flow experimental data covers three distinct cases, characterised mainly by a different TSR:

- **Case 1** - $U = 10.05\ m/s$ and $TSR = 10$,
- **Case 2** - $U = 15.06\ m/s$ and $TSR = 6.7$,
- **Case 3** - $U = 24.05\ m/s$ and $TSR = 4.2$.

In this study, the panel method is applied for Case 1 and Case 2, in order to make a comparison with experimental results.

The choice of discarding Case 3 is based on the experimental pressure measurements, from which is possible to witness flow separation on the blades. Indeed, as can be seen in Figure 2.4, a constant pressure is experienced on the suction side of the blade, which is a typical indicator that flow is not attached (see for example [36]). As mentioned in Section 1.2.3, panel methods can only perform calculations on potential flows, therefore, being flow separation a viscous effect, Case 3 can not be modelled with *PROPAN*.

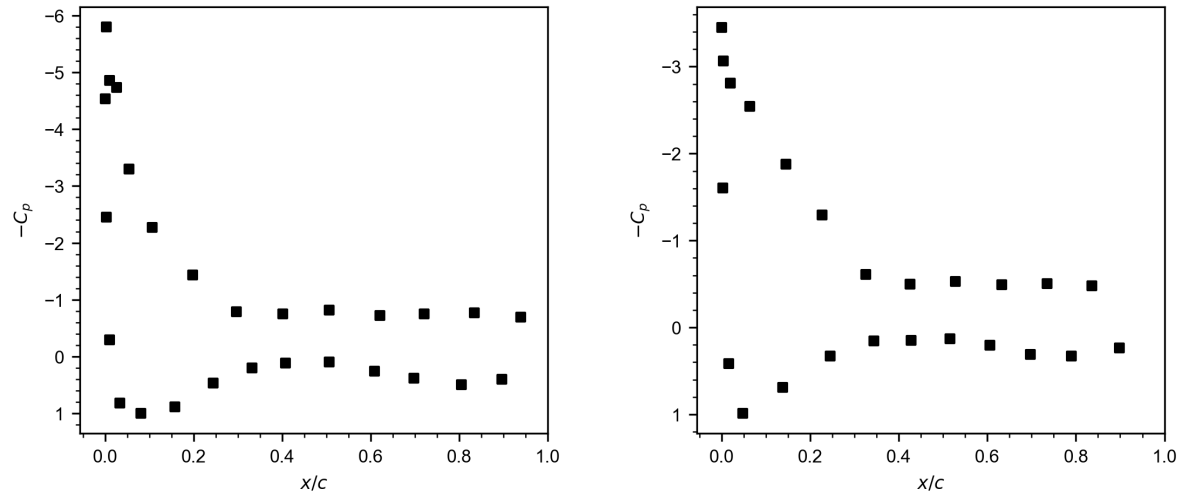

(a) $r/R = 35\%$ (b) $r/R = 60\%$

Figure 2.4: Experimental pressure distribution on the blades in Case 3 [33].

The parameters provided for Case 1 and 2 are summarised in Table 2.3 and Table 2.4, where T_{amb}, p_{amb} and r/R are the ambient temperature, ambient pressure and the dimensionless blade radial position, respectively. F_n and F_t denote forces (per unit length) normal and tangential to the blade section chord.

	$\boldsymbol{\Omega}\ [\boldsymbol{rpm}]$	$\boldsymbol{\Psi}\ [°]$	$\boldsymbol{\rho}\ [\boldsymbol{kg/m^3}]$	$\boldsymbol{U}\ [\boldsymbol{m/s}]$	$\boldsymbol{T_{amb}}\ [\boldsymbol{K}]$	$\boldsymbol{p_{amb}}\ [\boldsymbol{Pa}]$	$\boldsymbol{T}\ [\boldsymbol{N}]$	$\boldsymbol{Q}\ [\boldsymbol{Nm}]$
Case 1	425.1	-2.3	1.197	10.05	293.63	101398	974.4	68.1
Case 2	425.1	-2.3	1.191	15.06	294.91	101345	1663.0	316.7

Table 2.3: New MEXICO axial flow parameters.

	Case 1		Case 2	
r/R [%]	F_n $[N/m]$	F_t $[N/m]$	F_n $[N/m]$	F_t $[N/m]$
25	57.80	1.70	130.9	24.2
35	111.6	1.68	202.7	27.5
60	170.6	3.97	313.7	33.8
82	308.3	6.41	492.5	45.7
92	316.3	11.1	488.2	47.5

Table 2.4: Normal and tangential forces to the blade section chord from axial flow experiment.

The power coefficient C_P and the thrust coefficient C_T are calculated utilising Equation (1.8) and Equation (1.9). In addition, the input files include pressure data for each span position and wind velocity, as a function of the airfoil coordinates.

2.4.2 Dynamic inflow data

The experiments conducted under dynamic inflow conditions were performed changing four key quantities: wind velocity, rotational speed and yaw and pitch angle. Only one blade was instrumented with pressure taps at 25, 35, 60, 82 and 92% radius. Pitch steps of 7.3° have been performed at a maximum pitch rate of 40 °/s.

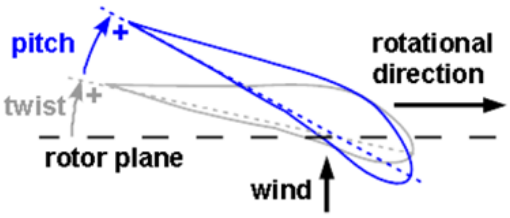

Figure 2.5: New MEXICO pitch axis convention.

Table 2.5 shows the different dynamic configurations set in the experiments.

	U $[m/s]$	$Yaw\ angle$ [°]	Ω $[rpm]$	ρ $[kg/m^3]$
Case A	9.97	0	425.1	1.2088
Case B	10.01	15	425.1	1.2072
Case C	7.68	0	324.9	1.2068
Case D	7.66	15	324.9	1.2068
Case E	7.67	30	425.1	1.2067

Table 2.5: New MEXICO dynamic inflow parameters.

The experimental datasets are composed by a timeseries ranging from 0 to about 15 seconds in which pitch angle, normal and tangential forces at each radial position are given. The case considered for applying the panel method is the first one (Case A), since it matches the aerodynamic conditions (TSR, wind speed and rotational speed) of axial flow Case 1. Indeed, the final grid that has been computed after the numerical tests in the axial flow scenario has been taken as the starting point for

the dynamic scenario. The normal force (F_n) and tangential force (F_t) behaviour extracted from Case A data is shown in Figure 2.6.

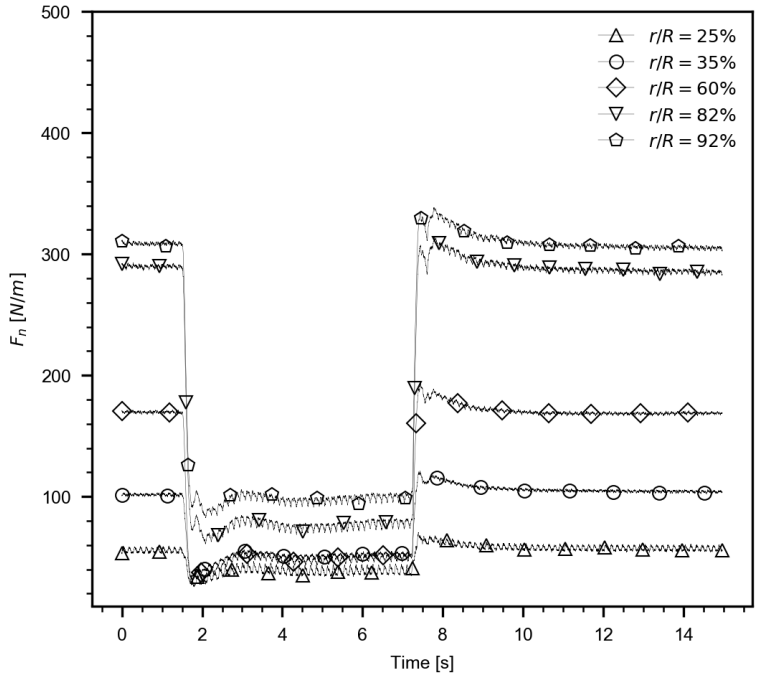

(a) Normal Forces

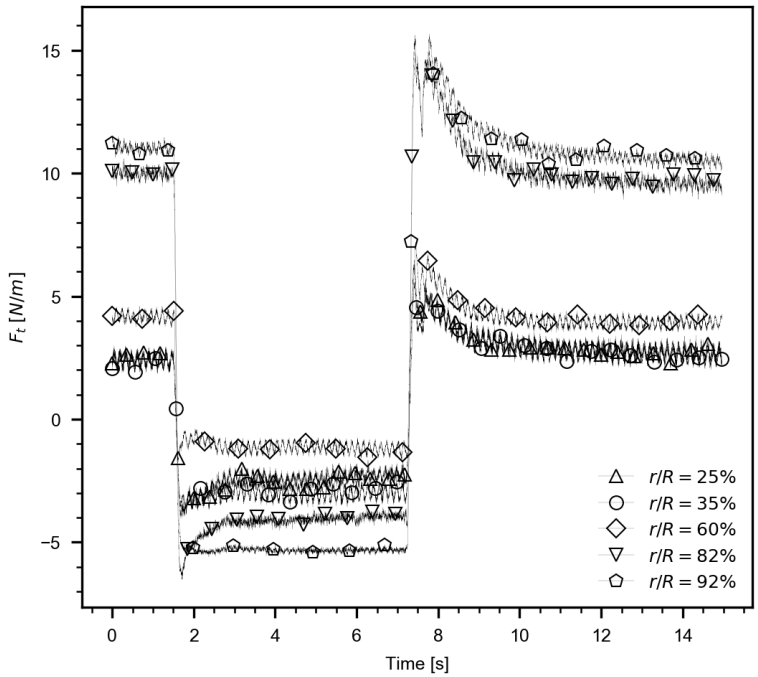

(b) Tangential Forces

Figure 2.6: Normal and tangential forces in Case A [33].

Chapter 3

Numerical method

3.1 Mathematical formulation

Let us consider the rotor of a horizontal axis wind turbine with radius R and K blades symmetrically placed around the rotational axis, rotating with constant angular velocity Ω in an incompressible fluid extending to infinity in all directions. We introduce an inertial earth-fixed Cartesian coordinate system (x_0, y_0, z_0) and a Cartesian coordinate system (x, y, z) rotating with the turbine rotor, as shown in Figure 3.1. The x and x_0 axes coincide with the turbine rotation axis, y_0 and z_0 are at the turbine plane,

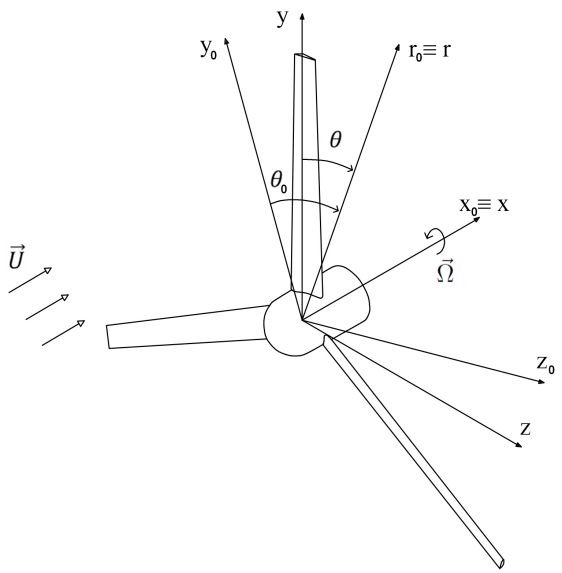

Figure 3.1: Coordinate system of the turbine.

with y_0 pointing upwards. The y axis is coincident with the turbine reference line, passing through the reference point at the root section of the $k = 1$ blade, which represents the key blade, and z completes

the right-hand system. It is worth adding the cylindrical coordinate systems (x_0, r_0, θ_0) and (x, r, θ), with

$$y_0 = r_0 \cos\theta_0, \quad z_0 = r_0 \sin\theta_0, \quad y = r\cos\theta, \quad z = r\sin\theta \tag{3.1}$$

The relation between the two coordinate systems for a rotating right-handed rotor is

$$x_0 = x, \quad r_0 = r, \quad \theta_0 = \theta - \Omega t \tag{3.2}$$

where $\Omega = |\vec{\Omega}|$ and t is the time variable. The key blade reference line coincides with the y_0 axis at $t = 0$.

In the Cartesian reference system (x_0, y_0, z_0) the inflow is assumed to be steady, with the velocity $\vec{U}(x_0, y_0, z_0)$, while in the reference frame rotating with the turbine, the relative velocity field is time dependent and defined as

$$\vec{V}_\infty(x, r, \theta, t) = \vec{U}(x, r, \theta - \Omega t) - \vec{\Omega} \times \vec{x} \tag{3.3}$$

with $\vec{x} = (x, y, z)$.

The fluid flow is assumed to be inviscid and incompressible. The flow field velocity $\vec{V}(x, y, z, t)$ can be described as

$$\vec{V}(x, y, z, t) = \vec{V}_\infty(x, y, z, t) + \nabla\phi(x, y, z, t) \tag{3.4}$$

where $\nabla\phi(x, y, z, t)$ represents the gradient of a scalar perturbation potential equivalent to the irrotational velocity perturbation $\vec{v}(x, y, z, t)$. The potential satisfies the Laplace equation $\nabla^2\phi(x, y, z, t) = 0$.

The boundary of the domain can be divided into two surfaces $\mathcal{S}_\mathcal{B}$ and $\mathcal{S}_\mathcal{H}$, representing the blade and hub, respectively. The perturbation potential needs to satisfy the following boundary conditions:

$$\nabla\phi \to 0, \quad \text{if} \quad r \to \infty \quad \text{and} \quad x \neq +\infty \tag{3.5}$$

and a Neumann boundary condition

$$\frac{\partial\phi}{\partial n} \equiv \vec{n} \cdot \nabla\phi = -\vec{n} \cdot \vec{V}_\infty \quad \text{on} \quad \mathcal{S}_\mathcal{B} \quad \text{and} \quad \mathcal{S}_\mathcal{H} \tag{3.6}$$

where $\partial/\partial n$ denotes differentiation along the normal and $\vec{n}$ is the unit vector normal to the surface directed outward from the surfaces.

When considering circulation around the blades, vortex sheets are shed from the trailing edge of each blade. There are two boundary conditions applying on the wake surface $\mathcal{S}_\mathcal{W}$: the normal component of the fluid velocity is continuous and equal to the normal velocity of the sheet

$$\vec{V}_w \cdot \vec{n} = \vec{V}^+ \cdot \vec{n} = \vec{V}^- \cdot \vec{n} \quad \text{on} \quad \mathcal{S}_\mathcal{W}, \tag{3.7}$$

and the pressure is continuous across the vortex wake

$$p^+ = p^- \quad \text{on} \quad \mathcal{S}_\mathcal{W}, \tag{3.8}$$

where $\vec{V}$ is the fluid velocity, $\vec{V}_w$ the velocity of the points on the wake surface $\mathcal{S}_\mathcal{W}$, p is the static pressure and the indices $+$ and $-$ denote the the upper side and lower side of the vortex sheet. The unit vector normal to the vortex sheet is defined pointing from the lower $-$ to the upper $+$ side of the sheet. In order to define uniquely the circulation around the blade, the following Kutta condition must be imposed at the blade trailing edge

$$|\nabla\phi| < \infty \tag{3.9}$$

3.1.1 Integral equation of a potential flow

Let us assume $\bar{\phi} = 0$ for the interior region to $\mathcal{S}_\mathcal{B}$ and $\mathcal{S}_\mathcal{H}$, with $\bar{\phi}$ denoting the potential in the interior region to $\mathcal{S} = \mathcal{S}_\mathcal{B} \cup \mathcal{S}_\mathcal{H}$. Applying Green's second identity, the perturbation potential at a point p on the body surface can be expressed as

$$2\pi\phi\left(p,t\right) - \iint\limits_{\mathcal{S}_\mathcal{B}\cup\mathcal{S}_\mathcal{H}} \left[G\left(p,q\right)\frac{\partial\phi}{\partial n_q} - \phi\left(q,t\right)\frac{\partial G}{\partial n_q}\right] dS = \iint\limits_{\mathcal{S}_\mathcal{W}} \Delta\phi\left(q,t\right)\frac{\partial G}{\partial n_q} dS \tag{3.10}$$

where $G(p,q) = -1/R(p,q)$, with $R(p,q)$ being the distance between the field point p and the point q on the boundary $\mathcal{S}$. Since $\partial\phi/\partial n_Q$ on the surfaces $\mathcal{S}_\mathcal{B}$ and $\mathcal{S}_\mathcal{H}$ is known from the Neumann boundary condition on the body surface (Equation (3.6)), the Equation (3.10) is a Fredholm integral equation of the second kind in the dipole distribution $\mu(q,t) = -\phi(q,t)$ on the surfaces $\mathcal{S}_\mathcal{B}$ and $\mathcal{S}_\mathcal{H}$. The Kutta condition, Equation (3.9), yields the additional relationship between the dipole strength in the $\Delta\phi\left(q,t\right)$ wake and the surface dipole strength at the blade trailing edge.

3.1.2 Wake boundary conditions

The two boundary conditions on the wake are expressed by Equation (3.7) and Equation (3.8). The former implies that the vortex sheet moves with the fluid. If $S_w(\vec{x},t)$ denotes the equation of the vortex sheet surface $\mathcal{S}_\mathcal{W}$, then

$$\frac{\partial S_w}{\partial t} + \vec{V}^+ \cdot \nabla S_w = \frac{\partial S_w}{\partial t} + \vec{V}^- \cdot \nabla S_w = 0 \tag{3.11}$$

Outside of the vortex sheet the Bernoulli equation for incompressible potential flow is

$$\frac{\partial\phi}{\partial t} + \frac{p}{\rho} + \frac{1}{2}|\vec{V}|^2 = \frac{p_\infty}{\rho} + \frac{1}{2}|\vec{V}_\infty|^2 \tag{3.12}$$

where p_∞ is the pressure of the undisturbed inflow and ρ the fluid density. Applying consecutively the Bernoulli equation at a given point on each side of the vortex sheet and subtracting:

$$\frac{\Delta p}{\rho} = -\frac{\partial(\Delta\phi)}{\partial t} - \frac{1}{2}\left(\left|\vec{V}^+\right|^2 - \left|\vec{V}^-\right|^2\right) \tag{3.13}$$

where $\Delta p = p^+ - p^-$ and $\Delta\phi = \phi^+ - \phi^-$ are the pressure and potential jumps across the sheet, respectively. From the boundary condition, Equation (3.8), the pressure-jump is zero, thus

$$\frac{\partial(\Delta\phi)}{\partial t} = -\frac{1}{2}\left(\left|\vec{V}^+\right|^2 - \left|\vec{V}^-\right|^2\right) \tag{3.14}$$

and knowing that

$$\left|\vec{V}^+\right|^2 - \left|\vec{V}^-\right|^2 = \left(\vec{V}^+ + \vec{V}^-\right)\cdot\left(\vec{V}^+ - \vec{V}^-\right), \tag{3.15}$$

it is possible to simplify Equation (3.12) as

$$\frac{\partial(\Delta\phi)}{\partial t} + \vec{V}_m \cdot \Delta\vec{V} = 0 \tag{3.16}$$

where $\vec{V}_m = \frac{1}{2}(\vec{V}^+ + \vec{V}^-)$ denotes the mean velocity and $\Delta\vec{V} = \vec{V}^+ - \vec{V}^-$ represents the velocity discontinuity on the wake surface. Using Equation (3.7), the velocity discontinuity may be written as the surface gradient of the potential discontinuity,

$$\frac{\partial(\Delta\phi)}{\partial t} + \vec{V}_m \cdot \nabla_S(\Delta\phi) = 0 \tag{3.17}$$

where $\nabla_S = -\vec{n}\times(\vec{n}\times\nabla)$ denotes the surface gradient. Equation (3.17) shows that the potential-jump remains constant following a fluid particle moving on the wake with the velocity $\vec{V}_m$.

In the general case, the instantaneous location of the wake has to be derived from Equation (3.11) and the dipole strength from Equation (3.17), which requires following the motion of the vortex sheet S_W in the unsteady flow velocity field. In this work a considerable simplification is introduced assuming a constant V_m equal to the undisturbed time averaged axisymmetric inflow. In the cylindrical coordinate system (x, r, θ),

$$\vec{V}_m = \left(\bar{U}(r), 0, \Omega r\right) \tag{3.18}$$

where $\bar{U}(r)$ is the zero harmonic of the axial inflow at the given radius, and Equation (3.17) becomes

$$\frac{\partial(\Delta\phi)}{\partial t} + \Omega\frac{\partial(\Delta\phi)}{\partial\theta} = 0 \tag{3.19}$$

The solution of Equation (3.19) is of the form $\Delta\phi(r,\theta,t) = \Delta\phi(r,t^*)$ with $t^* = t^*(\theta,t)$ being a characteristic convection time. If we consider $\theta = \theta_{te}$ at $t = 0$, where te stands for "trailing edge", we obtain

$$\Delta\phi(r,\theta,t) = \Delta\phi\left(r, t - \frac{\theta-\theta_{te}}{\Omega}\right) \tag{3.20}$$

Only the tangential induced velocity is neglected in the convection of vortices. The initial condition in the wake is

$$\Delta\phi(r,\theta,0) = \Delta\phi_{te}\left(r,0\right) = -\Gamma\left(r,0\right) \tag{3.21}$$

with Γ being the flow circulation for a circuit around the blade intersecting the wake at the blade trailing edge.

It is necessary to clarify that Equation (3.18) implies that the wake is aligned to the mean flow velocity field, which is not the actual case of this work where an empirical rigid wake is considered. However, Equation (3.19) is still used to compute the wake dipole strength.

3.1.3 Calculation of Velocity, Pressure and Forces

From the potential solution on the surface the covariant surface velocity components are calculated by means of a second order differentiation scheme of the potential relative to the arc lengths on the body surface grid. The pressure on the surface is obtained from the Bernoulli Equation (3.12). The pressure coefficient can be defined as

$$C_p = \frac{p - p_\infty}{1/2\rho V_\infty^2}, \tag{3.22}$$

with $V_\infty = |\vec{V}_\infty|$. The components of the inviscid force acting on the blades are obtained by integration of the pressure distribution on the blade surface. The integrated force is

$$\vec{F} = -\iint_{\mathcal{S}_\mathcal{B}} p\vec{n}\, dS, \tag{3.23}$$

and the moment is

$$\vec{M} = -\iint_{\mathcal{S}_\mathcal{B}} p(\vec{n} \times \vec{x})\, dS. \tag{3.24}$$

3.2 Panel method

3.2.1 Integral equation discretisation

The numerical solution of the integral equation (3.10) is obtained using a low-order panel method in the time domain at the time steps $n = t/\Delta t$, where Δt is the constant time step. The body surfaces $\mathcal{S}_\mathcal{B} \cup \mathcal{S}_\mathcal{H}$ and the wake surface $\mathcal{S}_\mathcal{W}$ are discretised in quadrilateral panels having a hyperboloidal-shaped surface. The integrals over $\mathcal{S}_\mathcal{B}$ and $\mathcal{S}_\mathcal{H}$ are approximated by the summation of the integrals on the panels discretising the surfaces, assuming a constant strength of the dipole and source distributions on each panel. On the wake surface $\mathcal{S}_\mathcal{W}$ piecewise linear or constant dipole distributions are assumed, depending on the specific location of the panel.

Let $\mu_j^k(n) = -\phi_j^k(n)$ be the values at time step n of the dipole strength of the panel S_j^k on the surface of the k^{th} blade-hub sector, with $k = 1, \ldots, K$, $j = 1, \ldots, N$, and N being the number of panels on each blade-hub sector; let $\mu_{ml}^k(n) = -\Delta\phi_{ml}^k(n)$ be the values at time step n of the dipole strengths of the boundary between the panel $S_{m,l-1}^k$ and the panel S_{ml}^k of the k^{th} wake sector, with $m = 1, \ldots, N_R$, $l = 1, \ldots, N_W$, N_R being the number of panels along the spanwise direction and N_W the number of panels along the streamwise direction of the wake; let $\sigma_j^k(n)$ be the source strength of the panel S_j^k on the surface of the k^{th} blade-hub sector. If, at each time step n, Equation (3.10) is satisfied on the centre points P_i, $i = 1, \ldots, N_P$ of the $N_P = N \times K$ panels on the surface of the K blade-hub sectors, the

so-called collocation points, it is possible to obtain a system of algebraic equations in the form

$$\sum_{k=1}^{K}\sum_{j=1}^{N}\left(\delta_{ij}-D_{ij}^{k}\right)\phi_{j}^{k}(n)-\sum_{k=1}^{K}\sum_{m=1}^{N_R}\sum_{l=1}^{N_W}W_{iml}^{k}\Delta\phi_{ml}^{k}(n)=\sum_{k=1}^{K}\sum_{j=1}^{N}S_{ij}^{k}\sigma_{j}^{k}(n),\quad i=1,\ldots,N_P, \tag{3.25}$$

in which δ_{ij} is the Kronecker delta and D_{ij}^{k} and S_{ij}^{k} are the influence coefficients given by

$$\begin{aligned} D_{ij} &= \tfrac{1}{2\pi}\iint_{S_j^k}\tfrac{\partial}{\partial n_Q}\left(\tfrac{1}{R(p_i,q)}\right)dS \\ S_{ij} &= \tfrac{1}{2\pi}\iint_{S_j^k}\tfrac{1}{R(p_i,q)}dS \end{aligned} \tag{3.26}$$

and W_{iml}^{k} is a wake influence coefficient which may be written as a linear combination of elementary integrals of the dipole type. These coefficients are calculated analytically following the formulation of Morino and Kuo [17]. The detailed mathematical procedure can be viewed in [32]. The source strength $\sigma_{k}^{k}(n)$ is determined from the boundary condition, Equation (3.6), as

$$\sigma_{k}^{k}(n)=-\vec{n}_{j}^{k}\cdot\vec{V}_{\infty}(r_{j}^{k},\theta_{j}^{k},n\Delta t) \tag{3.27}$$

with $\vec{n}_{j}^{k}$ denotes the unit vector at the control point $(x_{j}^{k},r_{j}^{k},\theta_{j}^{k})$ of the k^{th} blade. In order to reduce the dimension of the system of equations, the boundary condition is only applied at the key blade $k=1$, therefore the contributions of the other blades are assumed to be known when solving for the key blade.

In the general case of a non-uniform axial inflow field, the solution in the rotating frame is periodic in time with a period, in general, equal to the time of a turbine revolution. We introduce the angular time step $\Delta\theta=\Omega\Delta t$. The total number of time steps is $N_t=N_{rev}\times N_\theta$, where N_{rev} is the number of revolutions for the time integration and $N_\theta=2\pi/\Delta\theta$ is the total number of angular steps per revolution.

3.2.2 Calculation of Forces

The axial force T and the torque Q on the rotor are obtained by integration of the pressure distribution on the blade surfaces. Let (n_x,n_y,n_z) be the Cartesian components of the outward unit normal $\vec{n}$. Recalling Equation (3.23) and Equation (3.24), applying symmetry considerations, the thrust T can be expressed as

$$T=\iint_{S_B}pn_x dS, \tag{3.28}$$

and the torque Q as

$$Q=\iint_{S_B}p\left(n_y z-n_z y\right)dS. \tag{3.29}$$

3.2.3 Wake models

In this thesis two wake models are utilised, a rigid wake and an aligned wake. The former is characterised by a fixed geometry where the vortex lines are empirically prescribed, while the latter comprehends an

iterative alignment based on the pitch modification on the wake vortices. For both models, the contraction or expansion of the wake geometry is not allowed.

Rigid wake

In this model the wake generation is based upon empirical knowledge which allows to specify the geometry of the wake surface. The dipole strength at the wake surface can be related to the potential discontinuity at the blade trailing edge by the application of the so-called Morino Kutta condition [17], written in the form

$$\Delta\phi = \phi^{+} - \phi^{-}, \tag{3.30}$$

in which ϕ^{+} and ϕ^{-} are the values of the potentials at the trailing edge, respectively on the upper and lower sides of the blade.

It is possible to formulate an alternative condition by implementing an iterative pressure Kutta condition, which replaces Equation (3.30) by imposing equal pressure on both sides of the blade at the trailing edge. Due to the non-linear character of the pressure, the application of the condition for the pressure equality on the control points on the panels adjacent to the trailing edge gives origin to a non-linear system of equations, that can be solved by the method of Newton-Raphson (more details in [32]).

Aligned wake

In this model the corner points of the blade wake grid panels are displaced with the mean fluid velocity. At the $(h+1)^{\text{th}}$ iteration, the geometry in cylindrical coordinates of the wake strip $i+1$ can be determined by using an Euler scheme [37]:

$$\begin{aligned}
x_{i+1}^{(h+1)} &= x_i^{(h)} + V_x\left(x_i^{(h)}, r_i^{(h)}, \theta_i^{(h)}\right)\Delta t,\\
r_{i+1}^{(h+1)} &= r_i^{(h)} + V_r\left(x_i^{(h)}, r_i^{(h)}, \theta_i^{(h)}\right)\Delta t,\\
\theta_{i+1}^{(h+1)} &= \theta_i^{(h)} + \frac{V_\theta\left(x_i^{(h)}, r_i^{(h)}, \theta_i^{(h)}\right)\Delta t}{r_i^{(h)}},
\end{aligned} \tag{3.31}$$

where V_x, V_r and V_θ are the components of the mean vortex sheet velocity along the axial, radial, and circumferential directions, respectively, and Δt is the time step for the Euler vortex convection scheme. The velocity components are calculated from the integral equation of the velocity, derived from Equation (3.25). The first wake strip ($i = 1$) corresponds to the blade trailing edge. To control the wake alignment stability, the radial coordinates of the blade wake grid are kept constant during the iterative process. Hence,

$$r_{i+1}^{(h+1)} = r_i^{(h)} + \Delta r_i^{(h)}, \tag{3.32}$$

with

$$\Delta r_i^{(h)} = r_{i+1}^{(0)} - r_i^{(0)}. \tag{3.33}$$

Therefore, Equation (3.31) becomes:

$$\begin{aligned} x_{i+1}^{(h+1)} &= x_i^{(h)} + V_x\left(x_i^{(h)}, r_i^{(h)}, \theta_i^{(h)}\right)\Delta t, \\ r_{i+1}^{(h+1)} &= r_i^{(h)} + \Delta r_i^{(h)}, \\ \theta_{i+1}^{(h+1)} &= \theta_i^{(h)} + \frac{V_\theta\left(x_i^{(h)}, r_i^{(h)}, \theta_i^{(h)}\right)\Delta t}{r_i^{(h)}}. \end{aligned} \tag{3.34}$$

To clarify, the fluid velocity components are not computed for all wake strips. Indeed, two wake regions are defined:

- Transition wake - up to a position x_{fw}, where variations of the wake geometry take place;
- Ultimate wake - from x_{fw} to an ultimate section x_{uw}, where the wake parameters remain constant.

In the transition wake a set of alignment sections are defined, both on the axial (X_V) and radial (J_V) directions, where the above-mentioned fluid velocities are calculated. A linear interpolation for the velocities at the corner points of the remaining panels is then assumed.

3.2.4 Viscous effects

In order to consider the viscous effects, it is possible to apply quasi-steady corrections to the inviscid axial force and power calculated with the panel method [21]. Bearing in mind the velocity triangle shown in BEM theory section (Section 1.2.1, Figure 1.4), the viscous forces on the turbine blades are calculated using the concept of section lift and drag force that can be derived from two-dimensional lift and drag data. In particular, the inflow angle β_i is linked to the inviscid thrust T_i and torque Q_i by the relation

$$\tan\beta_i = \frac{dQ_i}{r dT_i} \tag{3.35}$$

and the angle of attack can be derived as $\alpha = \beta_i - \psi$, where ψ is the pitch angle. The angle of attack is key to extract experimental data of the lift and drag coefficient, C_L and C_D respectively.

The viscous thrust T_v and torque Q_v are then expressed as

$$dT_v = (L_v\cos\beta_i + D\sin\beta_i)dr, \tag{3.36}$$

$$dQ_v = (L_v\sin\beta_i - D\cos\beta_i)dr \tag{3.37}$$

where the viscous lift L_v is given as

$$L_v = L_i\frac{C_{L_v}}{C_{L_i}} \tag{3.38}$$

and the drag D as

$$D = \frac{1}{2}\rho C_D V^2 c \tag{3.39}$$

In Equation (3.39), the velocity V can be calculated by the Kutta-Joukowski law in steady flow:

$$L_i = \rho V\Gamma \tag{3.40}$$

A graphical representation of the forces acting on a blade section is shown in Figure 3.2. As one might suppose, the presence of viscosity causes a reduction in the lift force on the blade which, together with the presence of drag, ultimately leads to diminish the resultant force F_{res}.

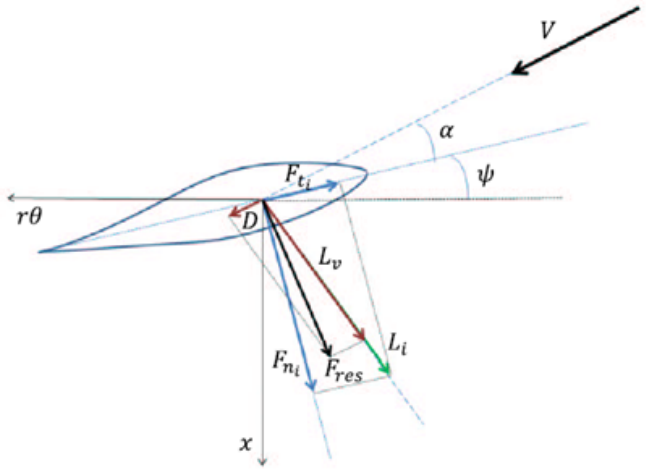

Figure 3.2: Blade velocity triangle with viscous effects.

In this work, the correction on the lift force (Equation (3.38)) is neglected for simplicity, thus the viscous thrust and torque (Equation (3.36) and (3.37)) become

$$dT_v = (L_i \cos\beta_i + D \sin\beta_i)dr, \tag{3.41}$$

$$dQ_v = (L_i \sin\beta_i - D \cos\beta_i)dr \tag{3.42}$$

Chapter 4

Grid generation

The creation of the 3D model and grid of the New MEXICO wind turbine is presented in this chapter. Since *PROPAN* code was first developed for marine propellers, which have different conventions on some geometrical parameters, corrections and adjustments have been made to the original information provided in [34] to be able to accurately replicate the correct geometry. Moreover, *PROPAN* is not directly used to generate the geometry and grid, whereas a secondary code called *ProPanel* was developed for that purpose.

4.1 Geometry creation

4.1.1 Blade

The definition of the blade geometry lies on the profile definition given in Figure 2.2 and Table 2.2. For each given radial position a set of parameters based on different geometrical correlations needs to be calculated. Table 4.1 shows and describes all the required parameters for every single radial position, providing a brief explanation of all of them. As mentioned previously, some of them are defined with a

Symbol	Unit	Description
r/R	[-]	Dimensionless radial position
c/D	[-]	Blade section chord divided by rotor diameter
p/D	[-]	Blade section pitch divided by rotor diameter
it/D	[-]	Blade section rake divided by rotor diameter (positive pointing downstream from rotor plane)
θ	[°]	Blade section skew angle (positive in the negative rotation direction)
t_{max}/D	[-]	Blade section maximum thickness divided by rotor diameter
f_{max}/D	[-]	Blade section maximum camber divided by rotor diameter

Table 4.1: Input parameters for definition of the blade geometry.

notation typical for propellers, such as blade section rake and skew angle. The former denotes the fore or aft slant of a blade with respect to the rotor plane, while the latter the transverse sweeping of a blade such

that viewing the blades from fore or aft shows an asymmetrical shape [38]. A clear representation of both is given in Figure 4.1 and Figure 4.2, respectively. In addition to the these geometrical characteristics,

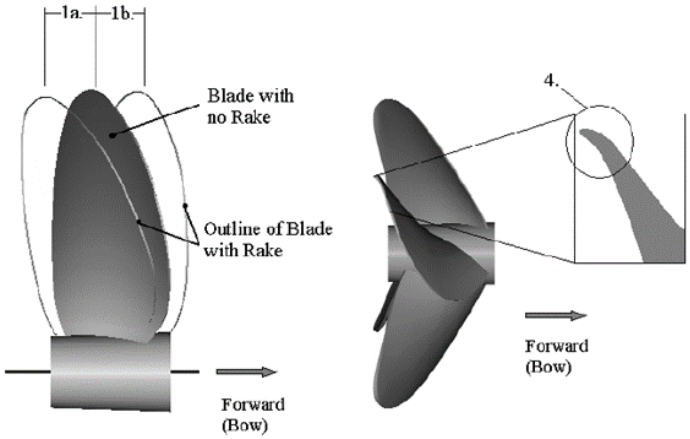

Figure 4.1: Blade section rake. 1a) Aft rake - blade slant towards aft end of hub; 1b) Forward rake - blade slant towards forward end of hub [38].

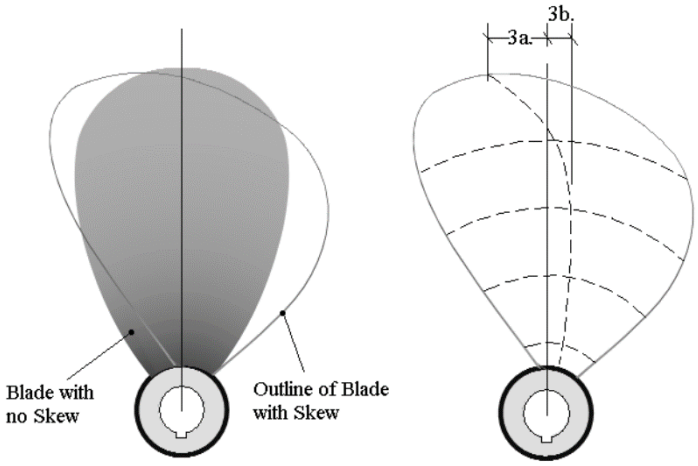

Figure 4.2: Blade section skew. 3a) Aft skew - blade sweep in direction opposite of rotation; 3b) Forward skew - blade sweep in same direction as rotation [38].

all the airfoil profiles that compose the blades must be specified. More in detail, one must consider the (x, y) coordinates of the lower and upper airfoil surface (divided by the chord length) and append them to a text file including the parameters of Table 4.1. The geometrical profile of each airfoil is shown in Figure 4.3 (the RISØ A2-21 profile cannot be shown due to confidentiality reason). The geometry of the transition zones between the airfoils is automatically derived through *ProPanel* by interpolation, that can be linear, quadratic or cubic.

Additional blade sections

In order to minimise the oscillations in the blade surface, different additional sections have been included in the transition zones. This plays a key role in the transition zone between the blade root (cylinder) and the DU91-W2-250 airfoil, where the blade shape changes drastically. Two different approaches were

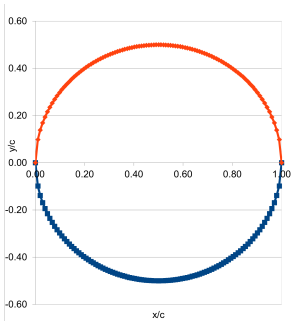

(a) Cylinder

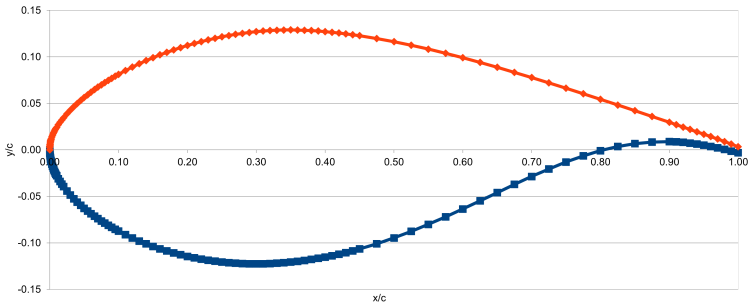

(b) DU91-W2-250

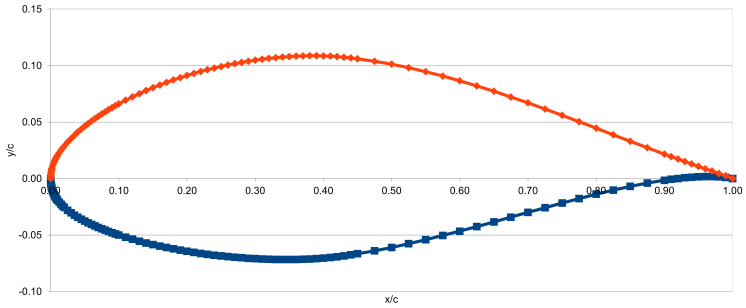

(c) NACA64-418

Figure 4.3: Cylinder, DU91-W2-250 and NACA64-418 profiles.

applied:

- Data points extraction with a CAD software,
- Linear interpolation using a python script.

The first method was utilised for the first transition zone because it was the most precise way to insert extremely accurate sections. The given CAD model of the blade was manipulated with the commercial software *Solid edge*, thanks to which it was possible to:

1. clip the model at specific radial positions (Figure 4.4(a)),
2. create circles centred along the border of the section (Figure 4.4(b)),
3. extract the (x, y) coordinates of the circle centres.

The second method, simpler than the first one, was used for the second and third transition zone where there is not a sharp section change. A python script was created with the possibility of importing two airfoil geometries as inputs and outputting as many interpolated sections as specified. Linear, quadratic and cubic interpolations were tested, resulting in no major difference among them, therefore a basic linear interpolation was considered. In total eight sections were added to the original blade model (see Appendix A), three in the first transition zone, two in the second one and three in the last one, as shown in Table 4.2. The chord and twist angle of the added profiles were calculated by linear interpolation.

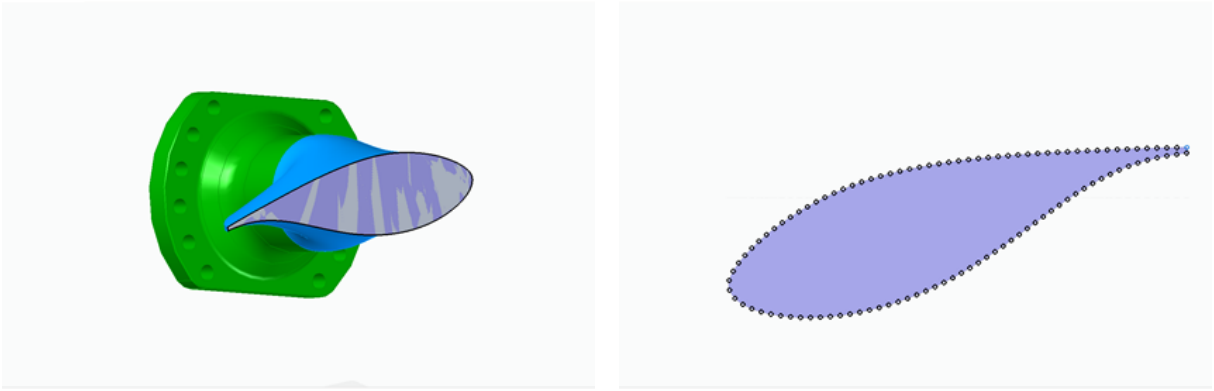

(a) Clip (b) Extraction

Figure 4.4: CAD blade model manipulation.

Radius [m]	**Chord** [m]	**Twist** [°]	**Profile name** [-]
0.000	0.195	0.000	Cylinder
0.020	0.195	0.000	Cylinder
0.025	0.090	0.000	Cylinder
0.090	0.090	0.000	Cylinder
0.150	**0.158**	**7.489**	**Section 1A**
0.187	**0.219**	**14.095**	**Section 2A**
0.210	**0.236**	**15.992**	**Section 3A**
0.240	0.240	16.400	DU91-W2-250
0.465	0.207	12.100	DU91-W2-250
0.690	0.178	8.300	DU91-W2-250
0.815	0.166	7.100	DU91-W2-250
0.882	**0.161**	**6.433**	**Section 1B**
0.948	**0.155**	**5.900**	**Section 2B**
1.015	0.150	5.500	RISØ A2-21
1.140	0.142	4.800	RISØ A2-21
1.265	0.134	4.000	RISØ A2-21
1.315	**0.132**	**3.850**	**Section 1C**
1.365	**0.129**	**3.700**	**Section 2C**
1.415	**0.126**	**3.450**	**Section 3C**
1.465	0.123	3.200	NACA64-418
1.590	0.116	2.600	NACA64-418
1.815	0.102	1.500	NACA64-418
1.955	0.092	0.700	NACA64-418
1.983	0.082	0.469	NACA64-418
2.012	0.056	0.231	NACA64-418
2.040	0.011	0.000	NACA64-418

Table 4.2: New MEXICO blade geometric properties with additional sections.

4.1.2 Hub

The hub geometry was derived by taking into considerations the technical drawings presented in [34]. Its geometry can be decomposed in three sub-geometries: a cylinder, a truncated cone and a sphere. The former makes up the main body of the hub while the other two parts define the nose of the hub (Figure 4.5). The main geometric inputs that *ProPanel* needs to create the hub are:

- Number of input points of hub,
- Axial coordinates of hub input points divided by the rotor radius,
- Radial coordinates of hub input points divided by the rotor radius.

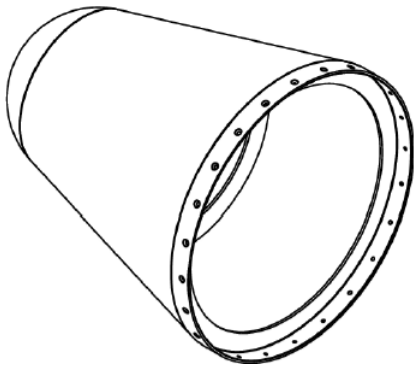

Figure 4.5: Geometry of the hub nose [34].

The reference coordinate system (x, y, z) has the origin at the center of the rotor of the blades. In order to extract the radial position of the truncated cone, one must consider the Cartesian equation of a generic cone with the axis parallel to the x-axis, which is

$$\frac{(y - y_V)^2}{b^2} + \frac{(z - z_V)^2}{c^2} = \frac{(x - x_V)^2}{a^2} \tag{4.1}$$

where (x_V, y_V, z_V) are the coordinates of the vertex and (a, b, c) denote the length of the semi-axis along the x, y and z axis, respectively. Regarding the end of the hub, the Cartesian equation of a sphere is

$$(x - x_C)^2 + (y - y_C)^2 + (z - z_C)^2 = r_s^2 \tag{4.2}$$

with (x_C, y_C, z_C) being the coordinate of the center of the sphere and r_s its radius.

After geometrical considerations, Equation (4.1) can be simplified as

$$y^2 + z^2 = \frac{b^2(x - x_V)^2}{a^2} \tag{4.3}$$

where $b = c$. Once an axial position x is specified, Equation (4.3) becomes the equation of a circle with radius $r = \frac{b}{a}(x - x_V)$. In the same way, Equation (4.2) is modified as

$$y^2 + z^2 = r^2 - (x - x_C)^2 \tag{4.4}$$

and the circle obtained by specifying x has a radius $r = \sqrt{r_s^2 - (x - x_C)^2}$. In total, 27 input points have been taken into account for the hub model generation.

4.1.3 Wake

As mentioned in Section 3.2.3, two wake models have been utilised in this work. In both of them, the wake geometry definition depends on the following fundamental quantities:

- Number of input radii,
- Input radii divided by the rotor radius,
- Wake pitch at the trailing edge divided by the rotor diameter,
- Wake pitch at the ultimate wake (downstream) divided by the rotor diameter,
- Dimensionless wake length.

The first three items correspond to the same parameters expressed for the blade geometry definition (Table 4.1) while the wake pitch at the ultimate wake region and the wake length are based on assumptions.

In the wake alignment model, the geometrical wake pitch is iteratively calculated and adjusted to attain a geometry aligned to the local fluid velocity. On the other hand, in the rigid wake model, the geometry is kept fixed once the above-mentioned parameters are specified, therefore only with precise assumptions it is possible to create a realistic wake geometry. To overcome this issue, additional features might be implemented in the rigid wake model: if the wake geometry is known *a priori* at some specific axial positions in the streamwise direction, then the radial and pitch distributions of the wake at those positions can be extracted and converted as inputs for *ProPanel*.

4.2 Geometry panelling

4.2.1 Blade

The discretisation of the blade consists of setting a number of strips along the spanwise radial direction, extending chordwise from the blade leading edge to the trailing edge.

Considering radial coordinates made non-dimensional by the blade radius R, let r_h be the non-dimensional hub radius and r_t the non-dimensional maximum blade tip radius. The maximum tip radius is chosen as $r_t = 1$, unless specified otherwise. The interval $r_h \leq r \leq r_t$ is divided into N_R strips. The radii of the panel corner points are given by a modified cosine distribution

$$r_j = \frac{1}{\cos\alpha_h + \cos\alpha_t} \left[(r_h \cos\alpha_t + r_t \cos\alpha_h) - (r_t - r_h)\cos\varphi_j \right], \tag{4.5}$$

with

$$\varphi_j = \alpha_h + j\frac{(\pi - \alpha_t - \alpha_h)}{N_R},\ j = 0, 1, \ldots, N_R, \tag{4.6}$$

where α_h, α_t are two parameters controlling the radial size of the panels close to the hub and tip, respectively.

The distribution of coordinates s_{ij}/c_j of the panel corner points along the chord of the strip j is given by the modified cosine distribution

$$\frac{s_{ij}}{c_j} = \frac{\cos\alpha_{le} - \cos\varphi_i}{\cos\alpha_{le} + \cos\alpha_{te}},\ i = 0, 1, \ldots, N_C,\ j = 0, 1, \ldots, N_R, \tag{4.7}$$

where

$$\varphi_i = \alpha_{le} + i\frac{(\pi - \alpha_{te} - \alpha_{le})}{N_C},\ i = 0, 1, \ldots, N_C, \tag{4.8}$$

$c_j = c(r_j)$ and N_C is the number of panels along the chord. The parameters α_{le} and α_{te} control the panel size in the chordwise direction close to the leading edge and trailing edge, respectively.

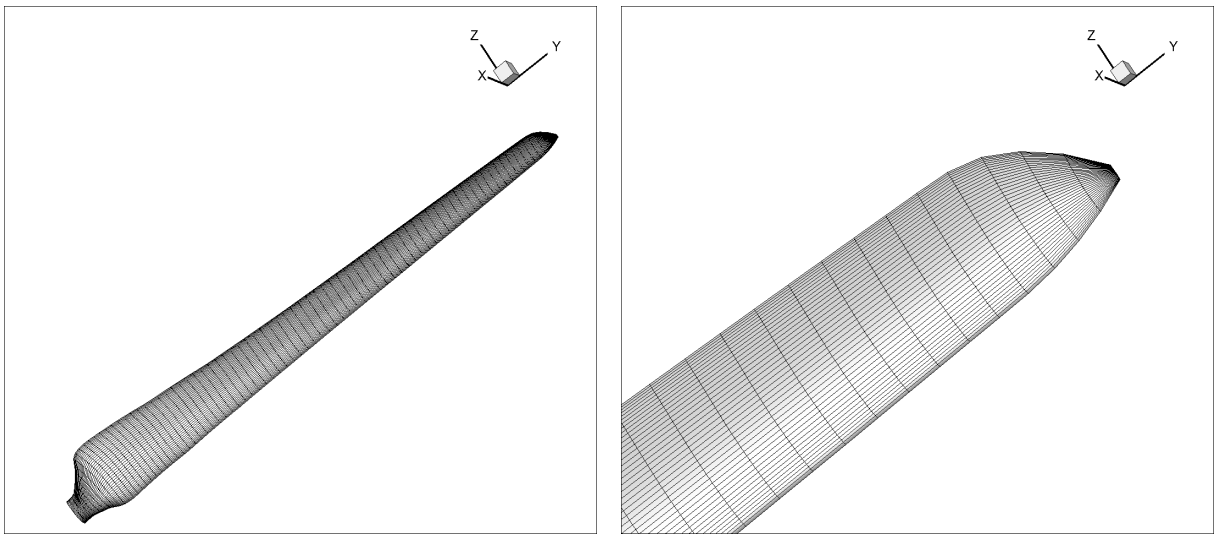

(a) Blade (b) Blade tip

Figure 4.6: Blade grid example ($N_R = 80$ and $N_C = 80$).

4.2.2 Hub

The hub surface is divided into three distinct regions: the region upstream the blades ($x_{H0} \leq x < x_{H1}$), the region between the blades ($x_{H1} \leq x \leq x_{H2}$) and the region downstream the blades ($x_{H2} < x \leq x_{H3}$). The regions upstream and downstream of the blades are discretised with N_{hu} and N_{hd} panels along the axial direction, respectively. The region between the blade leading and trailing edges is discretised with N_C panels along the axial direction. In addition to these three regions, the hub surface is also discretised in the circumferential direction with N_{ht} panels.

For the hub grid, an elliptical grid generator is used, as described by Eça [39]. The method solves a system of elliptic partial differential equations for the curvilinear coordinates with Dirichlet or Neumann-Dirichlet boundary conditions.

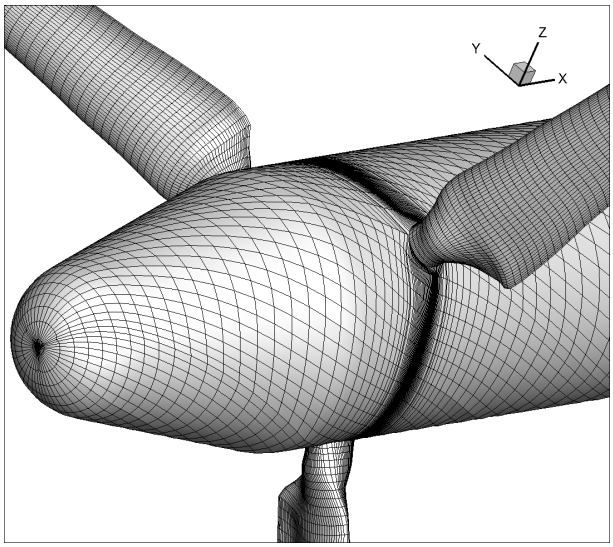

Figure 4.7: Hub grid example ($N_{hu} = 30$, $N_{hd} = 45$, $N_C = 80$ and $N_{ht} = 8$).

4.2.3 Wake

The helicoidal blade wake is discretised in the spanwise direction into N_{R_W} panel strips, with N_W panels for each strip. As mentioned in Section 3.2.3, the blade wake is divided into two regions: the transition wake region and the ultimate wake region. Contraction and variation of the helicoidal lines are not considered. The coordinates of the panel corner points on the blade wake are given by

$$\begin{aligned} x_{ij} &= x_{0j} + \left[1 - \cos\left(i\frac{\pi}{2N_W}\right)\right] x_W \\ r_{ij} &= r_{0j} \\ \theta_{ij} &= \theta_{i-1,j} + \frac{a(\xi)}{N_\theta} \\ i &= 0, 1, \ldots, N_W,\ j = J_I, \ldots, J_F \end{aligned} \tag{4.9}$$

where J_I and J_F represent the initial and final wake strip, respectively, and $J_F - J_I = N_{R_W} - 1$. Thus, the wake grid can be created not necessarily for all the blade span, but also for a smaller internal region (Figure 4.9). The variations of the pitch of the helicoidal lines in the transition wake region can be approximated utilising a cubic Hermite interpolation:

$$a(\xi) = a_{0j}\xi_1 + \frac{da_{0j}}{d\xi}\xi_2 + a_u\xi_3 + \frac{da_u}{d\xi}\xi_4, \tag{4.10}$$

where

$$\begin{aligned} \xi_1 &= 2\xi^3 - 3\xi^2 + 1, \\ \xi_2 &= \xi^3 - 2\xi^2 + \xi, \\ \xi_3 &= -2\xi^3 + 3\xi^2, \\ \xi_4 &= \xi^3 - \xi^2, \end{aligned} \tag{4.11}$$

with

$$\begin{matrix} \frac{da_{0j}}{d\xi} = 3, \\ \frac{da_u}{d\xi} = 0, \end{matrix} . \tag{4.12}$$

and

$$\xi = \frac{i-1}{N_\theta - 1}. \tag{4.13}$$

x_{0j}, r_{0j}, a_{0j} represent the axial coordinate, the radial coordinate and the pitch at the trailing edge of the blade, respectively. a_u represents the pitch at the position where the ultimate wake region starts.

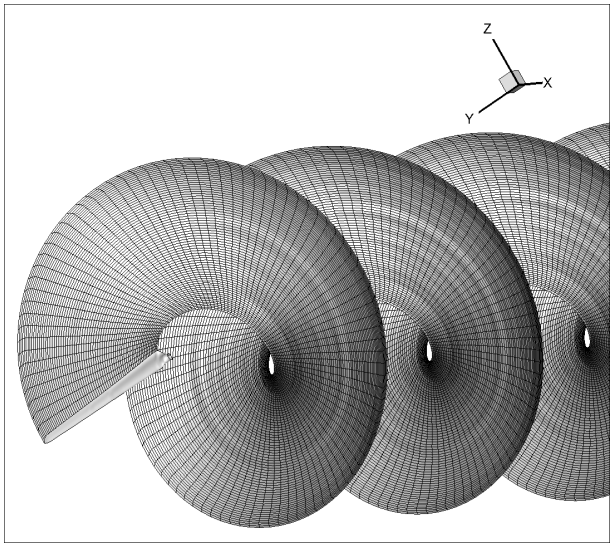

Figure 4.8: Wake grid shed from one blade ($N_R = 80$, $N_{R_W} = 69$, $N_C = 80$ and $N_W = 1080$).

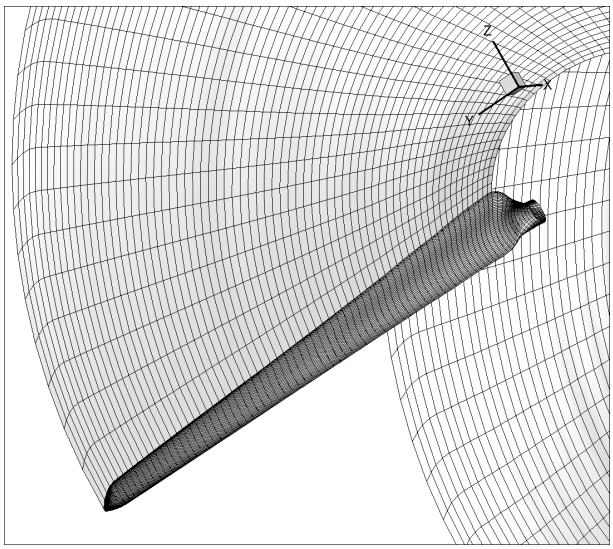

Figure 4.9: Wake grid not covering the whole blade span ($N_R = 80$, $N_{R_W} = 69$, $N_C = 80$ and $N_W = 1080$).

Chapter 5

Results

In this chapter the results obtained from the steady and dynamic cases are presented. Regarding the steady calculations, a detailed numerical study has been performed with wind velocities of $10.05\ m/s$ ($TSR = 10$) and $15.06\ m/s$ ($TSR = 6.7$) using the wake alignment model (Section 3.2.3), in order to define the best blade, hub and wake grids in terms of grid plot convergence, smoothness of wake geometry (surface) and viscous C_P and C_T. The outcomes of this study have been essentials to create the inputs for the dynamic simulations.

5.1 Numerical tests under steady inflow conditions

5.1.1 Simulation set-up

As for the majority of the computational works, the simulation process comprehends three main stages. The first one is the pre-processing phase, where geometrical and grid information of the turbine must be generated. The second step is the processing phase, where the main calculations happen, while the last one is the post-processing phase, where the viscous corrections are introduced from the inviscid predictions through additional easy-to-apply calculations. A more specific explanation for each of these steps is given below.

Pre-processing

This phase is needed to generate the turbine geometry and grid. Since the flow is in steady conditions, the mathematical formulation presented in Chapter 3 becomes independent of the time variable, therefore initial conditions such as the circulation Γ are not needed. Only two input files must be created: a file containing the geometrical information of the turbine blade and another file including all the specifications for the hub and wake geometries and grid parameters. The former is meticulously described in Section 4.1.1, while the geometric properties of the hub and wake are explained in Section 4.1.2 and 4.1.3, respectively. Regarding the grid parameters, Table 5.1 shows the quantities to be defined. Eventually, the sub-program *ProPanel* can be run to generate the modelled grid.

Component	Symbol	Description
Blade	N_R	Number of panels along the radial direction
Blade	N_C	Number of panels along the chordwise direction
Blade	α_h	Angle to control the size of the panels close to the hub
Blade	α_t	Angle to control the radial size of the panels close to the tip
Blade	α_{le}	Angle to control the chordwise size of the panels close to the leading edge
Blade	α_{te}	Angle to control the chordwise size of the panels close to the trailing edge
Hub	N_{hu}	Number of upstream hub panels
Hub	N_{hd}	Number of downstream hub panels
Hub	p/D	Pitch distribution on the hub divided by rotor diameter
Wake	J_I	Initial wake strip
Wake	J_F	Final wake strip
Wake	N_W	Number of panels for each wake strip

Table 5.1: Input parameters for grid generation.

Processing

The calculation of the potential flow on the New MEXICO turbine is done by running the program *PROPAN*. Thanks to a configuration file, it is possible to select the type of wake model and, in case of the wake alignment model used in this work, the number of alignment iterations (N_{WA}). Moreover, it is key to choose the right wake radial strips (J_V) and axial (streamwise) positions (X_V) from where the calculations are performed in order to have a smooth wake surface, which ultimately leads to the convergence of the Kutta condition (Equation (3.30)).

Post-processing

The main goal of the post-processing phase is to apply the viscous effects to the potential flow results. This is done by creating an input file containing the experimental lift and drag coefficients of the blade airfoils for different Reynolds numbers. In addition, it is possible to extract pressure data from specific blade sections and obtain a variety of parameters for every blade radial strip, such as angle of attack, normal and tangential force coefficients. The sub-program to be utilised is called *ProPost*.

5.1.2 Numerical test matrix

The numerical tests have been performed to achieve the convergence of the numerical results in steady inflow conditions. The parameters subject to this study are:

1. Wake length,
2. Radial and chordwise number of panels along the blade,
3. Upstream and downstream number of panels on the hub.

The complete test matrix is shown in Table 5.2. The numerical options of the wake alignment model considered for each test are presented in Appendix B. To evaluate the convergence of the results, three

quantities have been analysed:

- The pressure distributions at $25\%, 35\%, 60\%, 82\%$ and 92% radial positions,
- The dimensionless circulation ($\frac{\Gamma}{\Omega R^2}$),
- The viscous power and thrust coefficients C_P and C_T.

Test	**Blade grid ($N_R \times N_C$)**
Wake length equal to [$4R$, $6R$, $8R$, $10R$, $12R$, $14R$].	30×60
Convergence of the grid along the blade radial direction with $N_C = 60$.	[$30, 40, 50, 60, 70, 80$]$\times 60$.
Convergence of the grid along the blade chordwise direction with N_R equal to the best case from the radial test.	$N_{R_{best}} \times$ [$60, 70, 80, 90, 100$]
Convergence of the grid along the hub upstream direction with $N_{hu} = 30$ and $N_{hd} = 45$.	$N_{R_{best}} \times N_{C_{best}}$
Convergence of the grid along the hub upstream direction with $N_{hu} = 35$ and $N_{hd} = 45$.	$N_{R_{best}} \times N_{C_{best}}$
Convergence of the grid along the hub upstream direction with $N_{hu} = 40$ and $N_{hd} = 45$.	$N_{R_{best}} \times N_{C_{best}}$
Convergence of the grid along the hub downstream direction with $N_{hu_{best}}$ and $N_{hd} = 55$.	$N_{R_{best}} \times N_{C_{best}}$
Convergence of the grid along the hub downstream direction with $N_{hu_{best}}$ and $N_{hd} = 65$.	$N_{R_{best}} \times N_{C_{best}}$

Table 5.2: Numerical test matrix.

Eventually, the results obtained with the best grid yielded by this study are compared to the experimental measurements, in order to assess the accuracy of the panel method.

5.1.3 Wake length

The starting point of the numerical tests consists of understanding the influence of the wake length (x_W) on the numerical results, considering $N_R = 30$, $N_C = 60$, $J_I = 6$ and $J_F = 30$.

TSR = 6.7

The pressure distribution along the blade for specific radial positions is presented in Figure 5.1. It can be seen that the wake length has a negligible effect on the pressure distributions. However, a small discrepancy is obtained on the suction side for the region closer to the leading edge. In that region, for all the radial positions but $r/R = 25\%$, the pressures resulted from the wake lengths ($4R, 6R, 8R$) are slightly smaller than the ones yielded by the wake lengths ($10R, 12R, 14R$), meaning that the predicted loads on the blade are greater in the first case.

The same trend can be visualised for the circulation around the blade (in dimensionless form), shown in Figure 5.2. Indeed, it is possible to distinguish clearly two groups in terms of matching values, one comprehending the smaller wake lengths ($4R, 6R, 8R$) and the other composed by greater wake lengths ($10R, 12R, 14R$). The main outcome is that the former predicts a larger circulation around the blade for

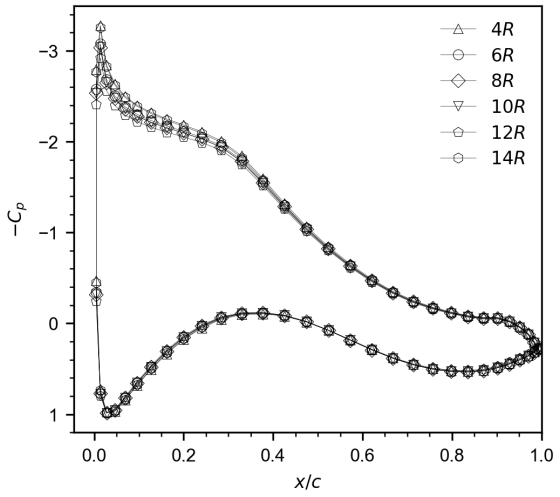

(a) $r/R = 25\%$

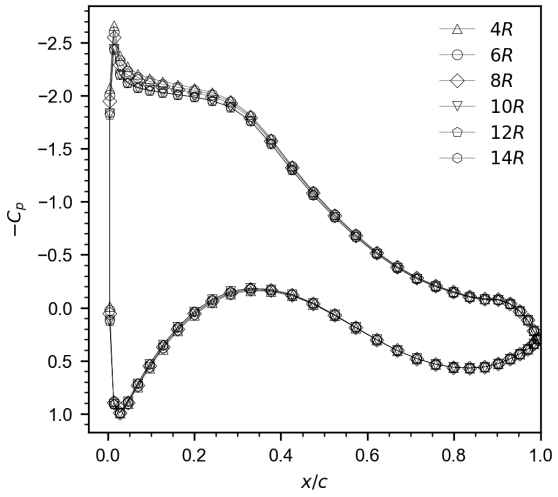

(b) $r/R = 35\%$

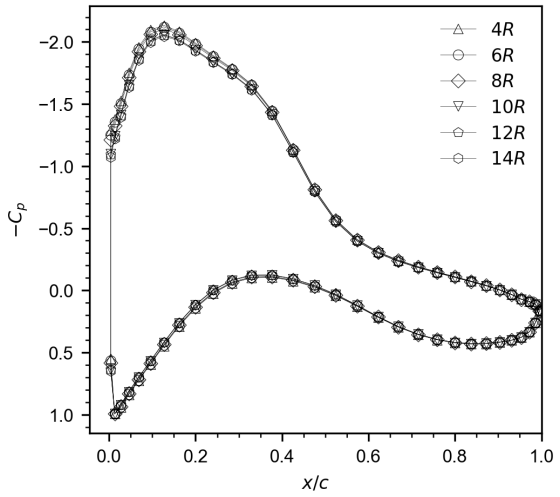

(c) $r/R = 60\%$

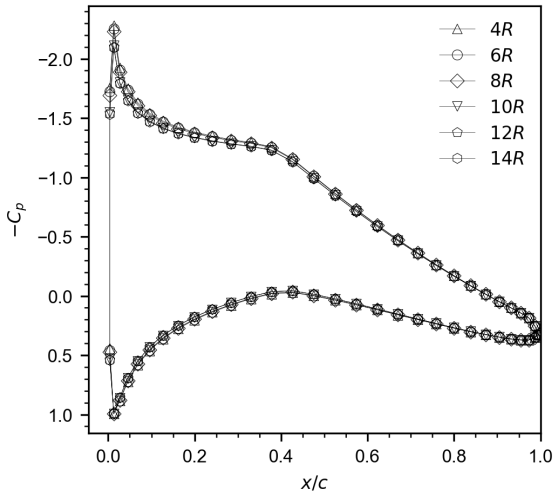

(d) $r/R = 82\%$

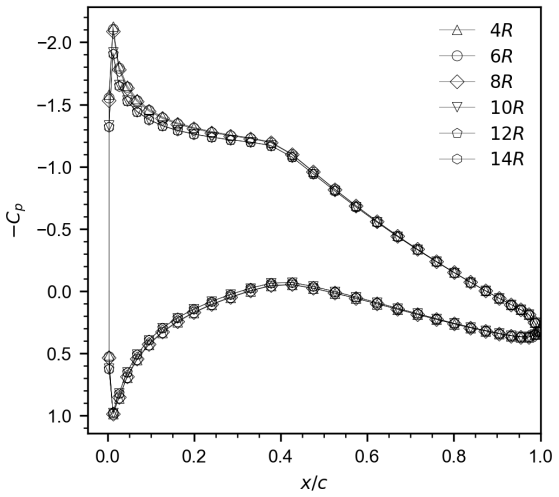

(e) $r/R = 92\%$

Figure 5.1: Numerical pressure coefficient comparison for different wake lengths at $TSR = 6.7$.

almost the entire blade span. Moreover, a small fluctuation can be noticed at the blade mid-span, where the circulation slightly decreases to then increase again, probably due to the geometrical transition between the DU and RISØ airfoils.

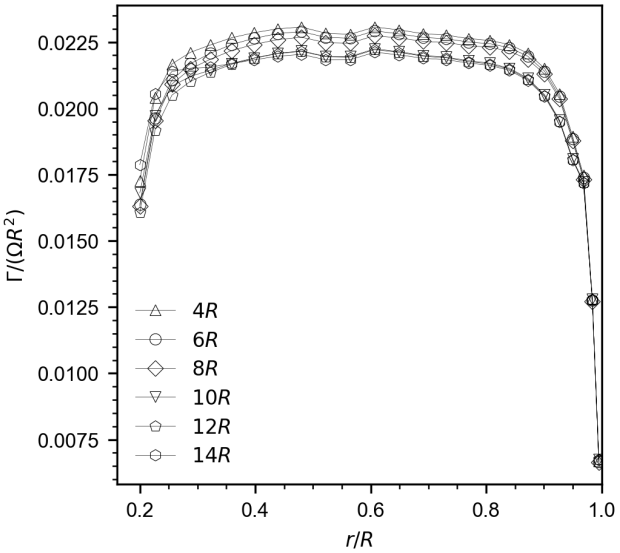

Figure 5.2: Numerical flow circulation comparison for different wake lengths at $TSR = 6.7$.

Finally, Table 5.3 summarises the outcomes for the power and thrust coefficients. ΔC_P and ΔC_T denote the difference between the C_P and C_T between two consecutive wake lengths in the table, respectively. Clearly, only when increasing the wake lengths, the fluctuation of the numerical results

	$\boldsymbol{C_P}$	$\boldsymbol{C_T}$	$\lvert\boldsymbol{\Delta C_P}\rvert$ [%]	$\lvert\boldsymbol{\Delta C_T}\rvert$ [%]
$4R$	0.4892	0.8969	-	-
$6R$	0.4816	0.8900	1.553	0.7693
$8R$	0.4742	0.8837	1.537	0.7079
$10R$	0.4474	0.8621	5.562	2.444
$12R$	0.4458	0.8601	0.3576	0.2320
$14R$	0.4442	0.8605	0.3589	0.04651

Table 5.3: Numerical power and thrust coefficients for different wake lengths at $TSR = 6.7$.

becomes negligible. Furthermore, among the results with $(10R, 12R, 14R)$, the absolute difference is extremely small, therefore all of these wake lengths can be considered valid. The chosen wake length to proceed with the numerical tests is $12R$, since it is the middle value among the possible valid lengths.

TSR = 10

Figure 5.3 shows the pressure distribution for the simulated results at $TSR = 10$. As one can notice, the wake length of $4R$ is missing: the main motivation is that it was not possible to reach the convergence of the Kutta condition for such a short wake. As already proved by the calculations at $TSR = 6.7$, numerical oscillations disappear towards longer wake lengths, thus no further investigations were carried out.

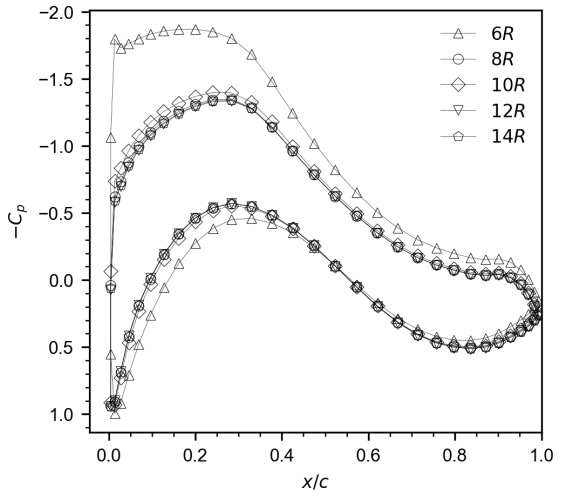

(a) $r/R = 25\%$

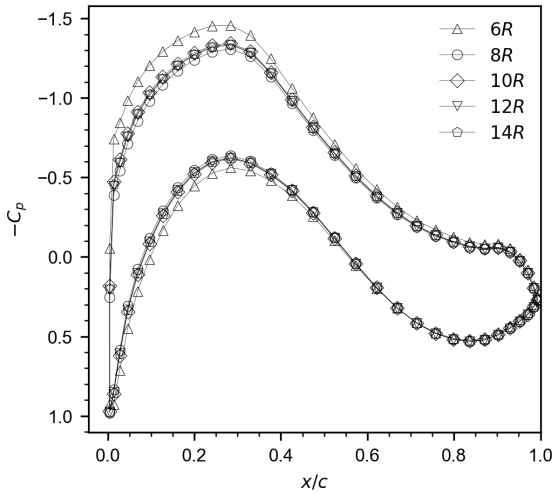

(b) $r/R = 35\%$

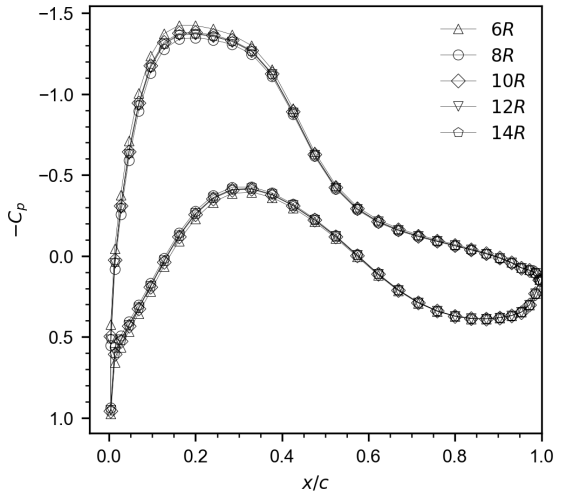

(c) $r/R = 60\%$

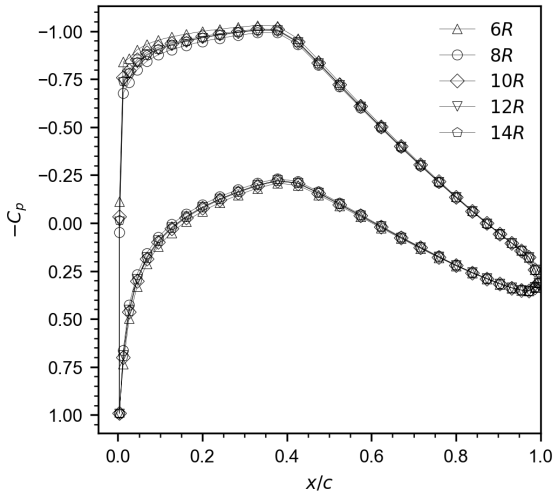

(d) $r/R = 82\%$

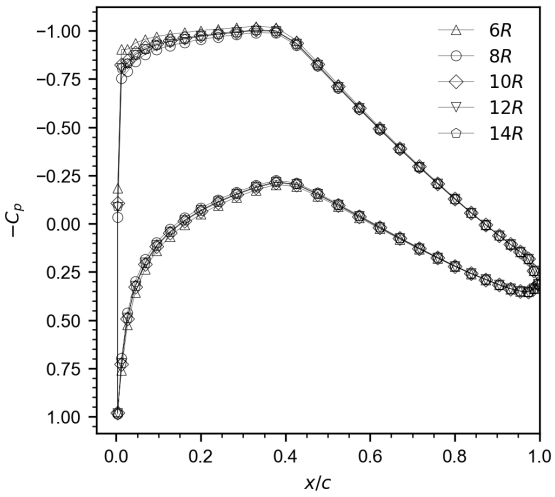

(e) $r/R = 92\%$

Figure 5.3: Numerical pressure coefficient comparison for different wake lengths at $TSR = 10$.

Three main trends can be highlighted:

1. The wake length $6R$ predicts large differences compared to the other results at the radial positions 25% and 35%,

2. The wake length $8R$ forecasts the largest pressure distribution on the suction side of the blade (lowest loads),

3. The wake lengths $(10R, 12R, 14R)$ are almost coincident for each radial position but $r/R = 25\%$.

Figure 5.4 illustrates the circulation around the blade. As expected, the circulation for the case $6R$ is completely different from the other cases, especially at the inner sections of the blade, and the wake length $8R$ predicts a lower circulation for almost the whole blade span. In addition, only $12R$ and $14R$ wakes give almost identical results along the blade, since the wake length $10R$ yields higher values up to about 30% of the blade span.

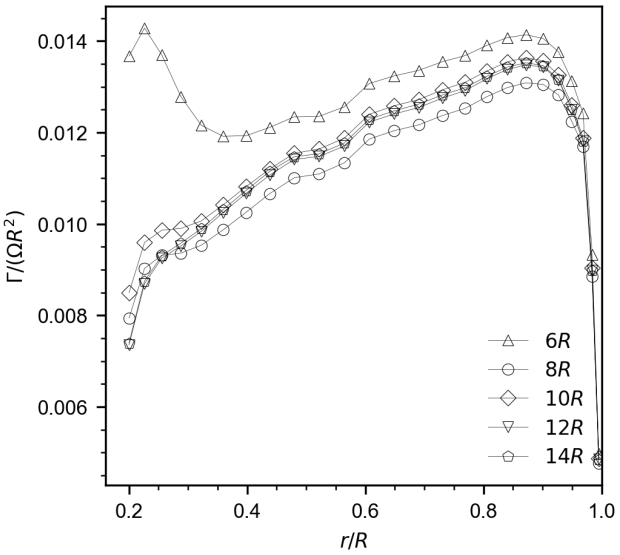

Figure 5.4: Numerical flow circulation comparison for different wake lengths at $TSR = 10$.

The power and thrust coefficient estimations are presented in Table 5.4. There is a clear trend of convergence of the results towards longer wakes, however the magnitude of ΔC_P is three times larger than in the $TSR = 6.7$ scenario. Therefore, further considerations must be evaluated in order to assess the best wake length between $12R$ and $14R$. It is useful to visualise the wake pitch distribution (divided by

	C_P	C_T	$\lvert\Delta C_P\rvert$ [%]	$\lvert\Delta C_T\rvert$ [%]
$6R$	0.4222	1.209	-	-
$8R$	0.2964	1.076	29.80	11.00
$10R$	0.3437	1.123	15.96	4.368
$12R$	0.3278	1.106	4.626	1.513
$14R$	0.3326	1.111	1.464	0.4521

Table 5.4: Steady axial flow power and thrust coefficients for different wake lengths at $TSR = 10$.

the rotor diameter) along the radial direction at some specific axial positions X_V, as presented in Figure 5.5. The wake pitch is defined as $p = 2\pi r \tan\psi$. One can immediately notice that near the rotor the wake geometries have almost the same pitch while some differences occur in the more distant region. However, the overall wake pitch trends are reasonable for both wake lengths, therefore $x_W = 12R$ has been selected for the following numerical studies as the minimum acceptable wake length.

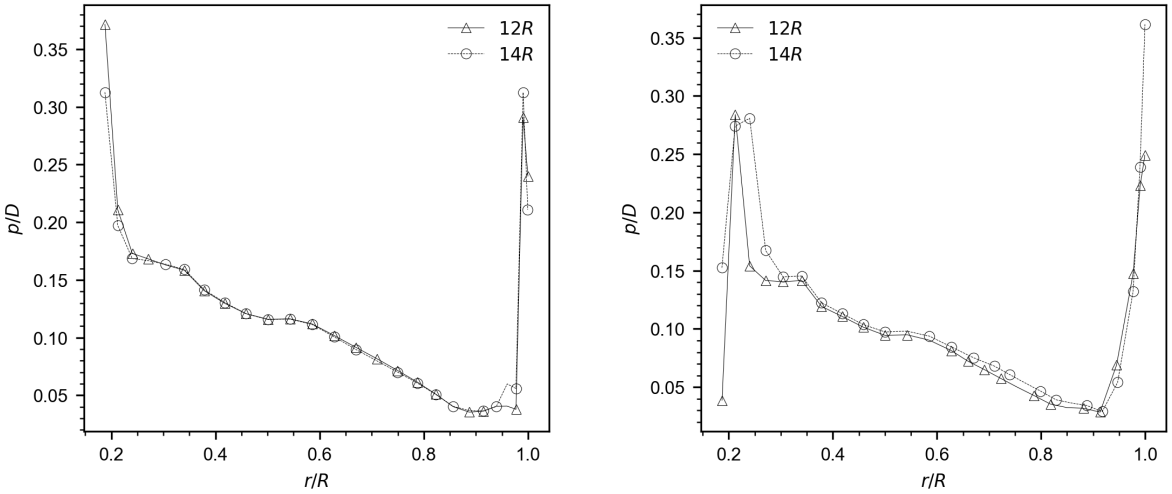

(a) $X_V = 0.5$ (b) $X_V = 2.0$

Figure 5.5: Wake pitch comparison between $12R$ and $14R$ wake lengths at different axial positions for $TSR = 10$.

5.1.4 Blade radial distribution

The numerical tests along the radial direction of the blade are extremely important to find a good compromise between blade panel resolution and computational time to run the simulations. Obviously, the higher is the resolution, the lower is the dimension of the panels and the greater is the running time of the simulations. These tests are based on a blade grid composed by $N_C = 60$ and N_R varying between 30 and 80 with a constant step of 10.

TSR = 6.7

The results of the pressure distribution achieved for the $TSR = 6.7$ case are presented in Figure 5.6. On the whole, no major discrepancy can be found among the different grid resolutions. Focussing on the 50×60 and 60×60 grids, it can be seen that the pressure profiles are slightly smaller in magnitude than the ones of the other configurations on the suction side in the region closer to the leading edge, particularly at the first three radial positions. Similar outcomes can be extracted from the circulation along the blade, Figure 5.7. The 60×60 grid predicts overloading for most of the blade span, presenting a grater difference from the other grid settings in the central zone of the blade. Furthermore, it can be highlighted that the pressure distribution yielded by the 70×60 grid presents lower values for the first half of the blade, trend that is harder to notice in the pressure graphs at $r/R = 25\%$ and $r/R = 35\%$.

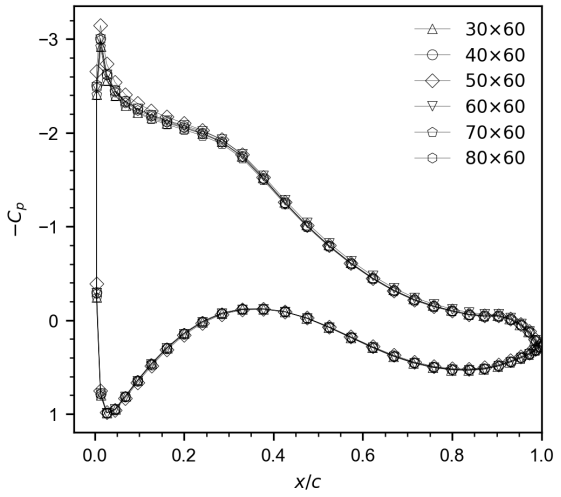

(a) $r/R = 25\%$

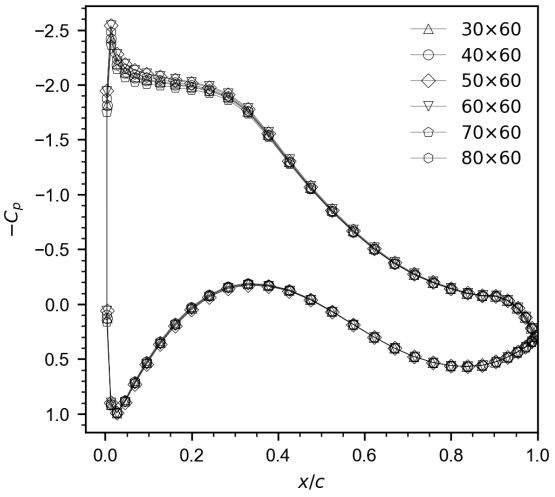

(b) $r/R = 35\%$

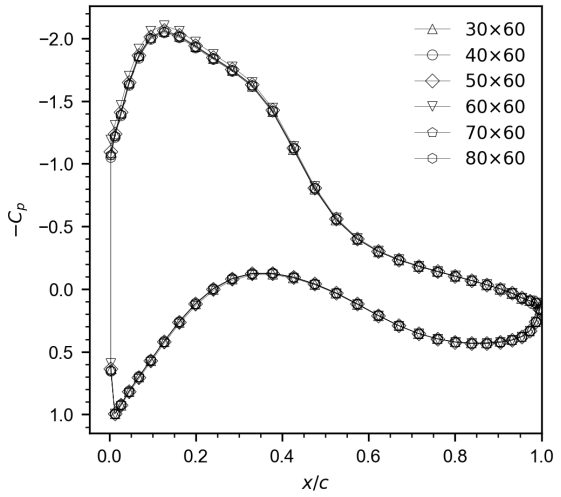

(c) $r/R = 60\%$

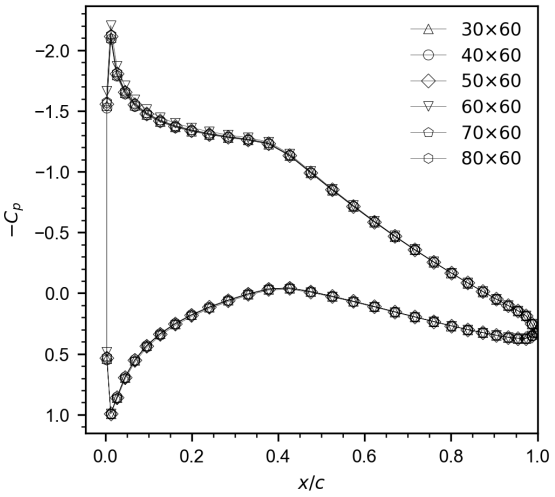

(d) $r/R = 82\%$

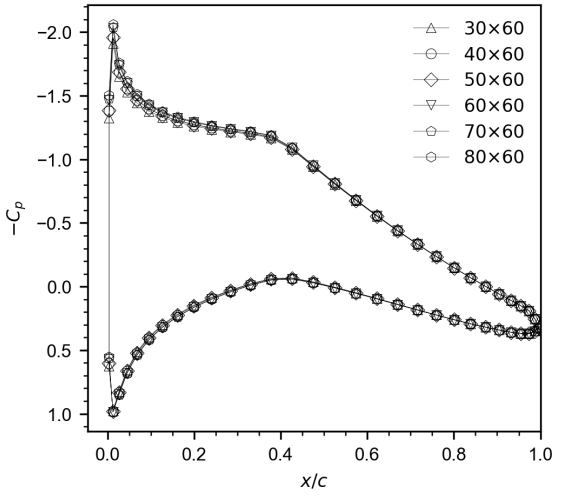

(e) $r/R = 92\%$

Figure 5.6: Numerical pressure coefficient comparison for a different number of blade radial panels at $TSR = 6.7$.

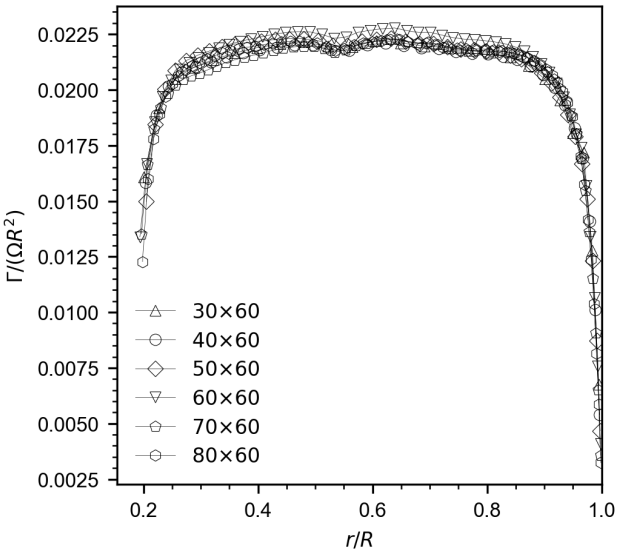

Figure 5.7: Numerical flow circulation comparison for a different number of blade radial panels at $TSR = 6.7$.

In accordance with the above-mentioned analysis, Table 5.5 demonstrates that the power and thrust coefficients for the 50×60 and 60×60 grids are the biggest ones. The convergence of the results appears to be reached only with $N_R = 70$ and $N_R = 80$. In order to select one of them, as it has been

	C_P	C_T	$\lvert\Delta C_P\rvert$ [%]	$\lvert\Delta C_T\rvert$ [%]
30×60	0.4458	0.8601	-	-
40×60	0.4416	0.8549	0.9421	0.6046
50×60	0.4495	0.8605	1.789	0.6551
60×60	0.4658	0.8766	3.626	1.871
70×60	0.4398	0.8571	5.582	2.225
80×60	0.4405	0.8601	0.1592	0.3500

Table 5.5: Numerical power and thrust coefficients for a different number of blade radial panels at $TSR = 6.7$.

done for the wake length test at $TSR = 10$, the pitch distributions of the two wake geometries at multiple axial positions have been compared, Figure 5.8. Evidently, the wake pitch for the $N_R = 70$ grid has a very large magnitude in the region closer to the hub. This tendency is more marked when analysing wake sections further downstream, where a peak p/D of about $10\ °/m$ is reached. On the other hand, this behaviour is not seen for wake geometry of the $N_R = 80$ case, with the wake pitch being almost constant for each axial position. Moreover, the pitch distribution is smooth and does not present any irregularity nor peaks. As a consequence, $N_R = 80$ is chosen for continuing the numerical tests.

It is important to stress that the results obtained from this test obviously depend on the blade grid refinement, but also on the different numerical options utilised for each case (Appendix B.2).

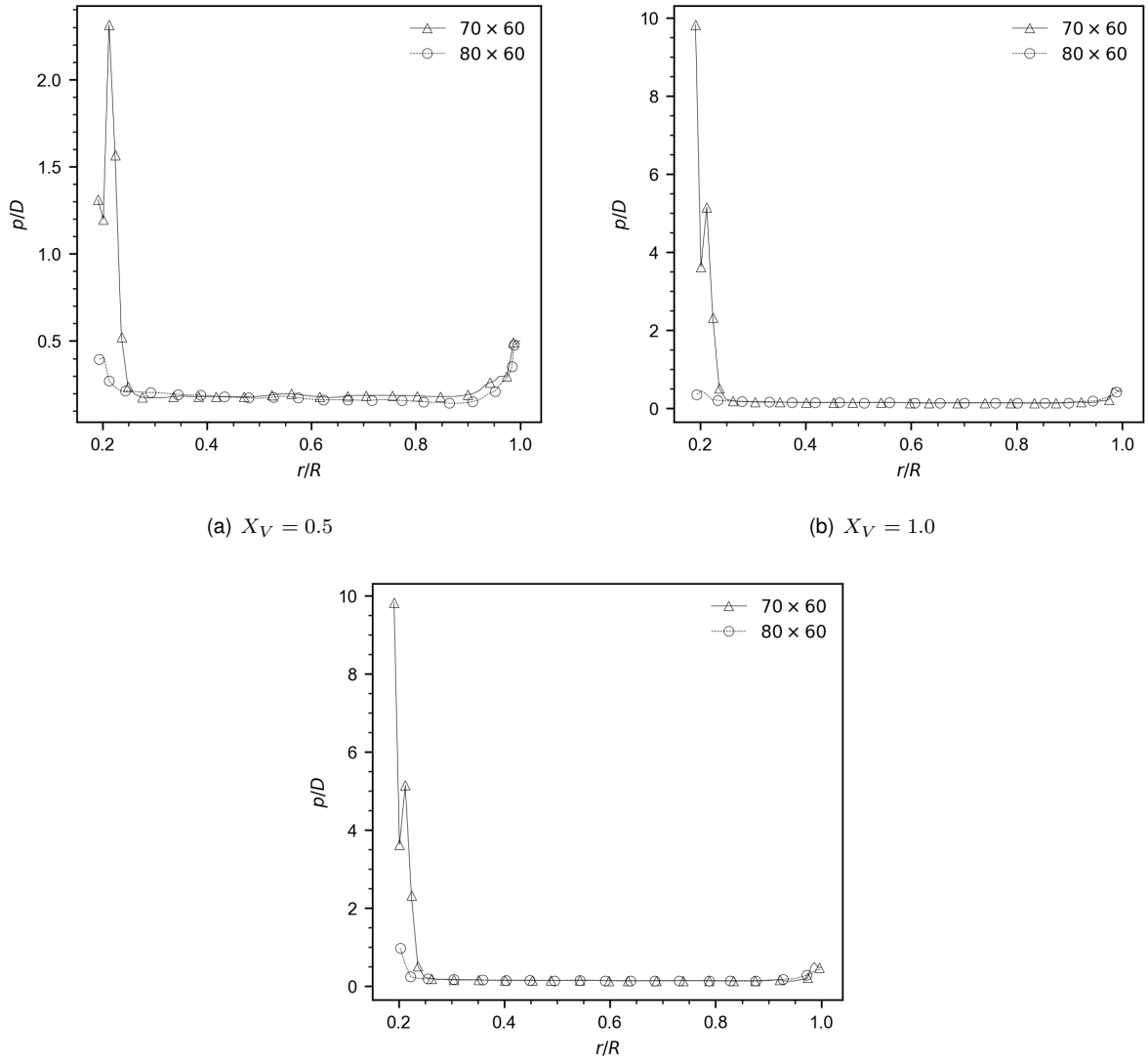

(a) $X_V = 0.5$

(b) $X_V = 1.0$

(c) $X_V = 2.0$

Figure 5.8: Wake pitch comparison between $N_R = 70$ and $N_R = 80$ grids at different axial positions for $TSR = 6.7$.

TSR = 10

The pressure trends obtained with the $TSR = 10$ are consistently different from the one for the $TSR = 6.7$, as shown in Figure 5.9. At $r/R = 25\%$ and $r/R = 35\%$ there is a clear distinction among all the cases, with the greatest and smallest pressure values on the suction side outputted by $N_R = 70$ and $N_R = 40$, respectively. On the other hand, the pressure distributions are extremely akin to each other for the remaining radial positions, however one might realise that the 70×60 grid is coincident with the 80×60 grid, behaving in a different way from the other resolutions. This is even more evident when analysing the flow circulation, Figure 5.10. Beside the fluctuations being common to all the grid settings, the predicted circulation is slightly higher for the group composed by $N_R = [30, 40, 50, 60]$ than for $N_R = [70, 80]$.

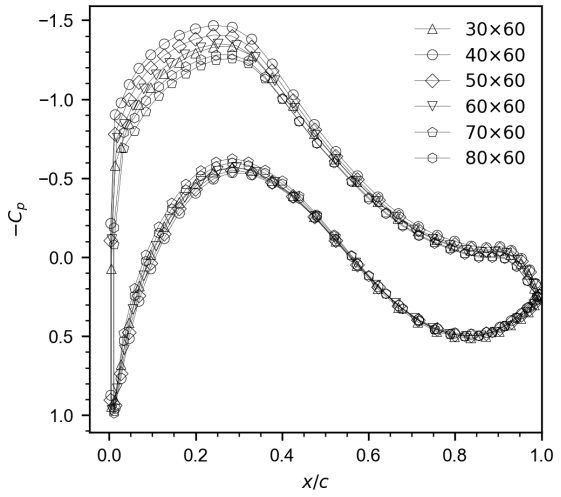

(a) $r/R = 25\%$

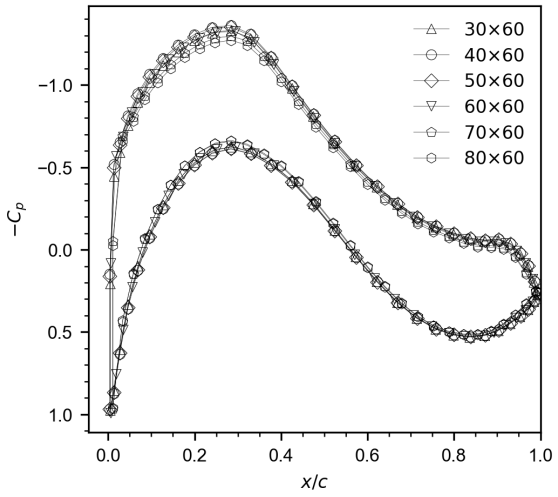

(b) $r/R = 35\%$

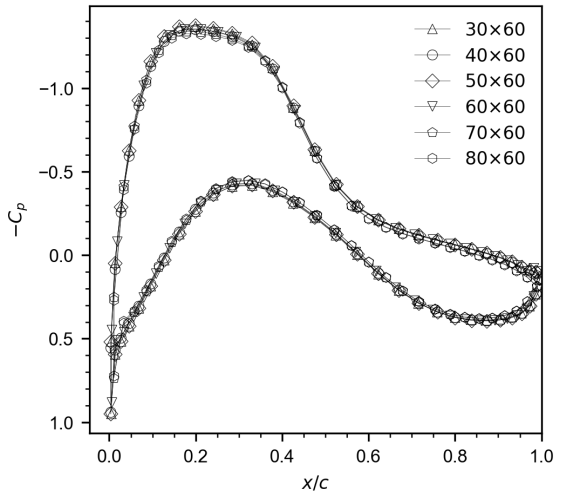

(c) $r/R = 60\%$

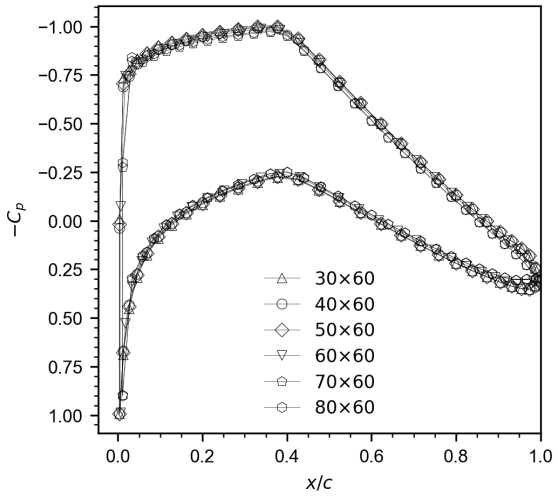

(d) $r/R = 82\%$

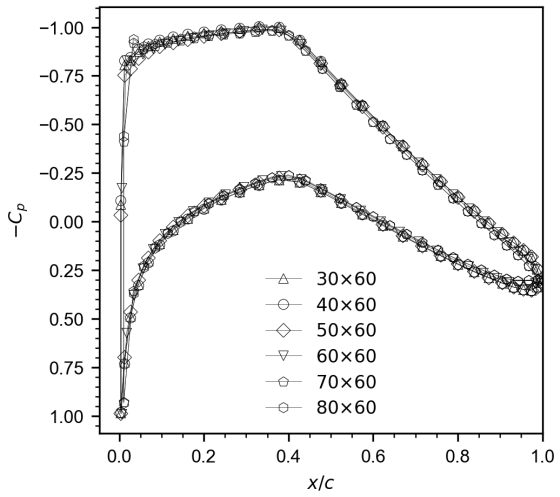

(e) $r/R = 92\%$

Figure 5.9: Numerical pressure coefficient comparison for a different number of blade radial panels at $TSR = 10$.

In terms of C_P and C_T, the convergence of the results is again achieved for the 70×60 and 80×60 grids, with $\Delta C_T = 0$. The latter has been utilised for the following tests in order to be consistent with grid obtained from the $TSR = 6.7$ tests.

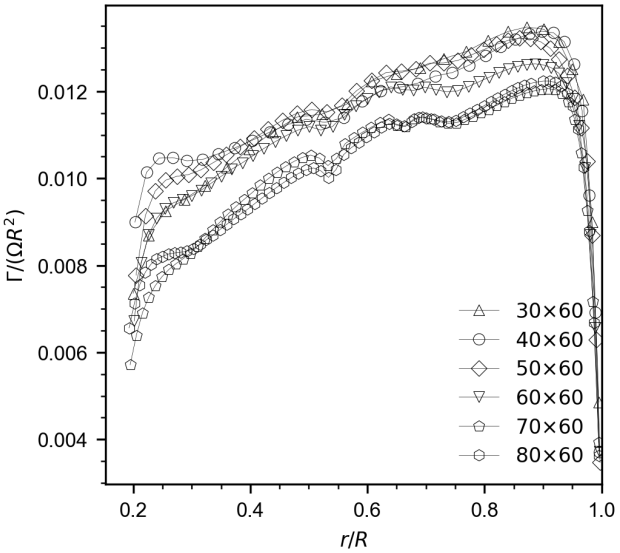

Figure 5.10: Numerical flow circulation comparison for a different number of blade radial panels at $TSR = 10$.

	C_P	C_T	$\lvert\Delta C_P\rvert$ [%]	$\lvert\Delta C_T\rvert$ [%]
30×60	0.3278	1.106	-	-
40×60	0.3152	1.096	3.844	0.9042
50×60	0.3154	1.097	0.06345	0.09124
60×60	0.2984	1.054	5.390	3.920
70×60	0.3123	1.002	4.658	4.934
80×60	0.3143	1.002	0.6404	0

Table 5.6: Numerical power and thrust coefficients for a different number of blade radial panels at $TSR = 10$.

5.1.5 Blade chordwise distribution

The second test performed on the blade grid is the one evaluating the optimal number of panels along the chordwise direction. With the radial panels being equal to 80, N_C is set between 60 and 100 with a step of 10. The number of the chordwise panels must be assessed in a way such that the grid is properly refined without creating very small panels which might affect the convergence of the results.

TSR = 6.7

From the analysis of the pressure profiles the main outcome is that the grid with $N_C = 70$ forecasts a lower pressure on the suction side of the blade for the radial positions 25% and 35%. Once again, it is

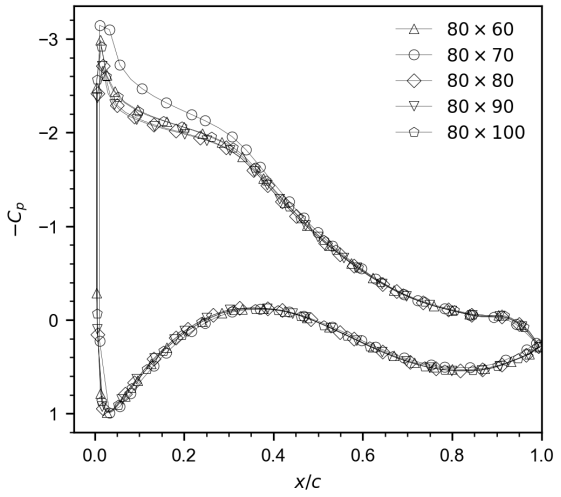

(a) $r/R = 25\%$

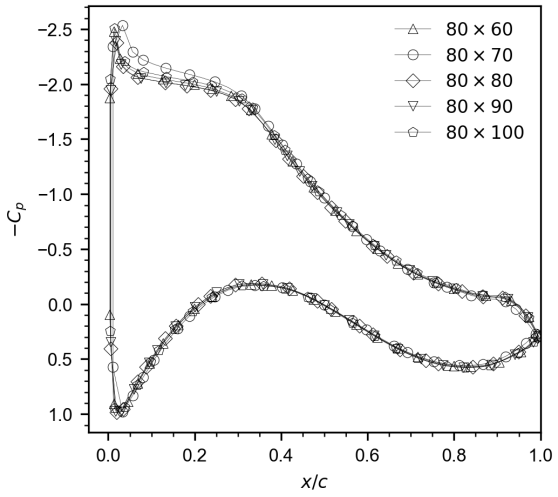

(b) $r/R = 35\%$

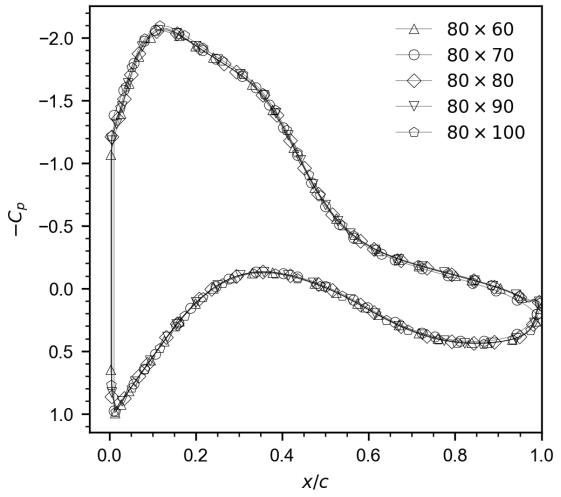

(c) $r/R = 60\%$

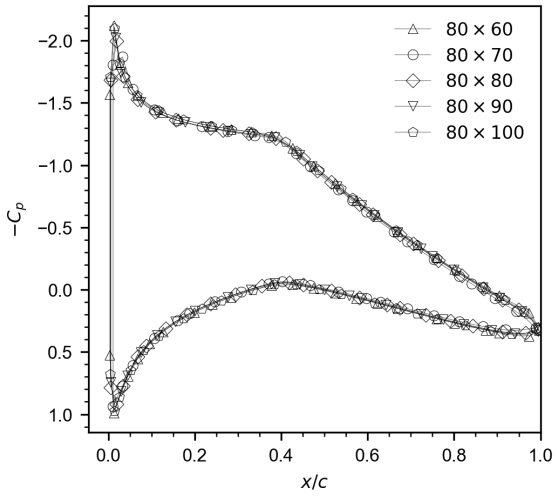

(d) $r/R = 82\%$

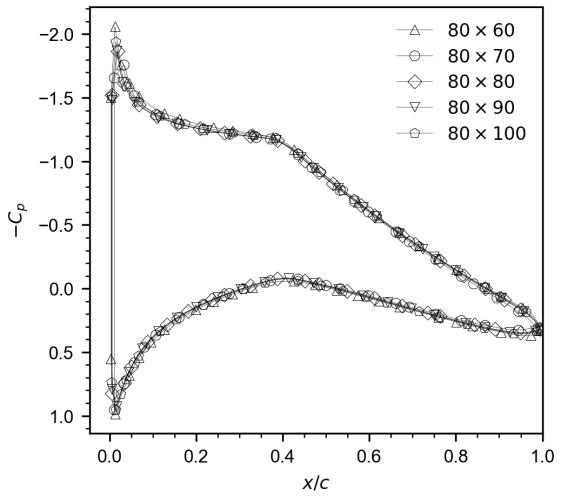

(e) $r/R = 92\%$

Figure 5.11: Numerical pressure coefficient comparison for a different number of blade chordwise panels at $TSR = 6.7$.

fundamental to understand that these differences may also be related with the obtained wake geometries near the root. Regarding the other configurations, all of them match smoothly, presenting only little differences on the suction peak at the leading edge. Accordingly with the pressure distribution, the circulation of the $N_C = 70$ case presents higher values in the section closer to the blade root, to then invert the trend near the tip (Figure 5.12). It is also worth noticing that the most refined grid (80×100) gives the largest flow circulation at the middle sections of the blade. These aspects are well reflected in

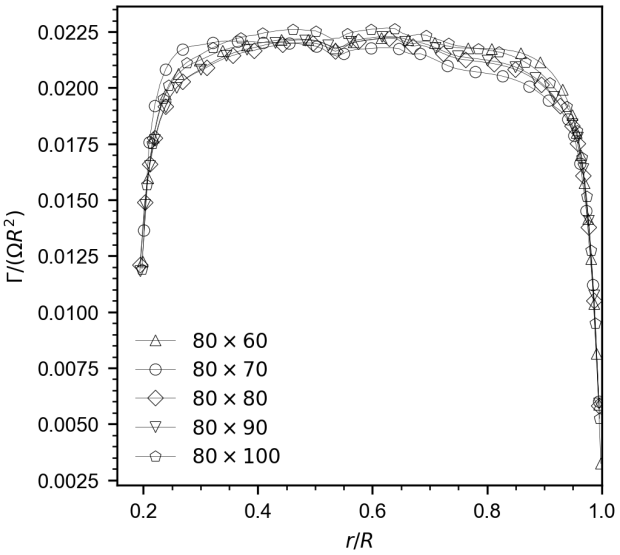

Figure 5.12: Numerical flow circulation comparison for a different number of blade chordwise panels at $TSR = 6.7$.

the power and thrust coefficient estimates (Table 5.7). Indeed the largest C_P occur for $N_C = [70, 100]$, while the greatest C_T is predicted with $N_C = 100$. Evidently, the increase of the number of panels do not

	$\boldsymbol{C_P}$	$\boldsymbol{C_T}$	$\lvert\boldsymbol{\Delta C_P}\rvert$ [%]	$\lvert\boldsymbol{\Delta C_T}\rvert$ [%]
80×60	0.4405	0.8601	-	-
80×70	0.4556	0.8469	3.428	1.535
80×80	0.4397	0.8458	3.490	0.1299
80×90	0.4411	0.8493	0.3184	0.4138
80×100	0.4565	0.8653	3.491	1.884

Table 5.7: Numerical power and thrust coefficients for a different number of blade chordwise panels at $TSR = 6.7$.

lead to numerical convergence. As mentioned previously, a higher N_C causes the panels to be smaller to an extent when the hyperboloidal shape is reduced to a line, creating issues in the calculations. The chosen grid refinement is $N_C = 80$, being the minimum acceptable number of blade chordwise panels.

TSR = 10

Figure 5.13 shows the pressure distribution for the $TSR = 10$. Interestingly, overloading is predicted at the first two radial positions by the most refined grids, 80×90 and 80×100.

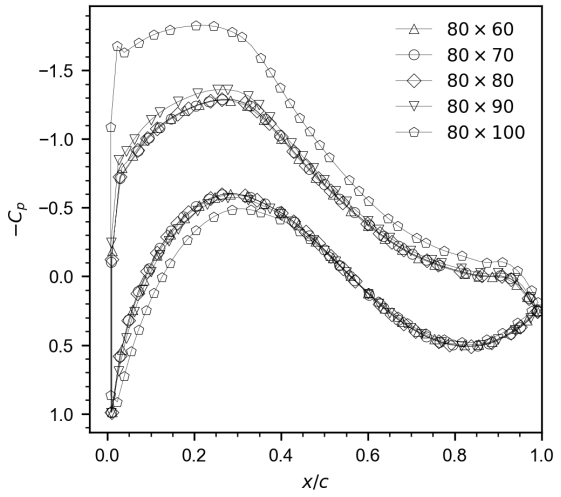

(a) $r/R = 25\%$

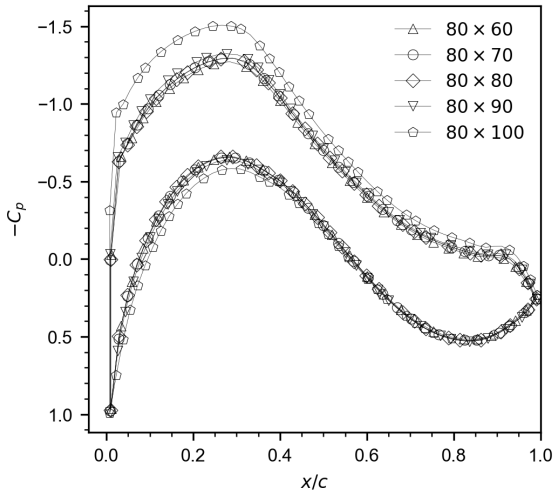

(b) $r/R = 35\%$

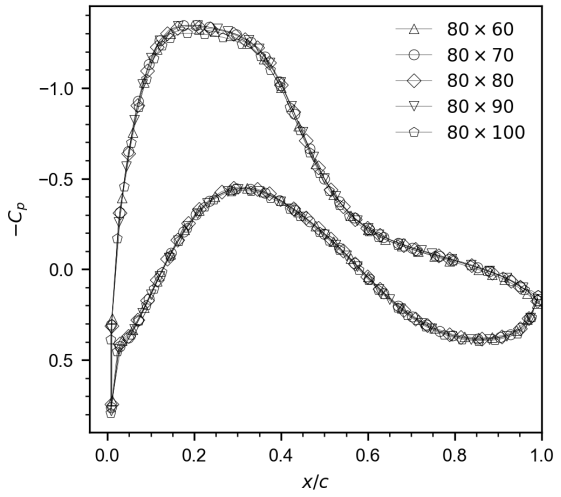

(c) $r/R = 60\%$

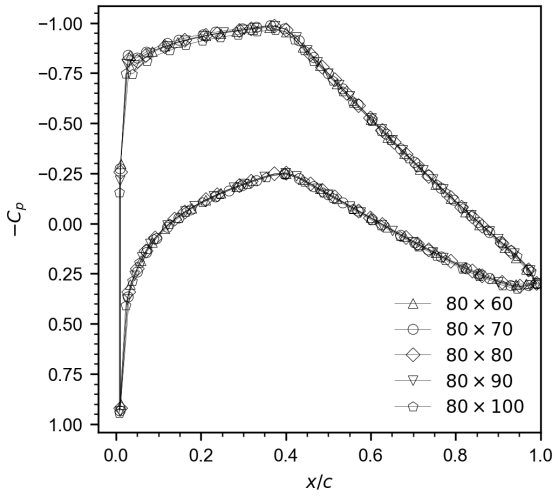

(d) $r/R = 82\%$

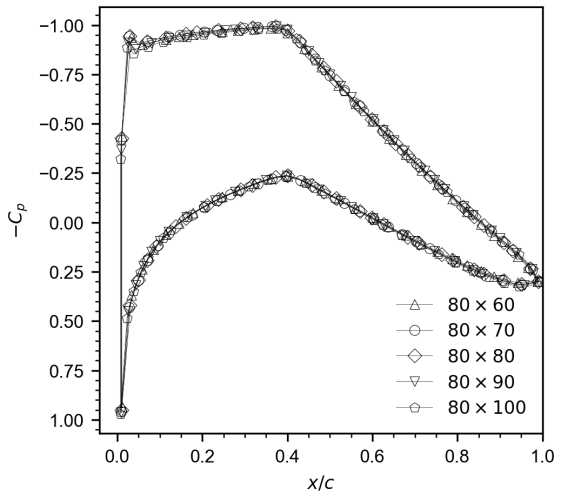

(e) $r/R = 92\%$

Figure 5.13: Numerical pressure coefficient comparison for a different number of blade chordwise panels at $TSR = 10$.

At $r/R = [60\%, 82\%, 92\%]$, all grid settings yield approximately the same results, with $N_C = 100$ having slightly larger pressure values on the suction side of the blade. The additional insight that can be grasped from the flow circulation illustrated in Figure 5.14 is that the 80×60 grid forecasts under-loading on about 70% of the blade compared to the other grid resolutions. As for the $TSR = 6.7$, the grid with

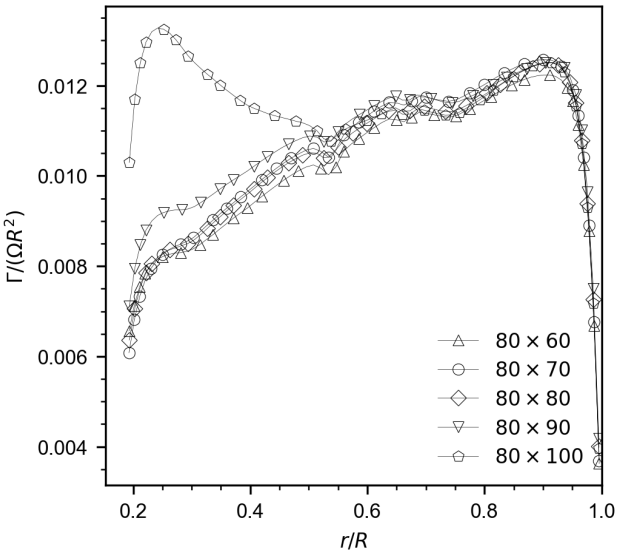

Figure 5.14: Numerical flow circulation comparison for a different number of blade chordwise panels at $TSR = 10$.

$N_C = 100$ outputs the most divergent values both for C_P and C_T, therefore it is not considered for the selection of the final N_C. Bearing in mind the results obtained for $TSR = 6.7$, $N_C = 80$ is deemed

	C_P	C_T	$\lvert\Delta C_P\rvert$ [%]	$\lvert\Delta C_T\rvert$ [%]
80×60	0.3143	1.002	-	-
80×70	0.3209	1.029	2.100	2.695
80×80	0.3119	1.019	2.805	0.9718
80×90	0.3166	1.041	1.507	2.159
80×100	0.3316	1.070	4.738	2.786

Table 5.8: Numerical power and thrust coefficients for a different number of blade chordwise panels at $TSR = 10$.

to be a valid option, whereas it is worth double checking the wake geometry to capture any possible irregularity. As can be seen in Figure 5.15, $N_C = 90$ presents a wake pitch smoother than $N_C = 80$ both at $X_V = 0.5$ and $X_V = 2.0$. Indeed, even though the overall wake pitch trends are similar, an unexpected large kink is seen at $r/R = 85\%$ for $N_C = 80$. Moreover, the C_P and C_T of these two cases are extremely comparable, therefore the 80×90 grid is chosen to proceed with the tests.

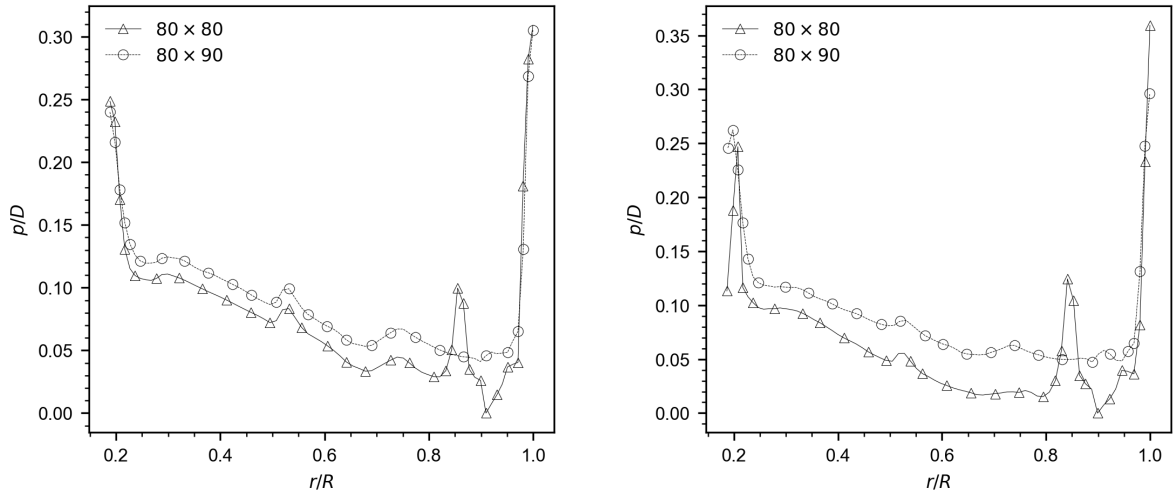

(a) $X_V = 0.5$ (b) $X_V = 2.0$

Figure 5.15: Wake pitch comparison between $N_C = 80$ and $N_C = 90$ grids at different axial positions for $TSR = 10$.

5.1.6 Hub upstream and downstream distribution

The last batch of numerical tests evaluates how and if the pressure, circulation and forces along the blades are affected by the grid refinement level on the hub. Three configurations have been analysed both in the upstream and downstream directions, $N_{hu} = [30, 35, 40]$ and $N_{hd} = [45, 55, 65]$.

Upstream

Figure 5.16 shows the pressure profiles for the radial position 25% at both TSRs. As one might expect,

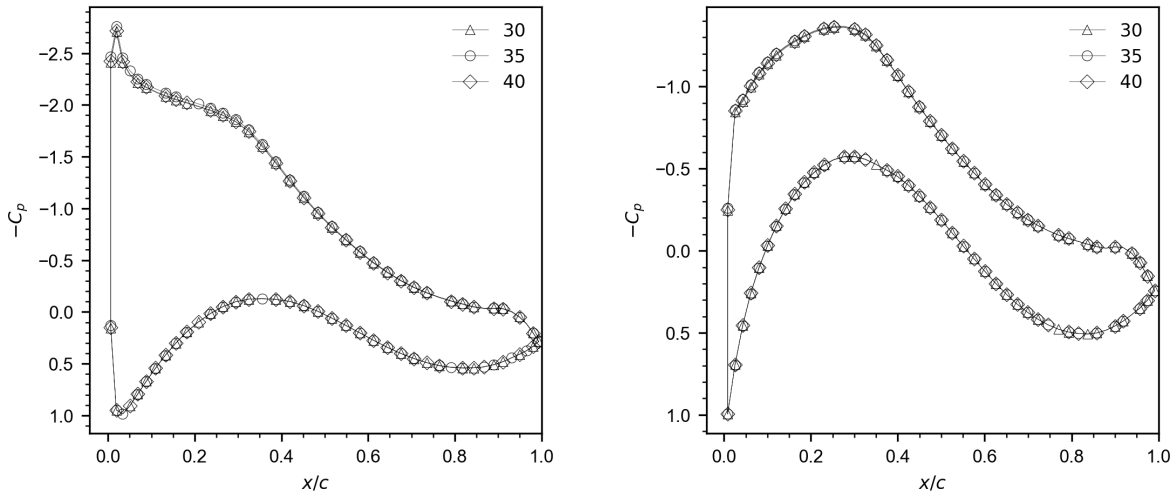

(a) $TSR = 6.7$ (b) $TSR = 10$

Figure 5.16: Numerical pressure coefficient comparison for a different number of hub upstream panels at $TSR = 6.7$ and $TSR = 10$ for $r/R = 25\%$.

the influence of the hub grid on the pressure distribution along the blade is negligible. The trends for the remaining radial positions at both TSRs are not presented because all hub grid configurations yield the same exact outcomes. The same comments can be made from the comparison of the flow circulation around the blades, as clearly visible in Figure 5.17. Eventually, Table 5.9 presents the power and thrust

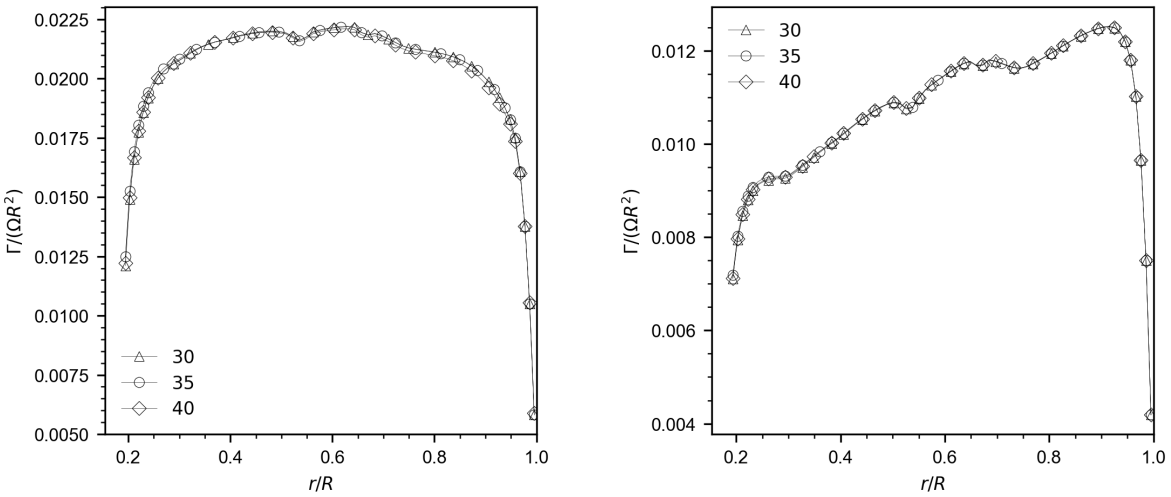

(a) $TSR = 6.7$ (b) $TSR = 10$

Figure 5.17: Numerical flow circulation comparison for a different number of hub upstream panels at $TSR = 6.7$ and $TSR = 10$.

coefficients on the blades. Again all values are massively consistent to each other, therefore the most simple grid ($N_{hu} = 30$) is selected.

	$TSR = 6.7$				$TSR = 10$			
N_{hu}	C_P	C_T	$\lvert\Delta C_P\rvert$ [%]	$\lvert\Delta C_T\rvert$ [%]	C_P	C_T	$\lvert\Delta C_P\rvert$ [%]	$\lvert\Delta C_T\rvert$ [%]
30	0.4397	0.8458	-	-	0.3166	1.041	-	-
35	0.4394	0.8458	0.06823	0	0.3178	1.043	0.3790	0.1921
40	0.4339	0.8412	1.252	0.5439	0.3149	1.038	0.9125	0.4794

Table 5.9: Numerical power and thrust coefficients for a different number of hub upstream panels at $TSR = 6.7$ and $TSR = 10$.

Downstream

Regarding the hub downstream tests, the pressure distributions at the radial positions $[25\%, 35\%, 60\%, 82\%, 92\%]$ are not varying remarkably with N_{hd}. On the other hand, when analysing the circulation along the whole blade span, one can notice that at $TSR = 6.7$ the grid with $N_{hd} = 65$ predicts overloading on the central part of the blade, most likely due to the different numerical options for the wake alignment, while no difference can be seen at at $TSR = 10$. As a consequence, higher power and thrust coefficient are calculated for $N_{hd} = 65$ (Table 5.10). On the whole, no relevant difference is seen among the grids, therefore the simplest grid ($N_{hd} = 45$) is selected as the last piece to form the final optimal grid.

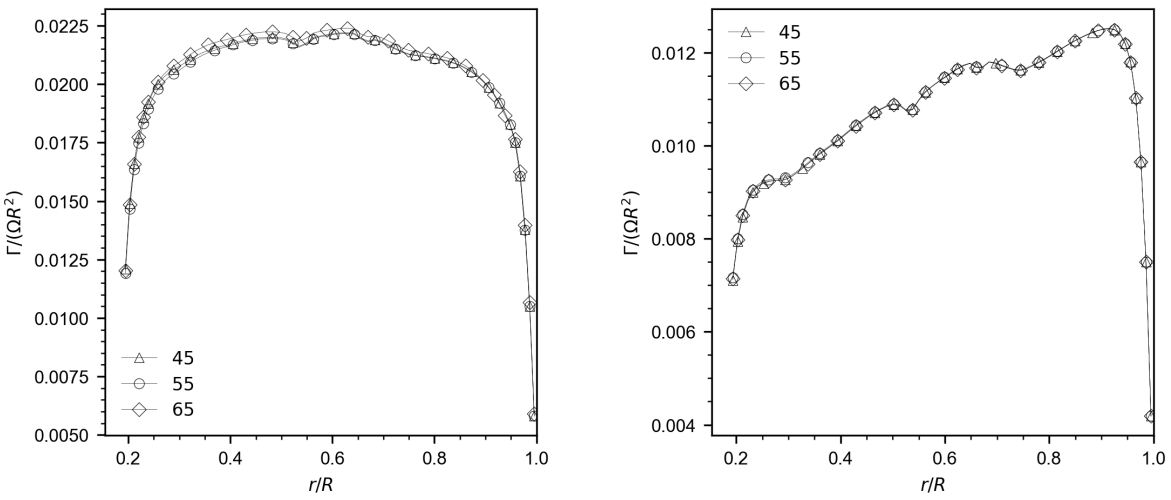

(a) $TSR = 6.7$

(b) $TSR = 10$

Figure 5.18: Numerical flow circulation comparison for a different number of hub downstream panels at $TSR = 6.7$ and $TSR = 10$.

	$TSR = 6.7$				$TSR = 10$			
N_{hu}	C_P	C_T	$\lvert\Delta C_P\rvert$ [%]	$\lvert\Delta C_T\rvert$ [%]	C_P	C_T	$\lvert\Delta C_P\rvert$ [%]	$\lvert\Delta C_T\rvert$ [%]
45	0.4397	0.8458	-	-	0.3166	1.041	-	-
55	0.4379	0.8437	0.4094	0.2483	0.3173	1.042	0.2211	0.09606
65	0.4463	0.8518	1.918	0.9601	0.3188	1.044	0.4727	0.1919

Table 5.10: Numerical power and thrust coefficients for a different number of hub downstream panels at $TSR = 6.7$ and $TSR = 10$.

5.1.7 Comparison with experimental data

The ultimate aim of the numerical tests is to evaluate the accuracy of the results obtained with the numerical optimal turbine grid when compared with the actual experimental data. In case of great precision between simulated and experimental outcomes, two major achievements could be reached:

1. *PROPAN* would be confirmed as an effective tool for wind turbine load predictions in steady flow conditions,

2. The numerical optimal grid would be a valid starting point for the dynamic inflow study.

For clarity purposes, the parameters composing the optimal grid and the selected numerical options are summarised in Table 5.11.

Pressure distribution

The calculated (*Sim*) and measured (*Exp*) pressure profiles at $TSR = 6.7$ and $TSR = 10$ are presented in Figure 5.19 and Figure 5.20, respectively. Clearly, the simulated pressure distribution matches outstandingly the experimental measurements at $r/R = 82\%$ and $r/R = 92\%$. Indeed, the only visible discrepancies are a greater suction peak pressure at the leading edge (at $TSR = 6.7$) and a slight un-

	$\boldsymbol{x_W}$	$\boldsymbol{N_R}$	$\boldsymbol{N_C}$	$\boldsymbol{N_{hu}}$	$\boldsymbol{N_{hd}}$	J_I	J_F	J_V	X_V	N_{WA}
$TSR = 6.7$	12R	80	80	30	45	12	80	[2,3,5,7,11,14,17, 19,21,24,27,29, 31,34,37,39,41, 44,47,49,51,54 57,59,62,64,66, 68,69]	[0.05,0.1, 0.5, 1.0, 2.0]	3
$TSR = 10$	12R	80	90	30	45	9	80	[2,3,5,7,9,11,14,17, 19,21,24,27,29 31,34,37,39,41, 44,47,49,52,55 57,59,61,63,64, 67,69,71,72]	[0.02,0.05, 0.1, 0.5 1.0,2.0]	2

Table 5.11: Numerical optimal grid parameters at $TSR = 6.7$ and $TSR = 10$.

derestimation along the pressure side of the blade sections (at $TSR = 10$). On the other hand, the same precision is not found for the remaining radial positions.

The largest mismatch can be seen for the pressure profiles at $r/R = 25\%$. For both TSRs the predicted pressure is smaller on the suction and pressure sides along the central region of the blade section. The same trends in a less marked way occur at $r/R = 35\%$, even though the pressure estimates are more consistent with the experiments, especially at $TSR = 6.7$. One possible reason is that the blade wake is truncated and does not connect with the hub surface. Therefore, in the cylindrical part, no vorticity is shed from the trailing edge. Furthermore, as briefly mentioned in Section 1.2.1, it is well known that in the blade region closer to the root the 3D effects, such as rotational augmentation (stall delay), have a non-negligible impact on load estimation and are very hard to model. However, the flow conditions (at both TSRs) do not lead to stall delay effects, since the angle of attack is well below the stall conditions. Overall, it is worth noting that for $r/R = 25\%$ and $r/R = 35\%$ the experimental data do not have reasonable values for some chordwise locations, especially where the pressure coefficient is greater than 1, meaning that some sensors recorded wrong measurements (e.g at $x/c = 0.8$). Finally, the pressure distributions obtained with *PROPAN* are qualitatively coherent with the ones outputted by the CFD codes participating in the New MEXICO project. Indeed, as concluded in the final New MEXICO report, Boorsma et al. [33], the experimental resolution of the pressure sensors is insufficient, especially at the lower inflow speeds, resulting in non-smooth measured pressure plots.

Regarding $r/R = 60\%$, there is a clear offset between measured and predicted suction side pressure levels between $x/c = 0.1$ and $x/c = 0.45$ for all TSRs, which is also yielded by the New MEXICO CFD codes. One possible cause might rely on the different camber of the RISØ profile in comparison to the DU and NACA profiles, which leads to the circulation discontinuity at the transition between the profiles (phenomenon called *decambering*). On the other hand, the non-rotating MEXICO blade measurements in the Delft Low speed low turbulence tunnel, hence featuring a totally different spanwise circulation distribution, gave rise to exactly the same observation as the rotating measurements in the DNW.

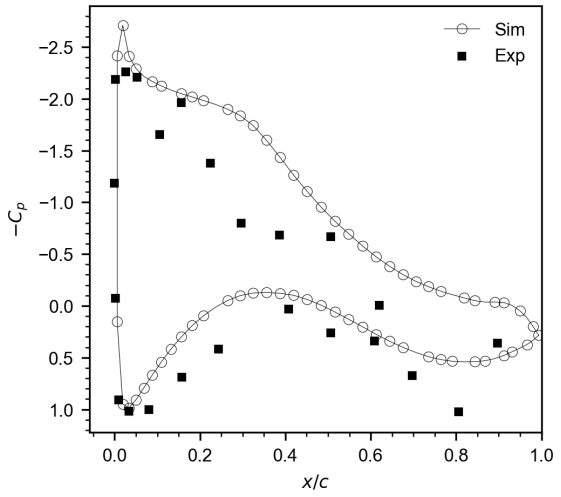

(a) $r/R = 25\%$

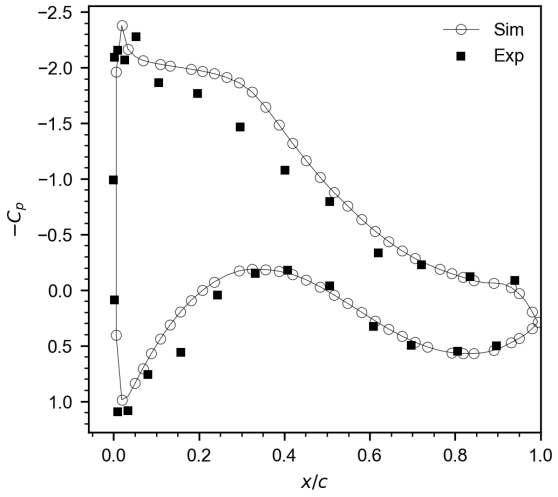

(b) $r/R = 35\%$

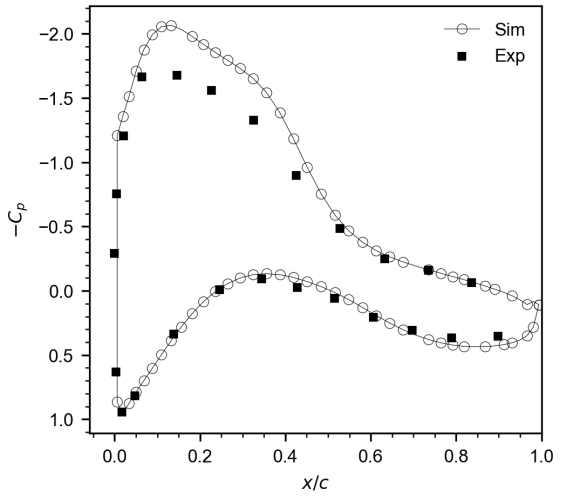

(c) $r/R = 60\%$

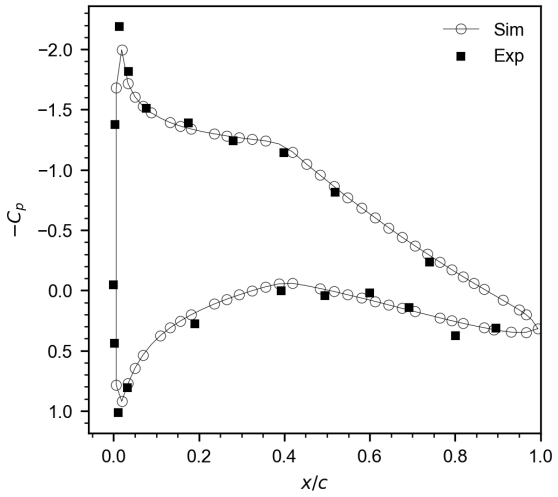

(d) $r/R = 82\%$

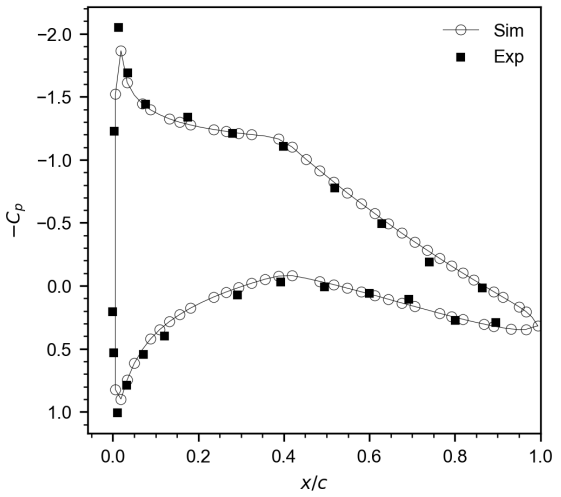

(e) $r/R = 92\%$

Figure 5.19: Numerical pressure coefficient comparison with experimental results at $TSR = 6.7$.

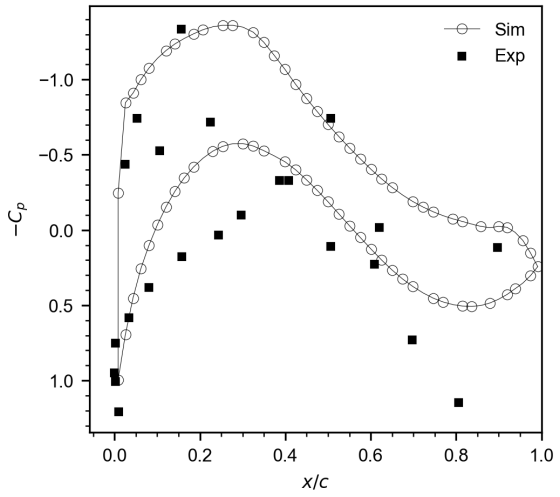

(a) $r/R = 25\%$

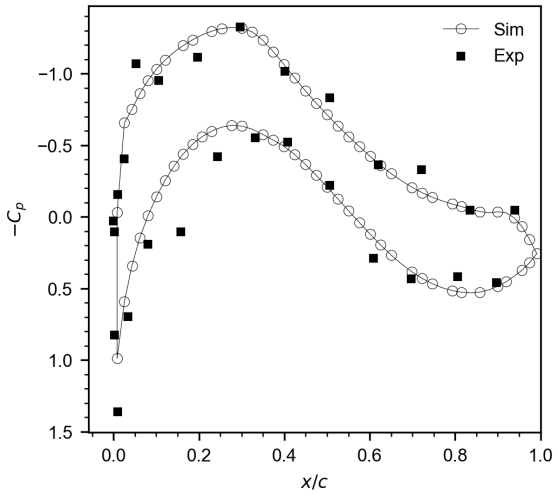

(b) $r/R = 35\%$

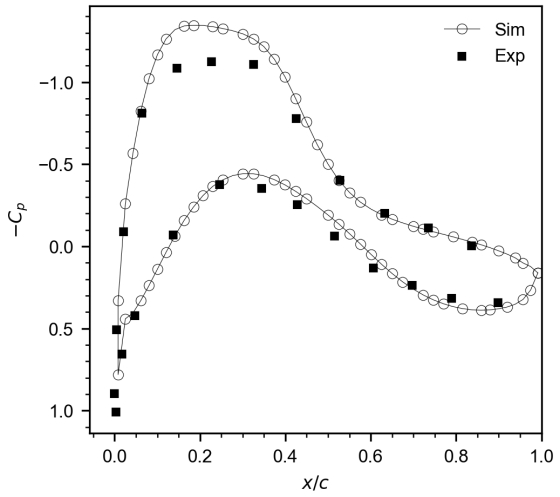

(c) $r/R = 60\%$

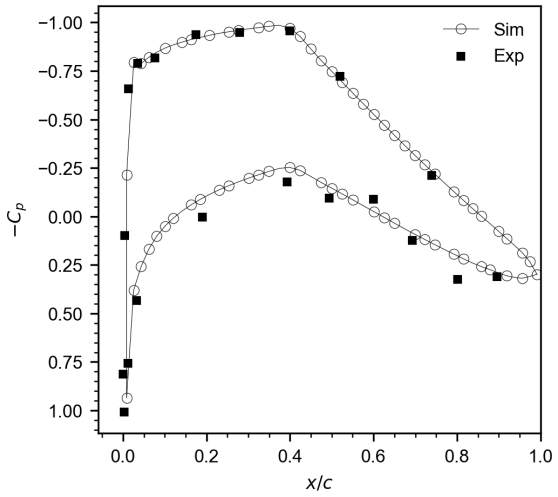

(d) $r/R = 82\%$

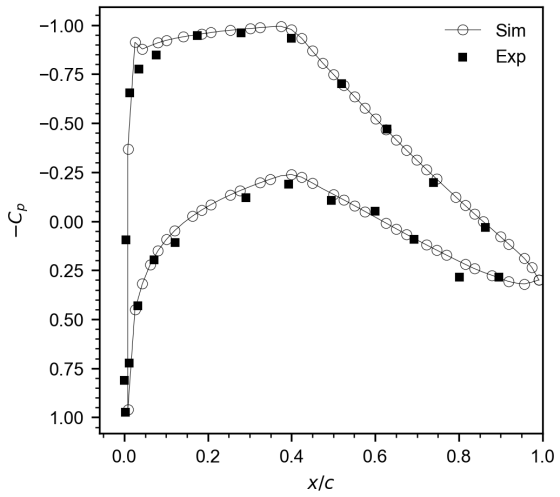

(e) $r/R = 92\%$

Figure 5.20: Numerical pressure coefficient comparison with experimental results at $TSR = 10$.

Eventually, the most probable cause might be found in the roughness strip applied onto the blade, which could enhance the decambering boundary layer, although further studies are needed, as recommended by Boorsma et al. [33].

Power and thrust

Table 5.12 shows the comparison of the power and thrust coefficients between the simulated results and the experimental data. The former include viscous effects while the latter is calculated by integrating the distributed forces linearly between instrumented sections assuming zero loads at the blade root and tip. A very small relative difference is recorded for the power coefficient (ΔC_P) - less than 1% - for both TSRs, while the estimate of C_T is far less precise. Indeed, although a reasonably small ΔC_T at $TSR = 10$, the thrust on the blades is overestimated by more than 9% at $TSR = 6.7$. The main probable cause of this behaviour lies in the underestimation of the pressure levels at the suction side of the inner parts of the blades, as described in the previous section, which leads to higher load predictions. More in detail, this trend is more pronounced on the pressure profiles at $TSR = 6.7$, which justifies the lower precision for this case.

	$TSR = 6.7$				$TSR = 10$			
	$\boldsymbol{C_P}$	$\boldsymbol{C_T}$	$\lvert\boldsymbol{\Delta C_P}\rvert$ [%]	$\lvert\boldsymbol{\Delta C_T}\rvert$ [%]	$\boldsymbol{C_P}$	$\boldsymbol{C_T}$	$\lvert\boldsymbol{\Delta C_P}\rvert$ [%]	$\lvert\boldsymbol{\Delta C_T}\rvert$ [%]
Exp	0.4358	0.7742	-	-	0.3153	1.019	-	-
Sim	0.4397	0.8458	0.9061	9.243	0.3166	1.041	0.4131	2.234

Table 5.12: Power and thrust coefficients comparison between simulated and experimental results at $TSR = 6.7$ and $TSR = 10$. *PROPAN* predictions include viscous corrections.

In conclusion, it is demonstrated that the panel method *PROPAN* is an extremely valuable tool for wind turbines performance predictions in steady flow conditions. Moreover, the optimal grid resulted from the numerical tests outputs highly accurate load forecasts at $TSR = 10$, therefore it is proved to be a great input for the dynamic inflow case, which has the same TSR.

5.2 Dynamic inflow

As previously discussed in Section 2.4.2, the study of the dynamic inflow conditions focusses on a single experimental set-up (Case A of Table 2.5). This is because wind velocity, rotational speed and consequently TSR are almost identical to the axial flow steady case with $TSR = 10$, allowing to utilise the best grid geometry yielded by the numerical study of Section 5.1. More specifically, the dynamic behaviour of the wind inflow is caused by a variation of the blade pitch angle, which changes from $-2.3°$ to $5.0°$ and eventually back to $-2.3°$, thus it is possible to define three different stages throughout the duration of the experiment, which is about 15 seconds. The first stage is coincident with the axial flow steady case, thus the results achieved from the optimal numerical grid of the steady flow numerical tests are considered constant for the whole timespan of this stage. For the second and third stage,

two different geometries have been defined based on the aligned wake model and the rigid wake model outlined in Section 3.2.3 (with the rigid wake model being used for the unsteady calculations). Finally, the inviscid normal and tangential force coefficients $C_n = \frac{F_n}{1/2\rho V_\infty^2 c}$ and $C_t = \frac{F_t}{1/2\rho V_\infty^2 c}$ obtained by the separate stages have been aggregated and compared to the experimental data.

5.2.1 Wake geometry creation methods

As already discussed, the wake geometry has a large influence on the accuracy of the prediction of the loads on the blades. For this reason, the utilisation of one single type of wake can not be considered sufficient to validate the panel method for dynamic inflow conditions. Two different approaches have been undertaken to create different wake geometries for each stage.

The first method, arbitrarily denominated *IAW* (Independent Aligned Wake), consists of performing three steps:

1. Create a simple wake geometry with *ProPanel* modifying the pitch distribution at the blade trailing edge accordingly to the stage pitch variation,
2. Run a steady simulation activating the wake alignment model for each stage of the dynamic inflow test,
3. Utilise the aligned wake outputted from the simulation as the rigid wake input geometry for the dynamic simulation.

The strength of this approach is to obtain an aligned wake geometry consistent to the pitch variation, while its weakness is to provoke an abrupt transition between the stages. Indeed, the perturbation caused by the pitch modification does not propagate with the same velocity over the wake, meaning that the wake needs more time to adjust to the new blade pitch configuration. Eventually, two distinct aligned wake geometries have been created with this method, one with respect to a blade pitch equal to $-2.3°$ (for Stage 1 and 3) and the other one to $\psi = 5.0°$ (for Stage 2).

The second method, denominated *EAW* (Empirical Aligned Wake), rely on the wake geometry utilised for Stage 1, therefore aligned to the incoming wind flow with $\psi = -2.3°$. It comprehends the following actions:

1. Extract the wake radial pitch distributions at some determined axial (streamwise) positions from the previous stage,
2. Create a rigid wake geometry with *ProPanel* modifying the pitch distribution at the blade trailing edge accordingly to the stage pitch variation and specifying the quantities highlighted in point 1.

In this case the wake geometry is highly dependent on the flow conditions occurring before the pitch variation, since the wake is forced to be consistent to the previous one except at the trailing edge. This might help to better predict the behaviour in the transition periods but lacks of accuracy due to the non-alignment of the wake in relation to the local flow. For every stage, the axial positions (in dimensionless form) selected to extract the wake properties are $x/R = [0.05, 0.10, 0.25, 0.50, 1.0]$. To

clarify this process, Figure 5.21 helps visualise what happens between Stage 1 and 2 at a blade section close to the root (airfoil DU-W2-250). The black and blue dashed lines are used to represent the airfoil

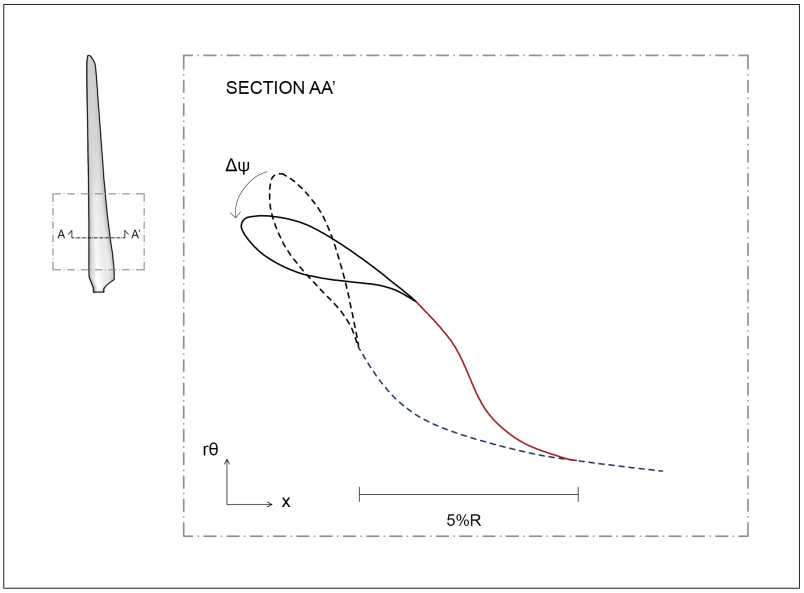

Figure 5.21: Explanatory visual of the Empirical Aligned Wake method (EAW).

and wake, respectively, for Stage 1. When passing to Stage 2 the pitch angle increases, which means that the airfoil becomes less inclined with respect to the axial (streamwise) axis (black solid line) and the wake (red solid line) changes accordingly. When the EAW method is applied, the wake shed from the trailing edge is kept consistent to the new pitch setting ($\psi = 5.0°$) up to $x/R = 0.05$, whereas after that streamwise position it is modified such that it coincides with the aligned Stage 1 wake geometry.

It is important to stress that:

1. Stage 3 *EAW* geometry is built on the Stage 2 *EAW* geometry, not from the *IAW* one, thus for both of these stages the *EAW* geometries extending from $x/R = 0.05$ are the same as for Stage 1,

2. Stage 3 *EAW* geometry differs from the Stage 3 *IAW* one (which is exactly the same as the one utilised in Stage 1).

5.2.2 Simulation set-up

The simulation procedure for the dynamic inflow study is partially different from the one described in Section 5.1.1, because initial conditions need to be specified for each stage. This leads to requiring a mix of additional input files and improvements on the existing ones.

Pre-processing

In addition to the modifications of the grid geometry which varies due to the blade pitch, the fundamental quantities that must be expressed for each stage are:

- Number of revolutions that the rotor completes during that stage (N_{rev}),
- Properties of the last time step of the solution file from the previous stage,
- Circulation of the last time step from the previous stage (Γ),
- Definition of the wake geometry.

It is evident that each stage is linked to its previous one, thus the outcome of the latter, in terms of flow properties, must be considered as the starting point for the following stage. In particular, the last point has a relevant impact on the accuracy of the results, thus it has been heavily analysed for all the stages.

Processing

The potential flow results are assessed for each time step, which corresponds to a specific time step of a particular revolution. To give an indication on the order of magnitude of the total number of time steps (N_t), if $N_{rev} = 10$ and the angular step $\Delta\theta = 4°$, then $N_t = 900$. As one can understand, the higher the number of revolutions, the longer it takes to develop a full simulation, therefore it is largely important to evaluate which revolutions are strictly necessary to capture the dynamic behaviour of the flow and which ones can be omitted.

Post-processing

As for the pre-processing part, the post-processing tool *ProPost* requires the number of revolutions as a mandatory input. Thus, the viscous correction are applied to the potential flow outcomes of each time step.

5.2.3 Simulation stages

From the analysis of the experimental data, three different stages can be highlighted: the first one comprehends the initial phase when the pitch angle is equal to $-2.3°$, the second one when the blade pitch is $5.0°$, while the final stage blade pitch returns to $-2.3°$. In Figure 5.22 the experimental trend of the blade pitch angle ψ is illustrated as an example to visualise the distinction of the three stages. The variation of the blade pitch occurs relatively fast and creates two transition time frames where two opposite effects occur - a force undershoot between Stage 1 and 2 and a force overshoot between Stage 2 and 3 - which must be studied with great attention. These phenomena happen because the axial induced velocity in the rotor plane and the associated axial induction respond to the pitch variation only with time delay due to the inertia of the global flow field. This results in very fast variations of the loads experienced by the blades, which vanish only after a certain period [40].

Stage 2

The second stage interval has been assessed between 1.5 and 7.2 seconds, equal to 41 revolutions of the blade rotor, in order to include the transition phase between Stage 1 and 2 and exclude the one

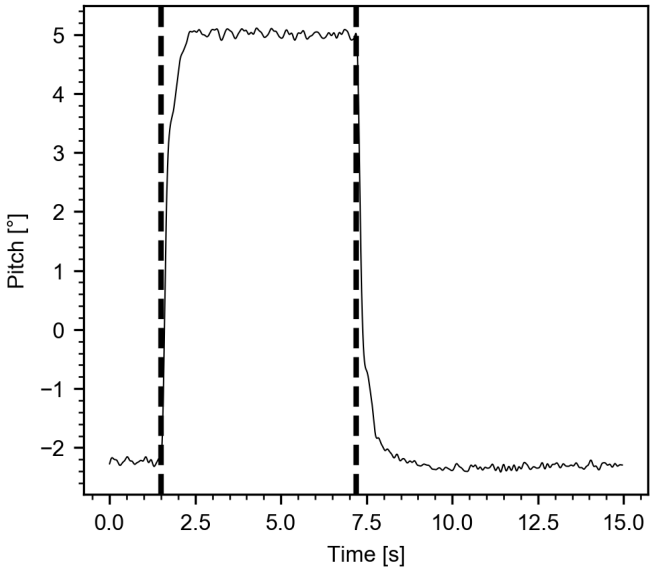

Figure 5.22: Stages definition - the different stages are separated by the dashed vertical lines.

between Stage 2 and 3.

The inviscid normal force coefficients for different blade radial positions outputted from the *EAW* and *IAW* simulations are shown in Figure 5.23. The overall trend is composed by a peak value at the beginning of the stage (derived from Stage 1) to then drop rapidly to reach the steady solution for the new pitch configuration. It is evident that the predicted forces are heavily different for the two methods, especially in the steady behaviour. Interestingly, this discrepancy has its maximum magnitude at $r/R = 25\%$ and decreases progressively while approaching the blade tip, with the *IAW* results being greater than the *EAW* ones for every radial position. It is also possible to notice that for the *EAW* geometry, numerical oscillations occur and have an increasing influence towards the outer sections of the blade.

The same identical considerations can be applied to the inviscid tangential force coefficients, shown in Figure 5.24. Additionally, a small jump at around $t = 5s$ is predicted for C_n and C_t at every radial position when utilising the *EAW* method. It is not clear why this phenomenon occurs, especially because the numerical oscillations experienced at the beginning of the simulation seem to disappear already at $t = 3s$ and after that time the results seem to smoothly converge at the equilibrium value. Therefore, in terms of numerical convergence, the *IAW* method might be labelled as the most reliable one, since no relevant fluctuations are forecast.

Figure 5.25 shows the pitch of the two wake geometries for different axial positions. As expected, the two geometries are largely diverse, with the *IAW* one having a greater pitch for the entire radial direction for all the streamwise locations. One can also notice that the *EAW* pitch is highly fluctuating at $X_V = 0.05$. The main reason for that is the geometrical transition from the wake derived from the new blade pitch configuration to the one generated from previous blade pitch setting (Stage 1), as shown in Figure 5.21.

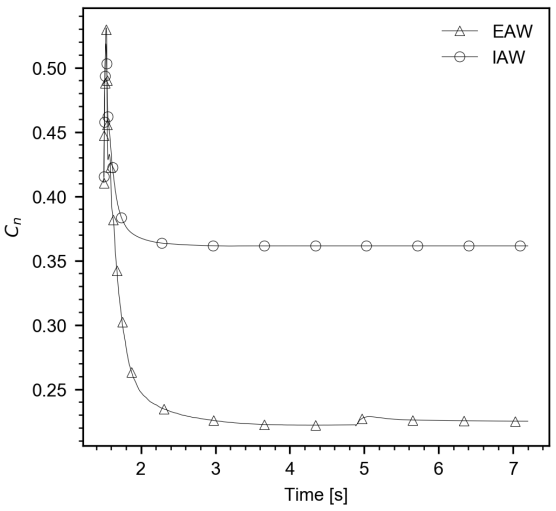

(a) $r/R = 25\%$

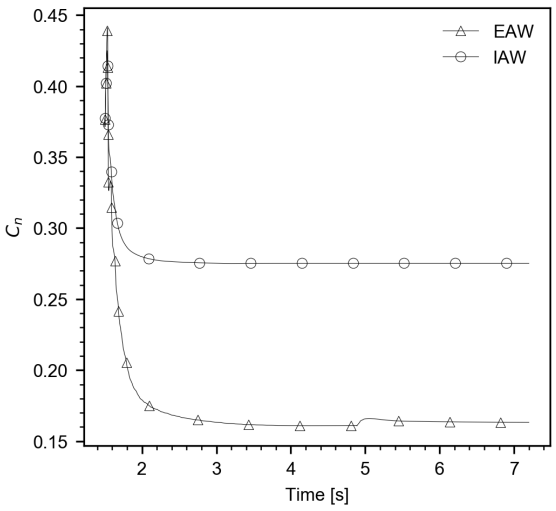

(b) $r/R = 35\%$

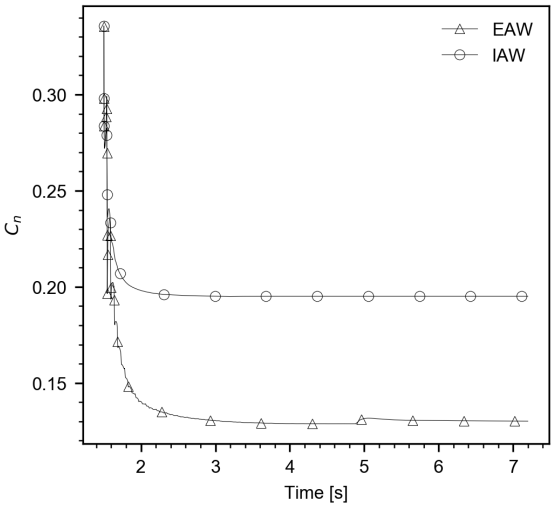

(c) $r/R = 60\%$

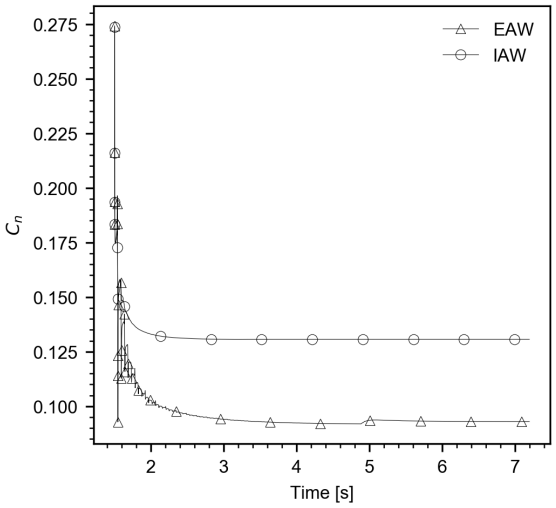

(d) $r/R = 82\%$

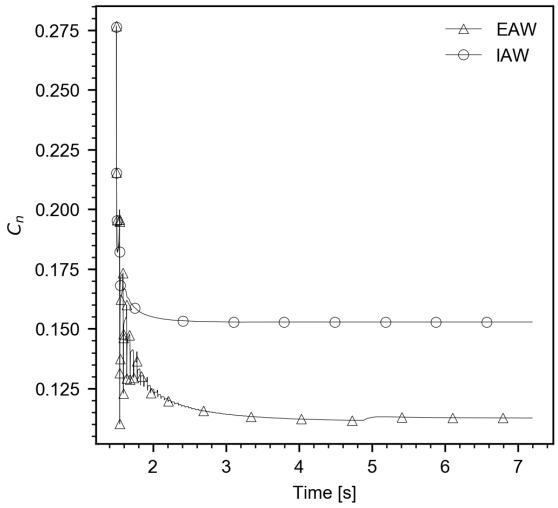

(e) $r/R = 92\%$

Figure 5.23: Stage 2 normal force coefficient comparison between *EAW* and *IAW* results for different radial positions.

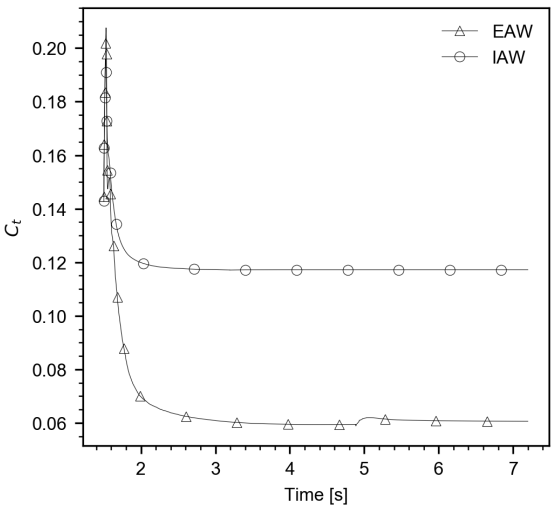

(a) $r/R = 25\%$

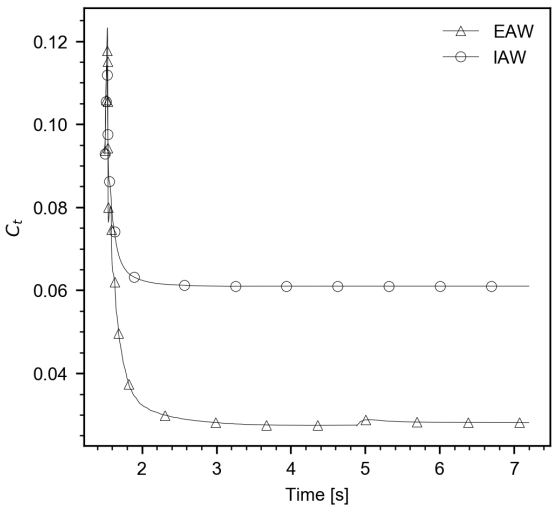

(b) $r/R = 35\%$

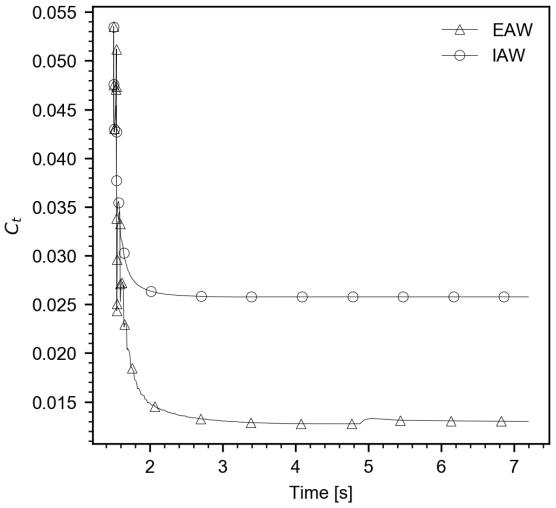

(c) $r/R = 60\%$

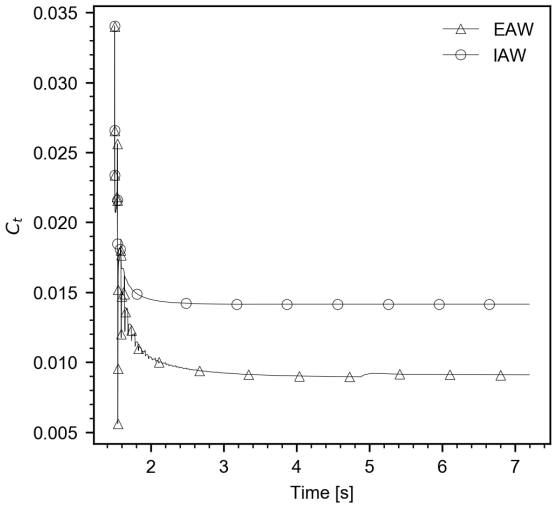

(d) $r/R = 82\%$

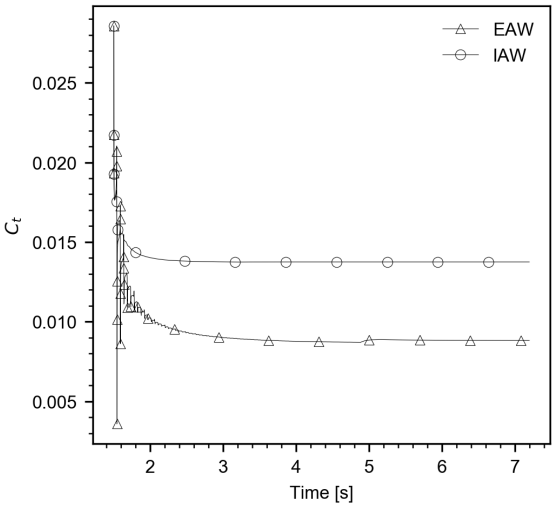

(e) $r/R = 92\%$

Figure 5.24: Stage 2 tangential forces coefficient comparison between *IAW* and *EAW* results for different radial positions.

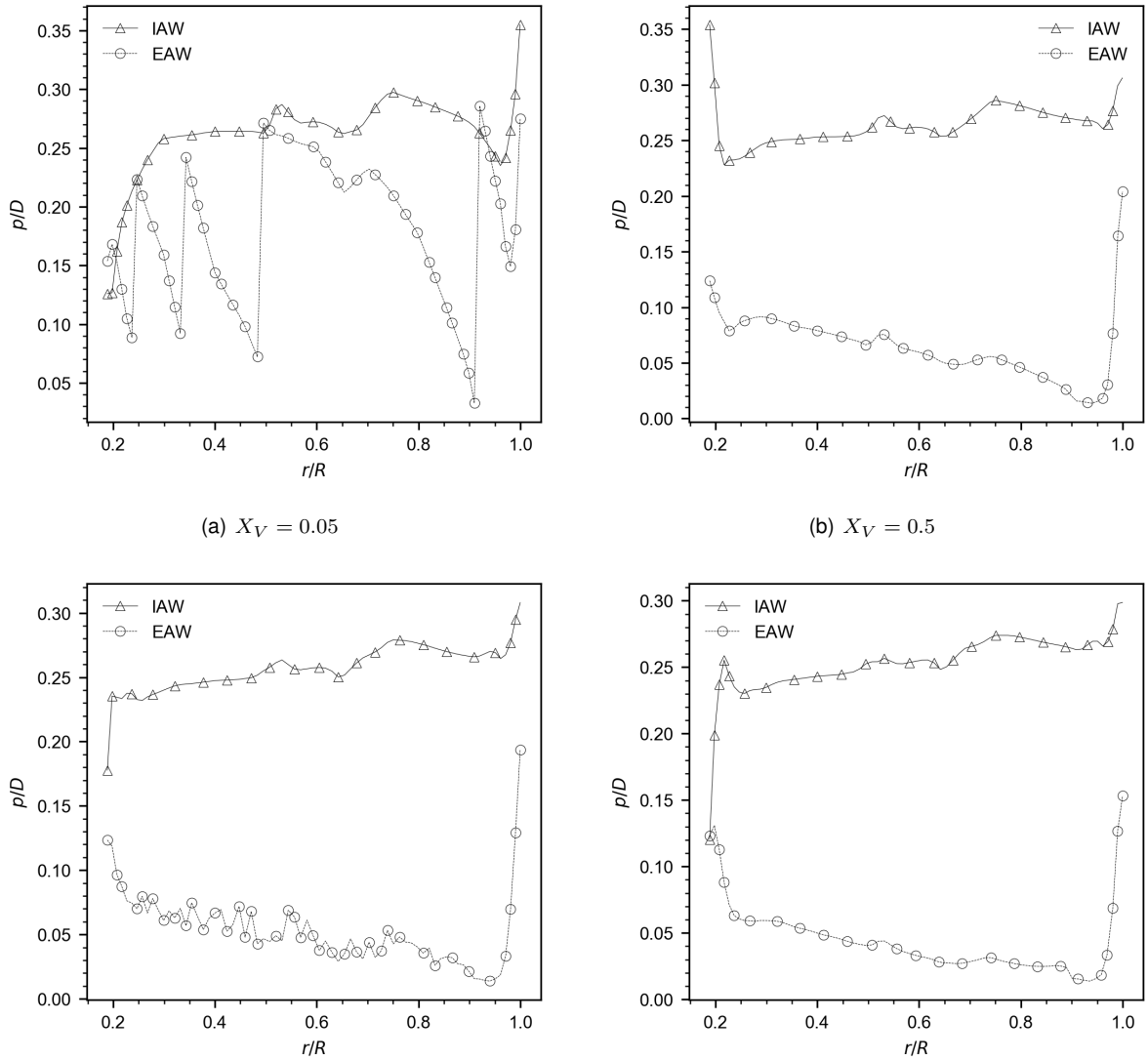

(a) $X_V = 0.05$

(b) $X_V = 0.5$

(c) $X_V = 1.0$

(d) $X_V = 2.0$

Figure 5.25: Stage 2 wake pitch comparison between *IAW* and *EAW* geometries at different axial positions.

Stage 3

The third stage has been defined to include the transient behaviour between Stage 2 and 3. It consists of 54 rotor revolutions, which correspond to a time frame of 7.8 seconds (from 7.2 to 15 seconds), where the blade pitch is set back to its original magnitude ($\psi = -2.3°$). As a consequence, the *IAW* geometry coincides with the one utilised for Stage 1, while the *EAW* geometry is derived considering the wake of the previous stage and the variation of the pitch distribution at the blade trailing edge.

As can be seen by the experimental measurements (Figure 2.6), when focussing only on Stage 3 the normal and tangential forces become steady already between 10 and 12 seconds, therefore the results have been achieved cutting the number of total revolutions to 34, equal to reaching 12 seconds.

Figure 5.26 and Figure 5.27 show the results for the inviscid normal and tangential force coefficients.

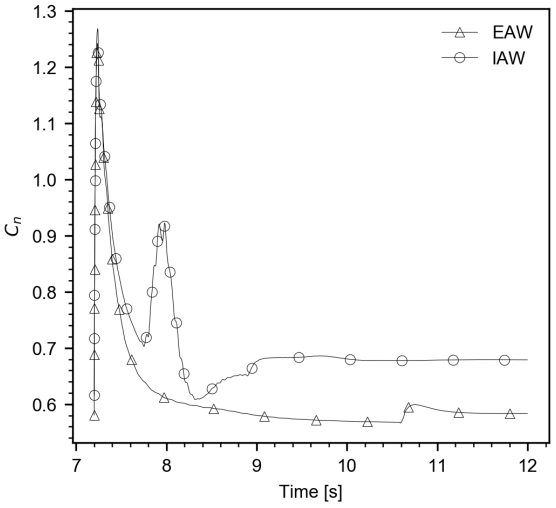

(a) $r/R = 25\%$

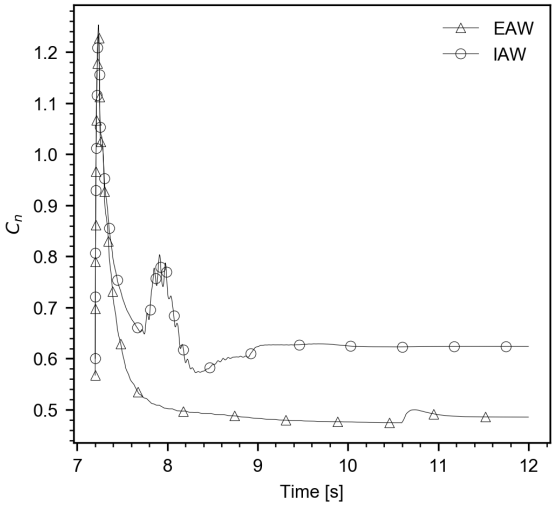

(b) $r/R = 35\%$

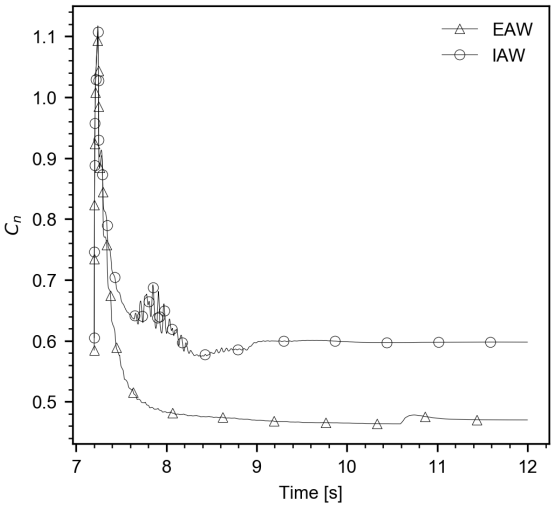

(c) $r/R = 60\%$

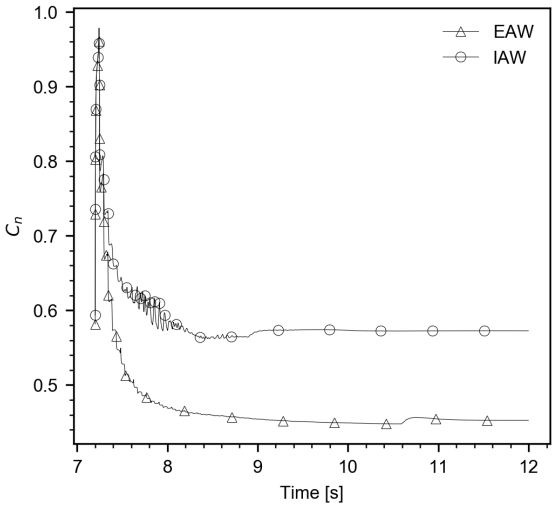

(d) $r/R = 82\%$

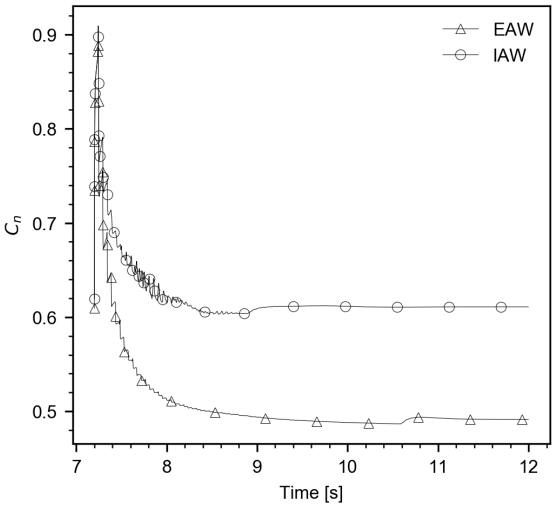

(e) $r/R = 92\%$

Figure 5.26: Stage 3 normal forces coefficient comparison between *IAW* and *EAW* results for different radial positions.

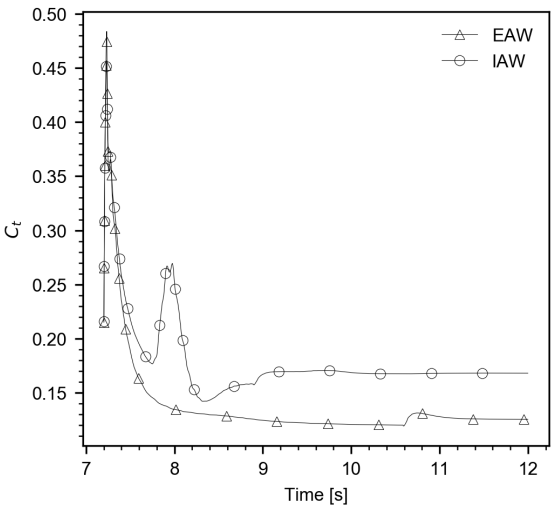

(a) $r/R = 25\%$

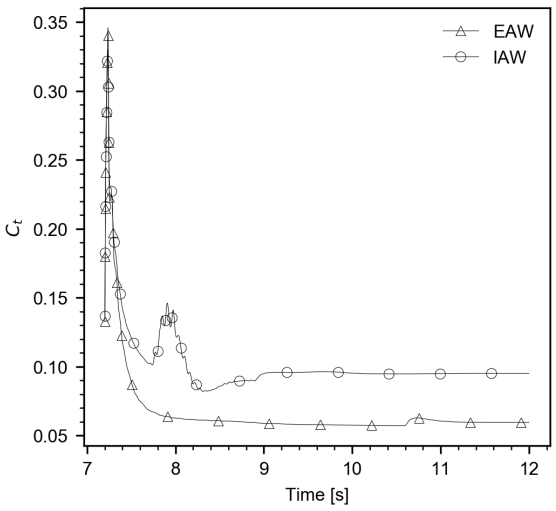

(b) $r/R = 35\%$

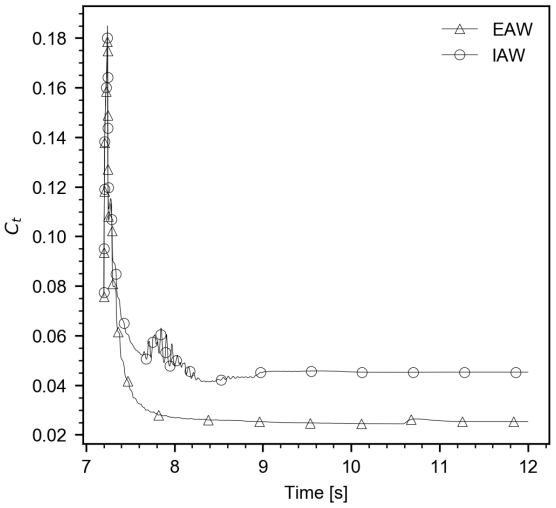

(c) $r/R = 60\%$

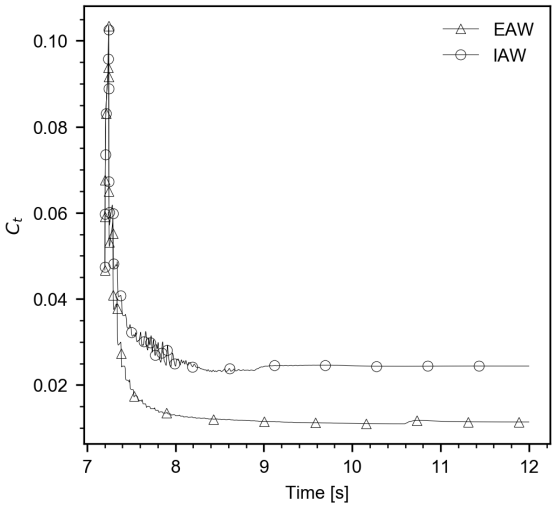

(d) $r/R = 82\%$

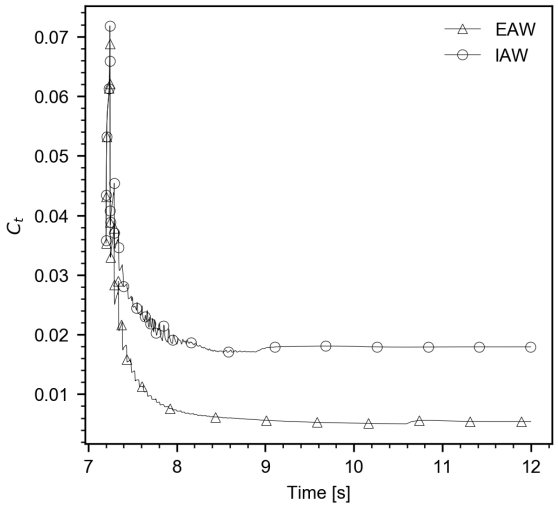

(e) $r/R = 92\%$

Figure 5.27: Stage 3 tangential forces coefficient comparison between *IAW* and *EAW* results for different radial positions.

Accordingly with Stage 2, *IAW* estimates are always larger than the *EAW*. However, complete opposite predictions are seen when evaluating the numerical quality of the simulations. Indeed, the *EAW* method yields almost no oscillations, while *IAW* produces high frequency fluctuations between 7.5 and 8.5 at $r/R = 60\%$, $r/R = 82\%$ and $r/R = 92\%$, which gradually diminish towards the blade tip. Moreover, within the same time frame, at the radial sections $r/R = 25\%$ and $r/R = 35\%$ the numerical oscillations are replaced by a distinct peak.

In the search for the causes of this phenomenon, the following initial guesses were made:

- Divergence of the Kutta condition,
- Anomalies in the pressure distributions,
- Problems with the application of viscous effects.

After verifying all these hypotheses, none of them could be labelled as the cause of this behaviour, since the Kutta condition converges after just three iterations, the pressure profiles do not present any particular anomaly and the potential force coefficients have the same trend of the viscous ones. Eventually, the most probable cause might be the abrupt change of wake geometry that occurs when passing from Stage 2 to Stage 3, due to the large numerical instability deriving from the instantaneous transition.

5.2.4 Discussion of the results

The trends of the entire simulation, made up from the aggregation of the separate stages and compared with the experimental results, are presented in Figure 5.28 and Figure 5.29. It is worth mentioning that due to the large recorded oscillations, the measured data has been denoised through the application of a moving average function.

Starting from analysing Stage 1 (in which the numerical steady-flow wake geometry is used), a good prediction of the results is calculated only for the C_n at $r/R = 92\%$. For the remaining blade sections, the simulated C_n and C_t are consistently different from the experimental data, especially towards the blade root.

When the pitch is varied to the Stage 2 configuration, the experiments show a clear undershoot in the forces, which presents some oscillations leading to a ”double” negative peak. The same observation can be drawn from the transient phase between Stage 2 and Stage 3: there is a distinct overshoot with two positive peaks before stabilising to the equilibrium. This phenomenon does not happen in reality, therefore it is believed to be due to a fault in the pressure sensors, which might be affected by the tower vibrations.

In Stage 2, the overall trends of the simulated force coefficients are qualitatively consistent to the experimental measurements, even though large discrepancies occur in the transient time frame, where unexpected peaks are seen. In particular, the trend of the simulated normal force coefficients is similar to the experimental one, except for the first two radial positions where the *EAW* method largely underestimates the forces at the equilibrium. The *IAW* geometry yields the best outcomes in terms

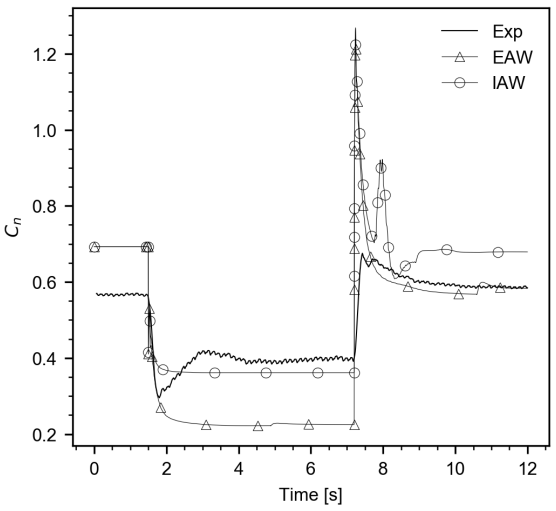

(a) $r/R = 25\%$

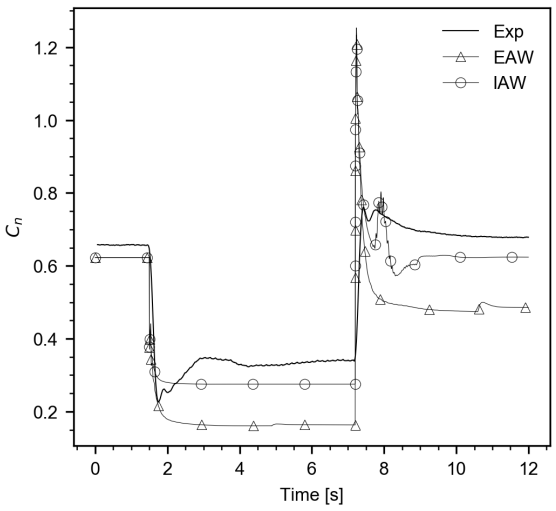

(b) $r/R = 35\%$

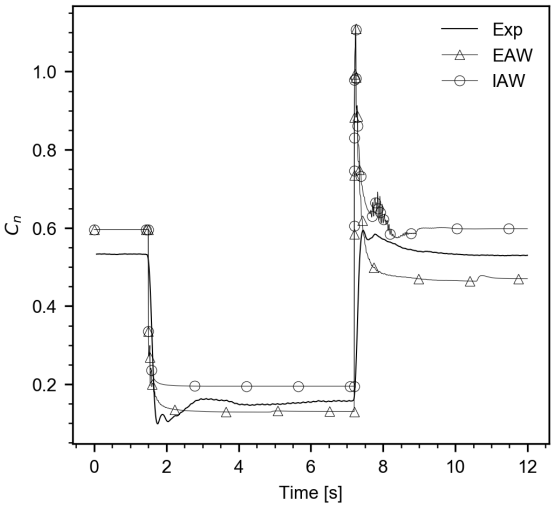

(c) $r/R = 60\%$

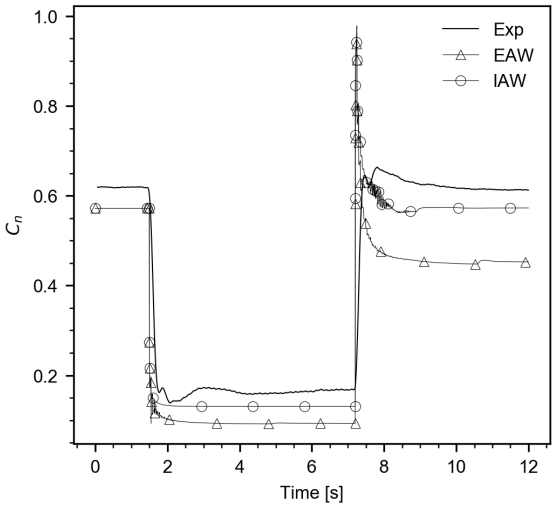

(d) $r/R = 82\%$

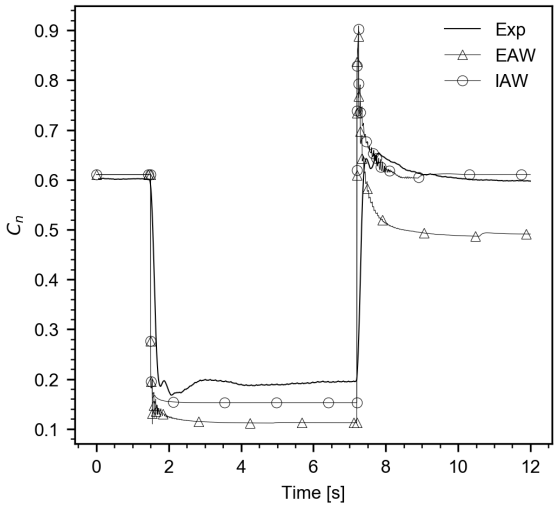

(e) $r/R = 92\%$

Figure 5.28: All stages normal forces coefficient comparison between experimental, *IAW* and *EAW* results for different radial positions.

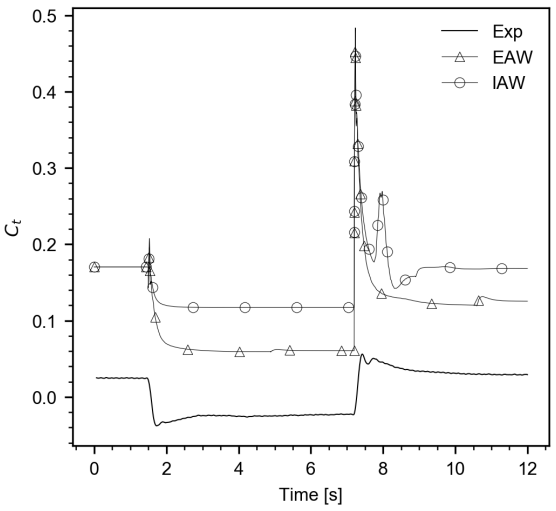

(a) $r/R = 25\%$

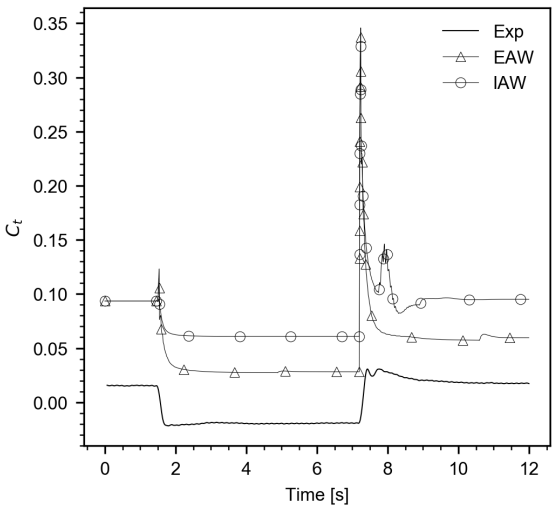

(b) $r/R = 35\%$

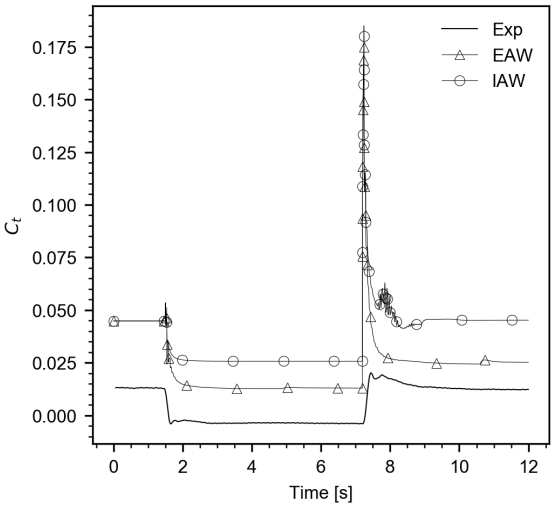

(c) $r/R = 60\%$

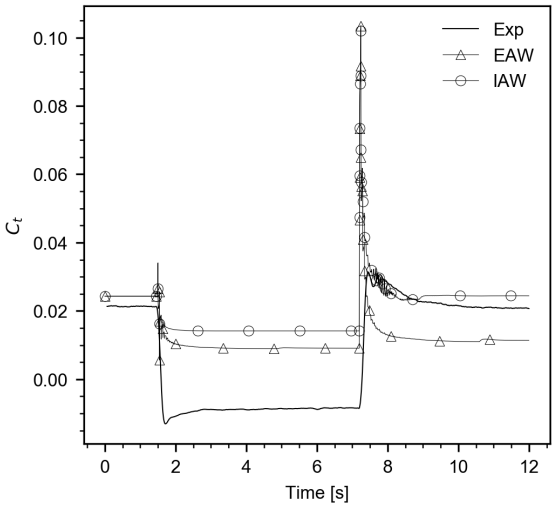

(d) $r/R = 82\%$

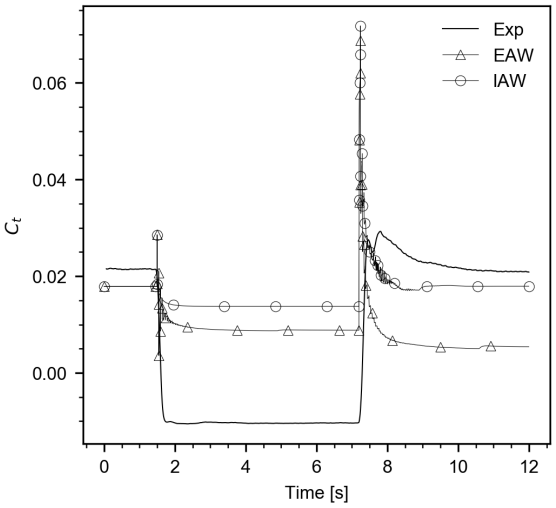

(e) $r/R = 92\%$

Figure 5.29: All stages tangential forces coefficient comparison between experimental, *IAW* and *EAW* results for different radial positions.

of agreement with the experimental results for every radial position but $r/R = 60\%$, where the normal forces are slightly overestimated. The opposite tendency is observed for the tangential force coefficients: the *EAW* results are always closer to the experimental data than the *IAW* ones.

Regarding Stage 3, clearly the predicted overshoot is extremely overestimated for both C_n and C_t. The results obtained for the normal force coefficients suggest that, compared to Stage 2 where the *IAW* geometry is the most accurate for every radial position but one, the *EAW* method predicts C_n at $r/R = 25\%$ with great precision and differs from the experimental data with the same magnitude of the *EAW* method at $r/R = 60\%$. For the remaining radial positions, the *IAW* geometry yields the best outcomes, especially at $r/R = 92\%$. On the other hand, the *EAW* estimates are more precise for the tangential forces, performing better than the *IAW* geometry for three radial positions. In addition, it can be seen that the *EAW* steady results are different from the Stage 1 results, indicating that the initial and final wake geometries are not coincident.

Finally, the following main considerations can be outlined:

- On the whole, the panel method predictions are in reasonable agreement with the experimental measurements, particularly when reaching the steady solution, making the panel method a reliable tool.

- From the comparison of the normal and tangential forces along the blades, no specific wake method is clearly the optimal one. The *IAW* geometry has a greater accuracy than the *EAW* one on the normal forces coefficient, while the opposite trend is observed for the tangential forces. However the *EAW* geometry is more unstable in terms of numerical oscillations.

- Compared to the steady calculations, the time required for running the dynamic simulations (utilising one CPU) is considerably larger. For instance, the computational time of the results obtained for Stage 2 is around 140 hours, equal to about 6 days, on a Xeon processor at 2.6GHz with 125GB of RAM. If one takes into account the duration of all the stages, then an average of 3.5 hours per rotor revolution can be assessed.

- The main discrepancies between the simulated and experimental results are seen in the transient time frames, especially in the one between the second and third stage.

Focussing on the last point, as briefly explained in Section 1.3, the load undershoot (between Stage 1 and 2) and overshoot (between Stage 2 and 3) are a result of the lag in induced velocity caused by the new pitch setting. More specifically, when the pitch angle is decreased, the angle of attack suddenly increases, which leads to an almost instantaneous increase of the forces on the blades. The same occurs in the opposite way, thus if the pitch increases the angle of attack drops. The forces are then brought to equilibrium only when the induced velocities have gradually adjusted to the new inflow conditions. The latter takes place with a time scale in the order of D/U, which is much longer than the time scale from the instationary airfoil aerodynamics $(c/(\Omega r))$ [30]. These effects are extremely evident in the experimental observations, whereas *PROPAN* can not predict them properly. In the case of the undershoot, the simulated values are similar to the experimental ones but no real undershoot is

reached: the forces smoothly decrease to achieve the equilibrium. Regarding the overshoot, although the presence of a distinct peak, the forces increase is largely overestimated in both wake methods. The main reason for this behaviour is the abrupt pitch modification between one stage and the following one: the experiment is conducted to have a variable pitch step, while the simulations are built upon an instantaneous change of the pitch setting.

Chapter 6

Conclusions

In this final chapter the most important achievements of this work are summarised and presented. Possible future improvements and analyses are also suggested.

6.1 Achievements

The goal of this thesis was to test the in-house panel method code *PROPAN* developed at IST for wind turbines under steady and dynamic inflow conditions. In order to validate the method, the results obtained both from the steady and dynamic simulations have been compared to the measurements performed on the wind turbine utilised in the New MEXICO experiments.

A thorough numerical study under steady inflow conditions has been described, aiming at assessing the best wake geometry and grid configuration for two undisturbed wind velocities, 10.05 m/s ($TSR = 10$) and 15.06 m/s ($TSR = 6.7$). A wake alignment model was used for all the tests. Convergence of the numerical results is achieved with a longer wake length and greater grid refinement along the radial and chordwise direction of the blade, while no relevant differences are observed for the hub. When comparing the simulated results with the experimental data, a good agreement is generally found. The predictions of the pressure distribution are extremely accurate for the sections closer to the blade tip, while small discrepancies are seen towards the root. Power coefficients also match precisely the experimental data for both TSRs, having a relative error of less than 1%. However, the same accuracy can not be reached for the thrust coefficients, with the largest relative error (about 10%) happening at $TSR = 6.7$.

When passing to the dynamic simulations, the numerical optimal grid obtained at $TSR = 10$ was utilised, since only one dynamic case from the New MEXICO measurements was considered for validation purposes. The dynamic variation of the blade pitch angle ψ has been simulated through the definition of three different stages, assuming an instantaneous behaviour. The first stage represents the steady inflow condition studied in the numerical tests. For the second and third stage, two different methods to create the wake geometry were applied, with the main difference of yielding a wake geometry partially or fully aligned to the incoming wind flow. The experimental normal and tangential forces

experienced on the blade at five specific radial sections were compared to the simulated results. Overall, the trends of the forces predicted with both wake geometries are comparable to the experimental ones when achieving the periodic solution. However, the main limitation of *PROPAN* lies in the inaccurate estimation of the force undershoot and overshoot occurring in the first instances of Stage 2 and 3, respectively. Additionally, high-frequency numerical oscillations are witnessed, suggesting that further analyses on the geometry and grid quality of the turbine model must be done.

6.2 Future Work

The accuracy of predictions obtained with *PROPAN* demonstrates and confirms that it is a very accurate tool for wind turbine performance predictions under steady inflow conditions. As a consequence, the major future developments on the code must be centred around the dynamic inflow simulations, which currently cannot be modelled precisely. Most importantly, corrections must be applied in order to enable the prediction of the undershoot and overshoot of the forces that occur in the initial instances of the dynamic behaviour. In relation to that, the abrupt division of the simulation stages shown in this work must be avoided, so that a smoother transition can be implemented. An additional improvement on the code might be found in reducing the computational time needed for running the simulations. This can be done by enabling parallel processing, which is normal practice for CFD simulations.

However, before developing new features on the code, additional tests can be done starting from the simulations presented in this work:

- Evaluate the *EAW* results for Stage 3 obtained with a wake geometry created from the *IAW* geometry of Stage 2,
- Apply the wake alignment model for each time step of each stage,
- Ameliorate the input files needed when transitioning to a the different stage.

The latter means to be more precise in the creation of the input files outlined in Section 5.2.2. Indeed in this work only the circulation and the geometrical parameters of the last time step are considered, while some interpolation between multiple time steps might be helpful to better predict the transitory behaviour.

Bibliography

[1] IRENA. Future of wind - Deployment, investment, technology, grid integration and socio-economic aspects. Technical report, IRENA, 2019.

[2] M. Johari, M. Jalil, and M. F. M. Shariff. Comparison of horizontal axis wind turbine (HAWT) and vertical axis wind turbine (VAWT). *International Journal of Engineering and Technology*, 7(4.13): 74–80, 2018.

[3] P. J. Schubel and R. J. Crossley. Wind Turbine Blade Design. *Energies*, 5(9):3425–3449, Sep 2012. ISSN 1996-1073. doi: 10.3390/en5093425. URL http://dx.doi.org/10.3390/en5093425.

[4] D. B. Melo, J. Baltazar, and J. A. C. Falcão de Campos. A numerical wake alignment method for horizontal axis wind turbines with the lifting line theory. *Journal of Wind Engineering and Industrial Aerodynamics*, 174:382 – 390, 2018. ISSN 0167-6105. doi: https://doi.org/10.1016/j.jweia.2018.01.028. URL http://www.sciencedirect.com/science/article/pii/S0167610517304427.

[5] P. Nigam, N. Tenguria, and D. M. Pradhan. Review on Design of Horizontal Axis Wind Turbine Blades. 12 2018. doi: 10.1729/Journal.22831.

[6] Z. Yang. *Wind Turbine Controls for Farm and Offshore Operation*. PhD thesis, 12 2013.

[7] M. M. Aslam Bhutta, N. Hayat, A. U. Farooq, Z. Ali, S. R. Jamil, and Z. Hussain. Vertical axis wind turbine – A review of various configurations and design techniques. *Renewable and Sustainable Energy Reviews*, 16(4):1926 – 1939, 2012. ISSN 1364-0321. doi: https://doi.org/10.1016/j.rser.2011.12.004. URL http://www.sciencedirect.com/science/article/pii/S136403211100596X.

[8] F. Castellani, D. Astolfi, M. Peppoloni, F. Natili, D. Buttà, and A. Hirschl. Experimental Vibration Analysis of a Small Scale Vertical Wind Energy System for Residential Use. *Machines*, 7:35, 05 2019. doi: 10.3390/machines7020035.

[9] S. Sang, H. Wen, A. Cao, X. Du, X. Zhu, Q. Shi, and C. Qiu. Dynamic modification method for BEM of wind turbine considering the joint action of installation angle and structural pendulum motion. *Ocean Engineering*, 215:107528, 2020. ISSN 0029-8018. doi: https://doi.org/10.1016/j.oceaneng.2020.107528. URL http://www.sciencedirect.com/science/article/pii/S0029801820305400.

[10] J. G. Schepers. *Engineering models in wind energy aerodynamics: Development, implementation and analysis using dedicated aerodynamic measurements*. PhD thesis, TU Delft, 2012.

[11] R. S. Pereira. Lecture Slides - The Blade Element Momentum Theory of a Turbine.

[12] S. Hauptmann, M. Bülk, L. Schön, S. Erbslöh, K. Boorsma, F. Grasso, M. Kühn, and P. W. Cheng. Comparison of the lifting-line free vortex wake method and the blade-element-momentum theory regarding the simulated loads of multi-MW wind turbines. *Journal of Physics: Conference Series*, 555:012050, dec 2014. doi: 10.1088/1742-6596/555/1/012050. URL https://doi.org/10.1088%2F1742-6596%2F555%2F1%2F012050.

[13] B. Epps and R. Kimball. Unified Rotor Lifting Line Theory. *Journal of Ship Research*, 57:181–201, 12 2013. doi: 10.5957/JOSR.57.4.110040.

[14] J. L. Hess and A. M. O. Smith. Calculation of Nonlifting Potential Flow About Arbitrary Three-Dimensional Bodies. *Journal of Ship Research*, Vol. 8(2):22–44, 1964.

[15] E. Houghton, P. Carpenter, S. H. Collicott, and D. T. Valentine. Chapter 6 - Thin Airfoil Theory. In E. Houghton, P. Carpenter, S. H. Collicott, and D. T. Valentine, editors, *Aerodynamics for Engineering Students (Seventh Edition)*, pages 391–447. Butterworth-Heinemann, seventh edition edition, 2017. ISBN 978-0-08-100194-3. doi: https://doi.org/10.1016/B978-0-08-100194-3.00006-7. URL https://www.sciencedirect.com/science/article/pii/B9780081001943000067.

[16] J. L. Hess. The problem of three-dimensional lifting potential flow and its solution by means of surface singularity distribution. *Computer Methods in Applied Mechanics and Engineering*, 4 (3):283–319, 1974. ISSN 0045-7825. doi: https://doi.org/10.1016/0045-7825(74)90009-7. URL https://www.sciencedirect.com/science/article/pii/0045782574900097.

[17] L. Morino and C.-C. Kuo. Subsonic Potential Aerodynamics for Complex Configurations : A General Theory. *AIAA Journal*, 12(2):191–197, 1974. doi: 10.2514/3.49191. URL https://doi.org/10.2514/3.49191.

[18] S. Pyo. *Numerical Modelling of Propeller Tip Flows With Wake SheetRoll-up in Three Dimensions*. PhD thesis, Masschusetts Institute of Technology, 1995.

[19] C. Hsin, J. E. Kerwin, and S. A. Kinnas. A Panel Method for the Analysis of the Flow Around Highly Skewed Propellers. In *Proceedings of the Propellers/Shafting'91 Symposium*, 1991.

[20] J. Baltazar and J. A. C. Falcão de Campos. Unsteady Potential Flow Calculations of Marine Propellers Using BEM. 06 2006.

[21] J. Baltazar and J. A. C. Falcão de Campos. Unsteady Analysis of a Horizontal Axis Marine Current Turbine in Yawed Inflow Conditions With a Panel Method. 06 2009.

[22] J. Baltazar, D. Rijpkema, J. A. C. Falcão de Campos, and J. Bosschers. A Comparison of Panel Method and RANS Calculations for a Ducted Propeller System in Open-Water. In *Third International Symposium on Marine Propulsors smp'13*, 2013.

[23] S. Brizzolara, D. Villa, and S. Gaggero. A systematic comparison between RANS and panel methods for propeller analysis. In *Proc. Of 8th International Conference on Hydrodynamics, Nantes, France*, 2008.

[24] M. Hansen, J. Sørensen, J. Michelsen, and N. Sørensen. A global Navier-Stokes rotor prediction model. In *35th Aerospace Sciences Meeting and Exhibit*, page 970, 1997.

[25] N. Sørensen and M. Hansen. Rotor performance predictions using a Navier-Stokes method. In *1998 ASME Wind Energy Symposium*, page 25, 1998.

[26] G. Xu and L. N. Sankar. Computational study of horizontal axis wind turbines. *J. Sol. Energy Eng.*, 122(1):35–39, 2000.

[27] N. Sørensen and J. Michelsen. Aerodynamic predictions for the unsteady aerodynamics experiment phase-II rotor at the National Renewable Energy Laboratory. In *2000 ASME Wind Energy Symposium*, page 37, 2000.

[28] S. Kang and C. Hirsch. Features of the 3D flow around wind turbine bladesbased on numerical solutions. In *Proceedings of EWEC 06*, 2001.

[29] J. Sørensen and W. Z. Shen. Numerical Modeling of Wind Turbine Wakes. *Journal of Fluids Engineering*, 124:393, 06 2002. doi: 10.1115/1.1471361.

[30] J. G. Schepers. IEA Annex XX. Dynamic Inflow effects at fast pitching steps on a wind turbine placed in the NASA-Ames wind tunnel, Oct 2007.

[31] P. Odgaard, T. Knudsen, A. Overgaard, H. Steffensen, and M. Jørgensen. Importance of Dynamic Inflow in Model Predictive Control of Wind Turbines. *IFAC-PapersOnLine*, 48:90–95, 12 2015. doi: 10.1016/j.ifacol.2015.12.359.

[32] J. Baltazar. *On the Modelling of the Potential Flow About Wings and Marine Propellers Using a Boundary Element Method*. PhD thesis, IST, 2008.

[33] K. Boorsma, J. G. Schepers, S. Gomez-Iradi, I. Herraez, T. Lutz, P. Weihing, L. Oggiano, G. Pirrung, H. A. Madsen, W. Z. Shen, H. Rahimi, and P. Schaffarcyk. Final report of IEA Wind Task 29 Mexnext (Phase 3). Technical report, ECN, 2018.

[34] K. Boorsma and J. G. Schepers. Description of Experimental Setup. Technical report, ECN, 2017.

[35] M. D. Atkins. Chapter 5 - Velocity Field Measurement Using Particle Image Velocimetry (PIV). In T. Kim, T. J. Lu, and S. J. Song, editors, *Application of Thermo-Fluidic Measurement Techniques*, pages 125 – 166. Butterworth-Heinemann, 2016. ISBN 978-0-12-809731-1. doi: https://doi.org/10.1016/B978-0-12-809731-1.00005-8. URL `http://www.sciencedirect.com/science/article/pii/B9780128097311000058`.

[36] N. N. Sørensen, J. A. Michelsen, and S. Schreck. Navier-Stokes predictions of the NREL phase VI rotor in the NASA Ames 80 ft x 120 ft wind tunnel, Jul 2002.

[37] J. Baltazar, J. A. C. Falcão de Campos, and J. Bosschers. Open-Water Thrust and Torque Predictions of a Ducted Propeller System with a Panel Method. *International Journal of Rotating Machinery*, 2012.

[38] *Propeller Geometry: Terms and Definitions*. Michigan Weel Engineering, 2000.

[39] L. Eça. Grid Generation With a System of Elliptical Partial Differential Equations. Technical report, 1994.

[40] F. Berger and M. Kühn. Experimental investigation of dynamic inflow effects with a scaled wind turbine in a controlled wind tunnel environment. *Journal of Physics: Conference Series*, 1037: 052017, 06 2018. doi: 10.1088/1742-6596/1037/5/052017.

Appendix A

Additional blade sections

In this annex the additional sections created to define the blade geometry are presented, as defined in Section 4.1.1.

A.1 Cylinder - DU

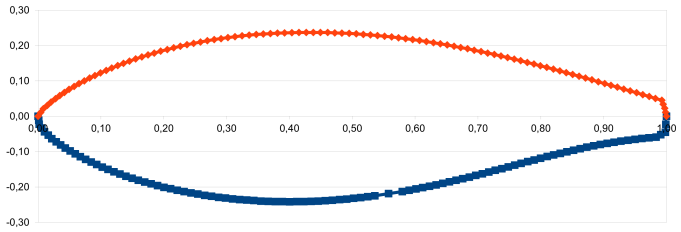

(a) Section 1A

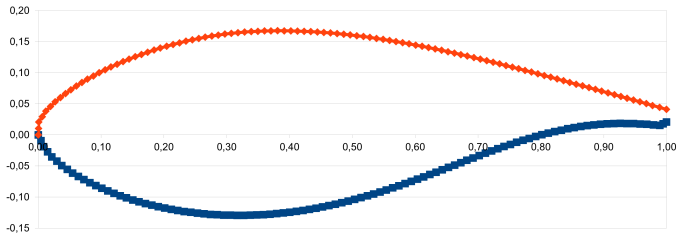

(b) Section 2A

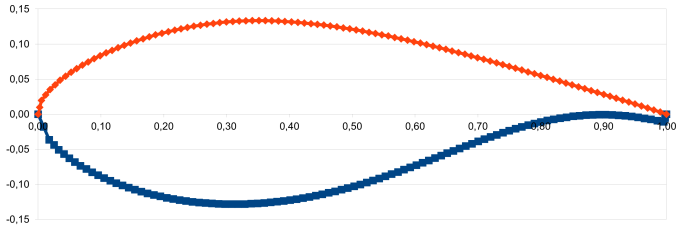

(c) Section 3A

Figure A.1: Additional blade sections between the cylinder and DU airfoil.

A.2 DU - RISØ

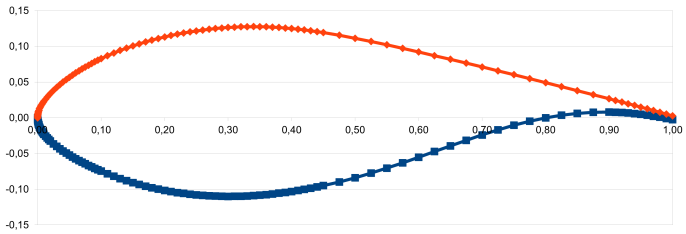

(a) Section 1B

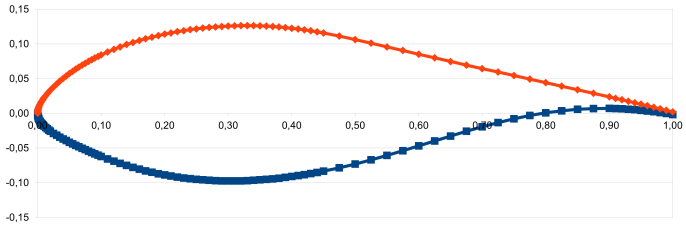

(b) Section 2B

Figure A.2: Additional blade sections between the DU and RISØ airfoils.

A.3 RISØ - NACA

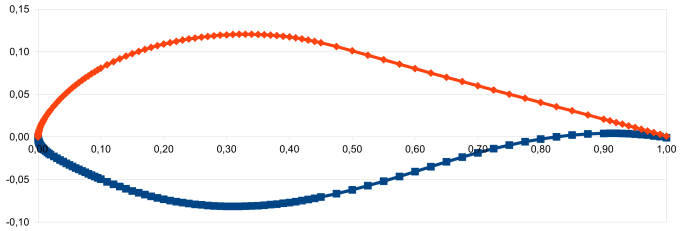

(a) Section 1C

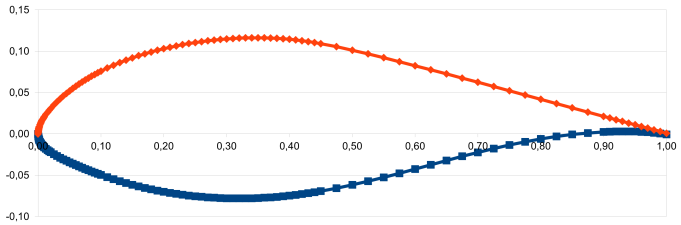

(b) Section 2C

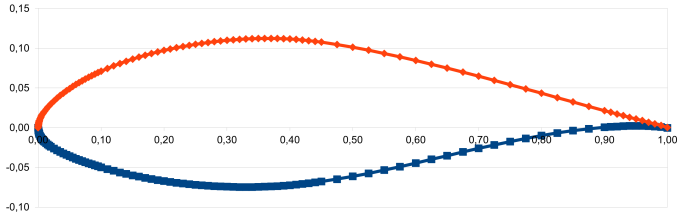

(c) Section 3C

Figure A.3: Additional blade sections between the RISØ and NACA airfoils.

Appendix B

Numerical options

The numerical options used for each numerical test presented in Section 5.1 are shown in this annex.

B.1 Wake length

	x_W	N_R	N_C	N_{hu}	N_{hd}	J_I	J_F	J_V	X_V	N_{WA}
	4R	30	60	30	45	6	30	[2,4,7,10,13, 16,19,22,25]	[0.05,0.1, 0.5,1.0,2.0]	3
	6R	30	60	30	45	6	30	[1,4,7,10,13, 16,19,22,25]	[0.05,0.1, 0.5,1.0,2.0]	3
	8R	30	60	30	45	6	30	[1,4,7,10,13, 16,19,22,25]	[0.05,0.1, 0.5,1.0,2.0]	3
$TSR = 6.7$	10R	30	60	30	45	6	30	[2,4,7,10,13, 16,19,22,25]	[0.05,0.1, 0.5,1.0,2.0]	3
	12R	30	60	30	45	6	30	[1,4,7,10,13, 16,19,22,25]	[0.05,0.1, 0.5,1.0,2.0]	3
	14R	30	60	30	45	6	30	[1,4,7,10,13, 16,19,22,25]	[0.05,0.1, 0.5,1.0,2.0]	3
	6R	30	60	30	45	6	30	[1,4,7,10,13, 16,19,22,25]	[0.05,0.1, 0.5,1.0,2.0]	3
	8R	30	60	30	45	6	30	[1,4,7,10,13, 16,19,21,23,25]	[0.05,0.1, 0.5,1.0,2.0]	3
$TSR = 10$	10R	30	60	30	45	6	30	[1,4,7,9,11,14, 17,18,20,22,24,25]	[0.05,0.1, 0.5,1.0,2.0]	3
	12R	30	60	30	45	6	30	[2,4,7,9,11,14, 17,19,21,22,24,25]	[0.05,0.1, 0.5,1.0,2.0]	3
	14R	30	60	30	45	6	30	[2,4,7,9,11,14, 17,19,20,22,24,25]	[0.05,0.1, 0.5,1.0,2.0]	3

Table B.1: Numerical options for the wake test at $TSR = 6.7$ and $TSR = 10$.

B.2 Blade radial distribution

	x_W	N_R	N_C	N_{hu}	N_{hd}	J_I	J_F	J_V	X_V	N_{WA}
	12R	30	60	30	45	6	30	[1,4,7,10,13, 16,19,21,23,25]	[0.05,0.1, 0.5,1.0,2.0]	3
	12R	40	60	30	45	8	40	[2,5,7,10,13,16 19,22,25,27,30,33]	[0.05,0.1, 0.5,1.0,2.0]	3
	12R	50	60	30	45	10	50	[2,3,5,7,11,14, 17,19,21,24,27,29] 31,33,35,37,41]	[0.05,0.1, 0.5,1.0,2.0]	3
$TSR = 6.7$	12R	60	60	30	45	11	60	[2,4,7,11,14,17 21,24,27,31,34,37, 41,43,46,50]	[0.05,0.1, 0.5,1.0,2.0]	3
	12R	70	60	30	45	13	70	[2,5,7,11,14,17, 19,21,24,27,29, 31,34,37,39,41,44 47,49,51,53,55,58]	[0.05,0.1, 0.5,1.0,2.0]	3
	12R	80	60	30	45	15	80	[2,4,7,11,14,17, 19,21,24,27,29,31 34,37,39,41,44,47, 49,51,54,57,61,63,65]	[0.05,0.1, 0.5,1.0,2.0]	3
	12R	30	60	30	45	6	30	[2,4,7,9,11,14 17,19,21,22,24,25]	[0.05,0.1, 0.5,1.0,2.0]	3
	12R	40	60	30	45	8	40	[2,3,5,7,11,14, 17,19,21,24,27,29, 32,33]	[0.02,0.05,0.1, 0.5,1.0,2.0]	3
	12R	50	60	30	45	10	50	[2,3,5,7,11,14, 17,19,21,24,27,29 31,33,35,39,40,41]	[0.05,0.1, 0.5,1.0,2.0]	3
$TSR = 10$	12R	60	60	30	45	11	60	[1,4,7,9,11,14 17,19,21,24,27,29] 31,33,35,37,39,41, 44,48,49,50]	[0.05,0.1, 0.5,1.0,2.0]	3
	12R	70	60	30	45	13	70	[2,3,5,7,9,11,14, 17,19,21,24,27,29 31,34,37,39,41,44, 47,49,51,53,57,59, 60,62]	[0.02,0.05,0.1, 0.5,1.0,2.0]	3
	12R	80	60	30	45	10	80	[2,3,5,7,9,11,14, 17,19,21,24,27,29 31,34,37,39,41,44, 47,49,52,55,57,59, 61,63,64,67,68,71]	[0.02,0.05,0.1, 0.5,1.0,2.0]	2

Table B.2: Numerical options for blade radial test at $TSR = 6.7$ and $TSR = 10$.

B.3 Blade chordwise distribution

	x_W	N_R	N_C	N_{hu}	N_{hd}	J_I	J_F	J_V	X_V	N_{WA}
	12R	80	60	30	45	15	80	[2,4,7,11,14,17, 19,21,24,27,29,31 34,37,39,41,44,47, 49,51,54,57,61,63,65]	[0.05,0.1, 0.5,1.0,2.0]	3
	12R	80	70	30	45	10	80	[2,4,7,11,14,17, 19,21,24,27,29,31 34,37,39,41,44,47, 49,51,54,57,59,61, 63,66,68,71]	[0.05,0.1, 0.5,1.0,2.0]	3
$TSR = 6.7$	12R	80	80	30	45	12	80	[2,3,5,7,11,14,17, 19,21,24,27,29,31 34,37,39,41,44,47, 49,51,54,57,59,62, 64,66,68,69]	[0.05,0.1, 0.5,1.0,2.0]	3
	12R	80	90	30	45	12	80	[2,3,5,7,11,14,17, 19,21,24,27,29,31 34,37,39,41,44,47, 49,51,54,57,59,61, 63,65,66,69]	[0.05,0.1, 0.5,1.0,2.0]	3
	12R	80	100	30	45	12	80	[2,4,7,11,14,17, 19,21,24,27,29,31 34,37,39,41,44,47, 49,51,54,57,59,61, 63,67,69]	[0.05,0.1, 0.5,1.0,2.0]	3
	12R	80	60	30	45	10	80	[2,3,5,7,9,11,14, 17,19,21,24,27,29 31,34,37,39,41,44, 47,49,52,55,57,59, 61,63,64,67,68,71]	[0.02,0.05,0.1, 0.5,1.0,2.0]	2
	12R	80	70	30	45	10	80	[2,3,5,7,9,11,14, 17,19,21,24,27,29 31,34,37,39,41,44, 47,49,52,55,57,59, 61,63,65,67,71]	[0.02,0.05,0.1, 0.5,1.0,2.0]	2
$TSR = 10$	12R	80	80	30	45	9	80	[2,3,5,7,9,11,14,	[0.02,0.05,0.1,	2

							17,19,21,24,27,29	0.5,1.0,2.0]	
							31,34,37,39,41,44,		
							47,49,52,55,57,59,		
							61,63,64,68,70,72]		
	12R	80	90	30	45	9	80	[2,3,5,7,9,11,14,	[0.02,0.05,0.1,	2
								17,19,21,24,27,29	0.5,1.0,2.0]	
								31,34,37,39,41,44,		
								47,49,52,55,57,59,		
								61,63,64,67,69,71,72]		
	12R	80	100	30	45	9	80	[2,3,5,7,9,11,14,	[0.02,0.05,0.1,	2
								17,19,21,24,27,29	0.5,1.0,2.0]	
								31,34,37,39,41,44,		
								47,49,52,55,57,59,		
								61,64,67,71,72]		

Table B.3: Numerical options for blade chordwise test at $TSR = 6.7$ and $TSR = 10$.

B.4 Hub upstream distribution

	$\boldsymbol{x_W}$	$\boldsymbol{N_R}$	$\boldsymbol{N_C}$	$\boldsymbol{N_{hu}}$	$\boldsymbol{N_{hd}}$	J_I	J_F	J_V	X_V	N_{WA}
	12R	80	80	30	45	12	80	[2,3,5,7,11,14,17,	[0.05,0.1,	3
								19,21,24,27,29,31	0.5,1.0,2.0]	
								34,37,39,41,44,47,		
								49,51,54,57,59,62,		
								64,66,68,69]		
$TSR = 6.7$	12R	80	80	35	45	12	80	[2,3,5,7,11,14,17,	[0.05,0.1,	3
								19,21,24,27,29,31	0.5,1.0,2.0]	
								34,37,39,41,44,47,		
								49,51,54,57,59,62,		
								64,66,68,69]		
	12R	80	80	40	45	12	80	[2,3,5,7,11,14,17,	[0.05,0.1,	3
								19,21,24,27,29,31	0.5,1.0,2.0]	
								34,37,39,41,44,47,		
								49,51,54,57,59,61,		
								63,65,68,69]		
	12R	80	90	30	45	9	80	[2,3,5,7,9,11,14,	[0.02,0.05,0.1,	2
								17,19,21,24,27,29	0.5,1.0,2.0]	

								31,34,37,39,41,44, 47,49,52,55,57,59, 61,63,64,67,69,71,72]		
$TSR = 10$	12R	80	90	35	45	9	80	[2,3,5,7,9,11,14, 17,19,21,24,27,29 31,34,37,39,41,44, 47,49,52,55,57,59, 61,63,64,67,69,71,72]	[0.02,0.05,0.1, 0.5,1.0,2.0]	2
	12R	80	90	40	45	9	80	[2,3,5,7,9,11,14, 17,19,21,24,27,29 31,34,37,39,41,44, 47,49,52,55,57,59, 61,63,64,67,69,71,72]	[0.02,0.05,0.1, 0.5,1.0,2.0]	2

Table B.4: Numerical options for hub upstream test at $TSR = 6.7$ and $TSR = 10$.

B.5 Hub downstream distribution

	$\boldsymbol{x_W}$	$\boldsymbol{N_R}$	$\boldsymbol{N_C}$	$\boldsymbol{N_{hu}}$	$\boldsymbol{N_{hd}}$	J_I	J_F	J_V	X_V	N_{WA}
	12R	80	80	30	45	12	80	[2,3,5,7,11,14,17, 19,21,24,27,29,31 34,37,39,41,44,47, 49,51,54,57,59,62, 64,66,68,69]	[0.05,0.1, 0.5,1.0,2.0]	3
$TSR = 6.7$	12R	80	80	30	55	12	80	[2,3,5,7,11,14,17, 19,21,24,27,29,31 34,37,39,41,44,47, 49,51,54,57,59,62, 64,66,68,69]	[0.05,0.1, 0.5,1.0,2.0]	3
	12R	80	80	30	65	12	80	[2,3,5,7,11,14,17, 19,21,24,27,29,31 34,37,39,41,44,47, 49,51,54,57,59,62, 64,66,67,69]	[0.05,0.1, 0.5,1.0,2.0]	3
	12R	80	90	30	45	9	80	[2,3,5,7,9,11,14, 17,19,21,24,27,29 31,34,37,39,41,44, 47,49,52,55,57,59,	[0.02,0.05,0.1, 0.5,1.0,2.0]	2

								61,63,64,67,69,71,72]		
$TSR = 10$	12R	80	90	30	55	9	80	[2,3,5,7,9,11,14, 17,19,21,24,27,29 31,34,37,39,41,44, 47,49,52,55,57,59, 61,63,64,67,69,71,72]	[0.02,0.05,0.1, 0.5,1.0,2.0]	2
	12R	80	90	30	65	9	80	[2,3,5,7,9,11,14, 17,19,21,24,27,29 31,34,37,39,41,44, 47,49,52,55,57,59, 61,63,64,67,69,71,72]	[0.02,0.05,0.1, 0.5,1.0,2.0]	2

Table B.5: Numerical options for hub downstream test at $TSR = 6.7$ and $TSR = 10$.